Strategies for Overcoming Shortcomings of Thermal Ablations: A Comprehensive Study of Nanoparticle Transport During Photothermal Chemotherapy Treatments, and High Frequency Irreversible Electroporation

Matthew R. DeWitt

Dissertation submitted to the faculty of the Virginia Polytechnic Institute and State University in partial fulfillment of the requirements for the degree of

Doctor of Philosophy
In
Biomedical Engineering

Marissa N. Rylander
Rafael V. Davalos
John L. Robertson
Christopher G. Rylander
Christopher R Byron

August 12th, 2016
Blacksburg, VA

Keywords: nanoparticles, tumor engineering, photothermal enhancement, irreversible electroporation

Strategies for Overcoming Shortcomings of Thermal Ablations: A Comprehensive Study of Nanoparticle Transport During Photothermal Chemotherapy Treatments, and High Frequency Irreversible Electroporation

Matthew R. DeWitt

ABSTRACT

Cancer continues to be a leading cause of death worldwide despite the increasing research advances into novel targeted treatments. Physical tumor destruction remains a viable therapeutic modality despite new molecular and biological targets. Specifically, thermal ablation of tumors is a relatively established therapy of numerous tumor types, despite inherent shortcomings which include incomplete tumor and margin treatment, contraindications from sensitive nearby structures, and the non-specific nature of thermal energy. Within the field of thermal cancer therapies, there is a new focus on utilizing nanoparticles to deliver non-lethal hyperthermia that enhance carried chemotherapeutic drugs. Additionally, a novel field of non-thermal ablations termed Irreversible Electroporation has recently been developed to treat tumors by irreversibly destroying cell membrane function through externally applied short electrical pulses.

The goal of the present study is to research two novel potential treatments for cancer that destroy tumors with energy which do not require complete thermal destruction. We first developed and tested novel methods to load the antineoplastic agent Cisplatin into carbon nanoparticles (SWNHs) to thermally enhance loaded drugs with non-lethal, mild hyperthermia. In the second aim we utilized a perfusable 3D collagen *in vitro* model of the tumor microenvironment, previously developed by our group to study tumor angiogenesis, to study nanoparticle transport. We demonstrated the ability of this model to study key mass transport obstacles nanoparticles face in the tumor including

extravasation from a leaky, pro-angiogenic vasculature, diffusion in the extracellular matrix, and cellular uptake in a 3D environment which are often overlooked in 2D cell studies. This model was then utilized in the third aim to study how mild hyperthermia affects transport of SWNHs, highlighting the role of tumor vasculature disregulation on ability to drive SWNHs into the tumor microenvironment. Lastly, we tested the non-thermal ablation, high-frequency irreversible electroporation (H-FIRE) in a 3D tumor platform and in an *in vivo* swine model to test H-FIRE as a repeatable therapy for hepatocellular carcinoma, a disease state growing in incidence rate. We then used H-FIRE in an outpatient treatment for infiltrative skin tumors in equines, showcasing the ability to deliver high voltage, short duration pulses in a clinical setting without muscle contractions which could overcome many complications associated with the intense anesthetic protocol for IRE clinical treatments.

Strategies for Overcoming Shortcomings of Thermal Ablations: A Comprehensive Study of Nanoparticle Transport During Photothermal Chemotherapy Treatments, and High Frequency Irreversible Electroporation

Matthew R. DeWitt

GENERAL AUDIENCE ABSTRACT

Cancer continues to be a leading cause of death worldwide despite the increasing research advances into novel targeted treatments. Physical tumor destruction remains a viable therapeutic modality despite new molecular and biological targets. Specifically, thermal ablation of tumors is a relatively established therapy of numerous tumor types, despite inherent shortcomings which include incomplete tumor and margin treatment, contraindications from sensitive nearby structures, and the non-specific nature of thermal energy. Within the field of thermal cancer therapies, there is a new focus on utilizing nanoparticles to deliver non-lethal hyperthermia that enhance carried chemotherapeutic drugs. Additionally, a novel field of non-thermal ablations termed Irreversible Electroporation has recently been developed to treat tumors by irreversibly destroying cell membrane function through externally applied short electrical pulses.

The goal of the present study is to research two novel potential treatments for cancer that destroy tumors with energy which do not require complete thermal destruction. We first developed and tested novel methods to load the antineoplastic agent Cisplatin into carbon nanoparticles (SWNHs) to thermally enhance loaded drugs with non-lethal, mild hyperthermia. We attached the imaging agent Quantum Dots (QDs) to the carbon particles in order to understand how hyperthermia affects cellular uptake, minimizing thermal enhancement. Results of this study highlight the need for better

biomimetic *in vitro* models of the tumors to study how hyperthermia affects tissue level transport of nanoparticles.

In the second aim we utilized a perfusable 3D collagen *in vitro* model of the tumor microenvironment, previously developed by our group to study tumor angiogenesis, to study nanoparticle transport. We demonstrated the ability of this model to study key mass transport obstacles nanoparticles face in the tumor including extravasation from a leaky, pro-angiogenic tumor vasculature, diffusion in the dense extracellular matrix, and cellular uptake in a 3D environment. This model was then utilized in the third aim to study how mild hyperthermia affects transport of SWNHs. Results from this aim were valuable in showing the utility of the 3D *in vitro* model to controllably test the effects of external stimuli on transport of particles and demonstrates the mechanism for how mild hyperthermia can selectively allow increased permeability of SWNHs in the tumor microenvironment by increasing selectivity of nanoparticle transport to the targeted tissue. Ultimately this work highlights the need for early nanoparticle optimization in more biomimetic testing platforms in order to better develop based on the physiological boundaries to therapy delivery.

Lastly, we tested the non-thermal ablation, high-frequency irreversible electroporation (H-FIRE) in a 3D tumor platform and in an *in vivo* swine model to better understand the ability of H-FIRE to produce repeatable destruction of hepatocellular carcinoma, a disease state growing in incidence rate. We then used H-FIRE in an outpatient treatment for infiltrative skin tumors in equines, showcasing the ability to deliver high voltage, short duration pulses in a clinical setting without muscle

contractions which could potentially expand the application of non-thermal ablation into indications currently limited by the difficult anesthetic protocol.

Ultimately, the results of this study demonstrate the tie between engineering solutions to model the tumor microenvironment with the basic science of therapy discovery and optimization that must occur to optimize novel treatments utilizing non-lethal hyperthermia, or non-thermal death mechanism to treat cancer. The studies show the usefulness of more complex 3D *in vitro* models of tumors for early development of novel therapies and the utility of *in vivo* models to validate studies.

Acknowledgments

This research presented in my dissertation was only made possible through the generous help of many researchers, faculty, staff, postdocs, and other graduate students. I will always remember the help, guidance, and general collaborative spirit that make Virginia Tech such a special place.

I first must thank my advisor Dr. Nichole Rylander, thank you for believing me from the start. It's been a long 5 years working on a variety of different projects with you, and I have grown so much as a researcher because of you. I deeply appreciate your guidance, freedom to purse many ideas, and your multiple, sometimes difficult, rounds of revisions on my manuscripts. Thank you for being so flexible and helpful these past two years, allowing me to stay in Blacksburg while continuing to help and work with your students in Austin.

I would like to send a special thank you to my "step-advisor" Dr Rafael Davalos. Words cannot describe how thankful I am for you allowing me to come into your lab. I feel that I am much more of well-rounded engineer having had the chance to work with your group. Dr John Robertson, you have been an amazing collaborator and mentor, you helped me on so many projects involved in this dissertation and so many more that didn't even make it in this. Dr Chris Rylander, thank you for expanding my critical thinking abilities and your thoughtful insights into my project throughout the years. Dr Chris Byron, thank you for stepping in when I needed you most. It has been great working on the equine and porcine studies with you.

The most important thanks goes out to fellow students that made not only this work possible, but enjoyable. I appreciate the mentorship from Dr Bryce Whited, Dr Chris Arena, Dr Chris Szot, Dr Katelyn Bittleman. Dr Mike Sano, while our phone applications may never make it in the real world, I profoundly appreciate not only your constant help but also your friendship throughout this whole process. Eduardo Latouche thanks so much for being such a great friend and awesome labmate to work with. Allison Pekanan, you have been an amazing asset to this project and taught me so much about chemistry, much of the nanoparticle work would be impossible without you. Thank you Bill, Lyle, Paulo, Rudy, Patrick, Dan Marrinan, Rhys, Manasa, and Chris Idelson for being such amazing friends throughout the years.

Most of all I want to thank my family and girlfriend Katlin Mooneyham. My mom and dad have been the most supportive parents I could ever ask for. It is because of y'all that I had the confidence and ability to work through such a difficult 5 years. Katlin, without you, I cannot imagine getting through these past 3 years. I am so lucky to have you in my life, thank you for putting up with me. And thanks Jackson for showing me the value of being lazy sometimes.

Contents

Figure List

Chapter 4

Chapter 5

Fig. 2 H-FIRE treatment in a 3D in vitro tumor platform. Live[Green] and dead[red] regions of cells in 3D hydrogel containing H4IIE separated by white dashed line after treatment of 100 burst of 100us on time for 1us(A) and 2us(B) pulses. The electric field threshold was determined utilizing a COMSOL model of the

Chapter 1: Introduction and Motivation

Cancer remains a leading cause of death worldwide and despite significant medical advances to reduce the mortality rate of other major diseases (such as heart disease), the number of cancer related deaths continues to increase every year. While traditional cancer therapies, such as chemotherapy and radiation treatment, have had limited success in the fight against cancer, there is much room for improvement. In addition to molecularly fighting cancer there is great interest in developing novel, energy based ablation technologies to destroy tumors and metastasis[1].

Thermal based ablation of tumors is the local application of potentially extremely high temperature (>60°C) for short duration or milder hyperthermia (>45°C) for longer durations, which is used to induce irreversible cell injury and ultimately tumor apoptosis or coagulative necrosis. The clinical delivery of hyperthermia is an ancient technique that was thought to be first utilized and documented by Hippocrates to treat surface tumors with a hot iron. More recently, in the first half of the 20th century, techniques for hyperthermia were employed including hot water bath, perfusion heating, and high frequency energy based ablation [2]. One of the primary benefits of tumor hyperthermia treatments is the higher sensitivity of cancer cells to temperatures compared to normal cells, possibly decreasing side effects when treatment planning is utilized.

Currently the most commonly utilized techniques in the clinic to perform thermal therapy or thermal ablation of tumors are radiofrequency ablation (RFA) and microwave ablation (MWA). RFA utilizes an active electrode to deliver a radiofrequency current, around 460 KHz, to a much larger passive electrode or grounding pad located distant from tumor site. The resulting high current density at the active electrode coupled with

the rapid current switching of the energy delivered results in ionic movement in the area near the electrode in the tumor causing frictional heating. MWA is a dielectric heating based ablation in which the dielectric material is the desired tumor tissue. During MWA the alternating electromagnetic field forces water molecules in the tissue to oscillate out of phase with the applied field leading to energy absorption and conversion to heat. A review of the effects of hyperthermic ablation is seen in Figure 1-1 below, taken from Chu et al[3].
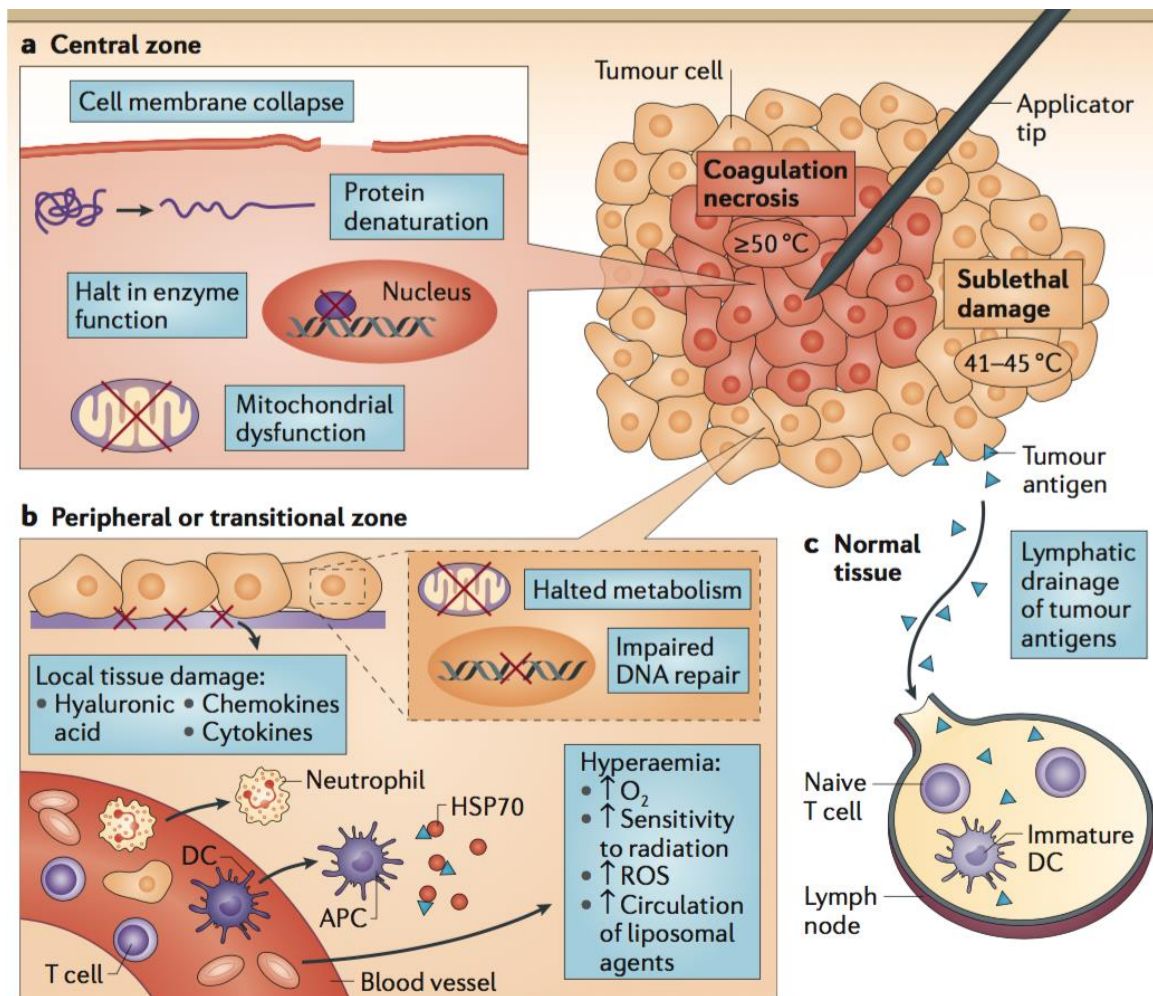
Figure 1. Overview of Effects of Hyperthermia on Tumor Destruction. Taken from Chu et al[3].

In addition to current clinical use of hyperthermia for tumor treatment, there is

great interest in the potential of using nanoparticles to act as antenna for external irradiation coined Photothermal Therapy. As the name suggests, photothermal therapy is based around the conversion of light energy into heat, either through plasmon resonance energy transfer or a vibrational energy transfer from atoms in nanoparticles to atoms in surrounding media or tissue. Although irradiating tissue with laser light without the presence of nanoparticles will cause tissue heating, the capability to transfer heat efficiently in a localized area is unique to nanoparticle photothermal therapy. The specificity of nanoparticle heating is limited to the area directly surrounding the particle, thereby limiting damage to the surrounding healthy tissue. Nanoparticles for use with photothermal therapy vary widely; the most commonly used particles revolve around the use of gold to transfer plasmon resonance from the particle to the surrounding tissue. These include gold nanorods, gold nanospheres, and silica core/gold shell particles, among others. A wide variety of other metals are also used, including silver particles, iron oxide-containing particles, and copper-containing particles. Carbon particles in photothermal therapy, including carbon nanotubes, graphene oxide, and carbon nanohorns, capitalize on the transfer of vibrational energy from the graphene atoms to the surrounding tissue. Polymer systems have also been explored recently as a potential biodegradable particle for photothermal therapy, bypassing many common concerns of higher costs and tissue retention associated with metal particles.

While these thermal therapies can provide several advantages over surgical resection including lower morbidity, increased preservation of neighboring tissue, and reduced therapy cost they also have inherent shortcomings independent of heating mode. These disadvantages include incomplete ablation and tumor recurrence. Thermal based

ablations induces indiscriminate, necrotic tissue destruction which can damage healthy vital structures near the tumor and the presence of major portal veins and hepatic veins can cause incomplete tumor necrosis due to heat sink effects leading to incomplete destruction. Therefore, tumor therapies that do not require sufficient heating for monotherapy or utilize other modes of cancer cell ablation can possibly overcome these shortcomings.

In the first scientific chapter of this document (Chapter 2) we determined the efficacy and ability of Single Walled Carbon Nanohorns(SWNHs), which have previously been shown to be excellent photo-absorbers and drug delivery vehicles, to produce synergistic effects with mild hyperthermia and carried Cisplatin. Photothermal-chemotherapy treatments utilize the heat generation capabilities of nanoparticles to deliver mild hyperthermia which has shown to be significantly less complicated than complete photothermal destruction of tumors. The results from this study highlight the difference between thermal enhancement of free drug and drug delivery vehicles by determining the uptake of these particles in 2D cell culture. This data is valuable for both showing the need for optimization of these photothermal-chemotherapy in early design stages while highlighting the shortcomings of static 2D cell cultures, which are commonly utilized for these types of studies.

In order to better understand how hyperthermia affects nanoparticle based photothermal-chemotherapy treatments it is imperative to establish how hyperthermia acts as an adjuvant. While heat has classically been viewed as an adjuvant therapy to increase the efficacy of chemotherapeutic drugs, with the development of co-delivery nanoparticles, heat should be considered to also affect particle transport. Therefore, in the

third chapter of this document we developed and utilized a microfluidic model to determine key transport barriers nanoparticles face in tumor transport. We validated our model to determine transport kinetics of different sized particles and the ability of the system to be used in cell-recovery analysis. While traditional cell culture models of tumors can be valuable for studying the last stage of nanoparticle transport in the tumor microenvironment, cellular uptake, this model shows the ability to create a cost efficient, reproducible *in vitro* model to study more of the dynamics of nanoparticle transport in the tumor microenvironment.

In the fourth chapter of this document we utilized the microfluidic platform developed in the fourth chapter to determine how hyperthermia affects these different transport barriers that nanoparticles face in the tumor microenvironment. Results shed light on the change of transvascular transport of SWNHs during hyperthermia and accumulation in the ECM. Results from this study highlight how useful a microfluidic model of the tumor microenvironment can be to elucidate perturbation therapies such as mild hyperthermia, which is often impossible in highly complex in vivo tumor models. Ultimately, studies involving more complex, controllable in vitro models of the tumor microenvironment will lead to optimization of these therapies.

In the fifth chapter of this chapter a novel ablation technique previously developed in the lab, High Frequency Irreversible electroporation (H-FIRE), was studied in an in vitro model of hepatocellular carcinoma and an *in vivo* swine model to determine its ability to treat liver tumors and the unique biophysical approaches that must be understood for optimizing H-FIRE treatments. H-FIRE can overcome many of the complications of currently utilized thermal ablations, as it does not actually use thermal

energy for tumor cell destruction. Instead, high frequency bipolar pulses of 500 ns - 2us generate an electric field that causes irreversible cell membrane damage that leads to cell death. The results from this aim show how H-FIRE can be utilized to create clinically valuable lesion sizes and parameter tuning can occur to shift the mode of cell death from necrotic to apoptotic. Ultimately this data will be combined with novel computational models of the in vivo treatment to compare in vitro and in vivo results, hopefully helping to bridge the gap between these two models when optimizing H-FIRE treatments.

In the sixth chapter we highlight the need for non-thermal ablation technologies in the veterinarian surface lesion therapeutic field. Many surface lesions including sarcoids and melanomas are often in critical locations including perianal and perivulvar, limiting the ability to apply thermal therapies near these critical structures. Additionally, with the treatment of equine patients, the ability to use mild anesthesia and local blocking is necessary to reduce complications of full anesthesia with equine patients. In this chapter we highlight how the unique pulses regime utilized in H-FIRE treatments reduce muscle contractions seen in typical IRE treatments, allowing for the use of mild sedation during clinical delivery of pulses in the treatment of multiple surface lesions.

While thermal therapies will continue to be utilized in the clinic to treat many soft tissue cancers, there are many avenues to optimize therapies that do not require sufficient heat to destroy tumors. In this dissertation two of these therapies were studied. The first of which is photothermal –chemotherapy treatments where a mild hyperthermia is used to enhance drug efficacy and in the second a novel non-thermal electroporation technique was studied. Results reveal the promise of these novel therapies and describe the

engineering challenges for pre-clinical optimization that must occur prior to successful

implementation.

1. Ahmed M, Brace CL, Lee FT, Jr., Goldberg SN (2011) Principles of and advances in percutaneous ablation. Radiology 258: 351-369.
2. Hager ED, Dziambor H, Hohmann D, Muhe N, Strama H (2001) Intraperitoneal hyperthermic perfusion chemotherapy of patients with chemotherapy-resistant peritoneal disseminated ovarian cancer. Int J Gynecol Cancer 11 Suppl 1: 57-63.
3. Chu KF, Dupuy DE (2014) Thermal ablation of tumours: biological mechanisms and advances in therapy. Nat Rev Cancer 14: 199-208.

Chapter 2: Influence of Hyperthermia on Efficacy and Uptake of Carbon Nanohorn-Cisplatin Conjugates

This chapter was published in The Journal of Biomechanical Engineering

2.i. Abstract:

Single walled carbon nanohorns (SWNHs) have significant potential for use in photothermal therapies due to their capability to absorb light and deposit heat. Their extensive relative surface area and volume also make them ideal drug delivery vehicles. By capitalizing on these unique qualities, new multimodal treatments are envisioned to create a localized hyperthermic environment under excitation of an NIR laser source to enhance the chemotherapeutic efficacy of loaded drugs. Drugs such as cisplatin (CDDP) are known to be enhanced in response to mild hyperthermia (41-43°C) making them an excellent candidate for these multimodal therapies. Although hyperthermia has been shown to increase cellular uptake of cisplatin leading to thermal enhancement, studies to determine the effects of hyperthermia on cisplatin loaded nanoparticles are limited. In this study, we determine the effects of mild hyperthermia on the efficacy of surface and volume loaded CDDP-SWNH conjugates. After forming the nano-drug conjugates, an in vitro study with rat bladder transitional carcinoma cells demonstrated that unlike free CDDP, CDDP-SWNH conjugates do not exhibit thermal enhancement at 42°C. Flow cytometry and confocal microscopy showed a decreased uptake of CDDP-SWNH conjugates at 42°C revealing the importance of nanoparticle uptake on the CDDP-SWNH conjugate's efficacy particularly when hyperthermia is used as an adjuvant. These experiments indicate the need for careful consideration of drug loading properties while developing novel nano-drug conjugates for use in multimodal photothermal-chemotherapy treatments to ensure favorable thermal enhancement of chemotherapeutic agent.

2.1 Introduction:

Cancer is a leading cause of mortality worldwide and while new technologies are continually being explored, the rates of incidence and survival remain unchanged. Urinary bladder cancer in particular is gaining attention from researchers as it is the fourth most common non-cutaneous malignancy. Currently, transurethral resection of bladder tumors is the primary treatment course. However, patients that undergo conventional resection often experience high rates of recurrence and can suffer from poor quality of life following complete resection [1]. Therefore, the development of new therapeutic strategies to improve patient morbidity and prognosis of superficial and invasive urinary carcinomas is of the upmost importance.

To overcome the shortcomings of conventional surgical treatments, therapies that utilize mild hyperthermia (41-43°C) and a wide range of chemotherapeutic agents including antineoplastic agents such as cisplatin (CDDP) have been explored [2-5]. A wide variety of studies both in vitro and in vivo have investigated the enhancement of CDDP with hyperthermia and have shown promising results including not only additive killing but synergism between the heat and drug [5] Specifically, CDDP is investigated for use in bladder cancers as an adjuvant to thermal therapies due to these enhancement properties[6]. Compared to chemotherapy alone, application of heat in addition to chemotherapy has shown a significant decrease in progression and recurrence in bladder and other malignancies and can overcome complications which leads to significant collateral damage to healthy tissue and major patient discomfort [7-9].

While the mechanism for thermal enhancement of antitumor drugs remains controversial, it is known that an effective treatment using CDDP results when the drug is transported into tumor cells and accumulates in the nucleus where it can react with DNA resulting in DNA adducts [10]. The formation of these adducts eventually results in apoptosis due to inability to replicate DNA [3, 5, 11]. There are

many possible explanations for the increase in drug efficacy when utilized in combination with hyperthermia, but the two prevailing hypothesized mechanisms are enhanced diffusion into the cell caused by a more fluid membrane under hyperthermic conditions and increased intercalations with the DNA as a result of unknown cellular changes [12]. While the theoretical application of heat and CDDP results in higher efficacy of treatment, with viability of tumor cells decreasing by as much as 30% in the combinatorial treatment compared to CDDP alone[5], the practicality of simultaneous application of the two modalities is limited due to complications in the application of the multi-modal treatment resulting in an increase in toxicity in healthy tissue, thus limiting the overall utility of the combination [13, 14].

With this shortcoming in mind, nanotechnology could provide the missing link between theoretical studies and a clinically viable treatment option with both heat and drug delivery that results in less residual toxicity and damage to healthy tissue [15]. Nanoparticle assisted photothermal therapies have provided a foundation for new treatment regimens which include highly localized and selective heating and targeted delivery of drugs [16]. These therapies utilize unique nanostructures, including gold nanorods and spheres[17, 18], gold nanoshells[19], and carbon nanomaterials such as single and multi-walled nanotubes[20] and single walled carbon nanohorns that absorb light strongly in the near-infrared (NIR region) and convert the light into heat to locally destroy the tumor[21, 22]. Despite the promise of nanoparticle assisted therapies, they can produce uneven heating of the tissue due to a heterogeneous distribution of nanoparticles in a non-uniform tumor which can lead to incomplete destruction, resulting in reoccurrences [23, 24]. These shortcomings in nanoparticle assisted photothermal therapies alone provide a need for multimodal therapies to destroy tumors with higher efficacy and lower reoccurrence. Specifically, the introduction of a chemotherapeutic drug is necessary as an adjuvant to these thermal therapies to overcome issues of non-specific heating, development of thermal resistance, and limitations associated with thermal therapies reaching deep tissue tumors[8].

While gold nanorods and spheres, gold nanocages, and carbon nanomaterials are conventionally used to deliver only heat for tumor ablation, they can also be utilized to deposit heat selectively to induce a mild hyperthermia in the desired treatment region to enhance the therapeutic efficacy of a chemotherapeutic drug through thermal enhancement as mentioned previously [18]. The use of light absorbing nanoparticles therefore can be used to create a synergistic effect with a chemotherapeutic drug, overcoming many of the shortcomings of photothermal therapies alone such as incomplete destruction of the tumor resulting from insufficient thermal deposition. Specifically, the use of CDDP with gold nanorods or graphene oxide in combination with NIR light to produce a synergistic effect of heating with a chemotherapeutic agent has recently been explored. The studies found that these nanoparticles are capable of producing a thermal stimulus needed for enhancement of the drug with decreases of viability occurring in the combinatorial studies being as much as 25% in vitro [23, 25, 26]. The introduction of a chemotherapeutic drug is necessary as an adjuvant to these thermal therapies to overcome issues of non-specific heating, development of thermal resistance, and limitations associated with thermal therapies reaching deep tissue tumors[8].

The nanoscale (~100 nm) size these photoabsorbing nanoparticle allows for passive targeting to the tumor site by exploitation of the enhanced permeability effect which results from a leaky vasculature in the tumor microenvironment [27]. While free drugs can passively diffuse out of the blood vessels, the leaky vasculature of the tumor may permit a nanoparticle carrying a drug to extravasate only in the tumor space [28]. Additionally, the dysfunctional lymphatic drainage in tumors aids in retention of the extravasated nanoparticles and therefore allows their accumulation in the desired region enabling drug localization and treatment[29]. In addition, it has been shown that a mild hyperthermia, which could be delivered by the nanoparticles in combination with laser irradiation, aids in the extravasation of larger

nanoparticles to the tumor site in a size dependent manner, resulting in enhanced accumulation of nanoparticles reaching their targeted destination [30]. Overall, the ability to conceal a drug within a nano-sized device capable of producing heat leads to possibly the greatest passive targeting to the desired location. With the addition of active targeting through the addition of ligands to the surface of the nanoparticle, this treatment can be further enhanced [31].

Single walled carbon nanohorns (SWNHs) stand out as a promising nanoparticle choice for multimodal vehicles of heat delivery and chemotherapy [21]. SWNHs offer many advantages over other nanomaterials, including low inherent toxicity due to lack of a metal catalyst during synthesis thereby resulting in high purity of SWNHS (90-95%), increased surface area compared to spherical particles, and high drug loading volume [32]. While other carbon nanotubes aggregate in micron sized particles, SWNHs form a spherical or dahlia like shape (Figure 1) on the order of 100 nm which allows for passive tumor targeting. Additionally others have shown the ability to incorporate CDDP into SWNHs and have verified efficacy in vitro [33, 34]. Sequestering CDDP within the interior of the SWNHs allows for delivery of clinically relevant does of drug to passively target tumor cells with minimal delivery to non-tumor regions, taking advantage of the high internal drug space. We have demonstrated the ability of SWNHs to be used with clinically relevant laser parameters and nanoparticle concentrations to generate lethal temperature elevations and cause tumor cell death [22, 35-37]. Overall, the high capacity for both photoabsportive heat delivery and drug loading gives SWNHs many advantages for these multimodal therapies when compared to other nanoparticles used for their absorptive properties.
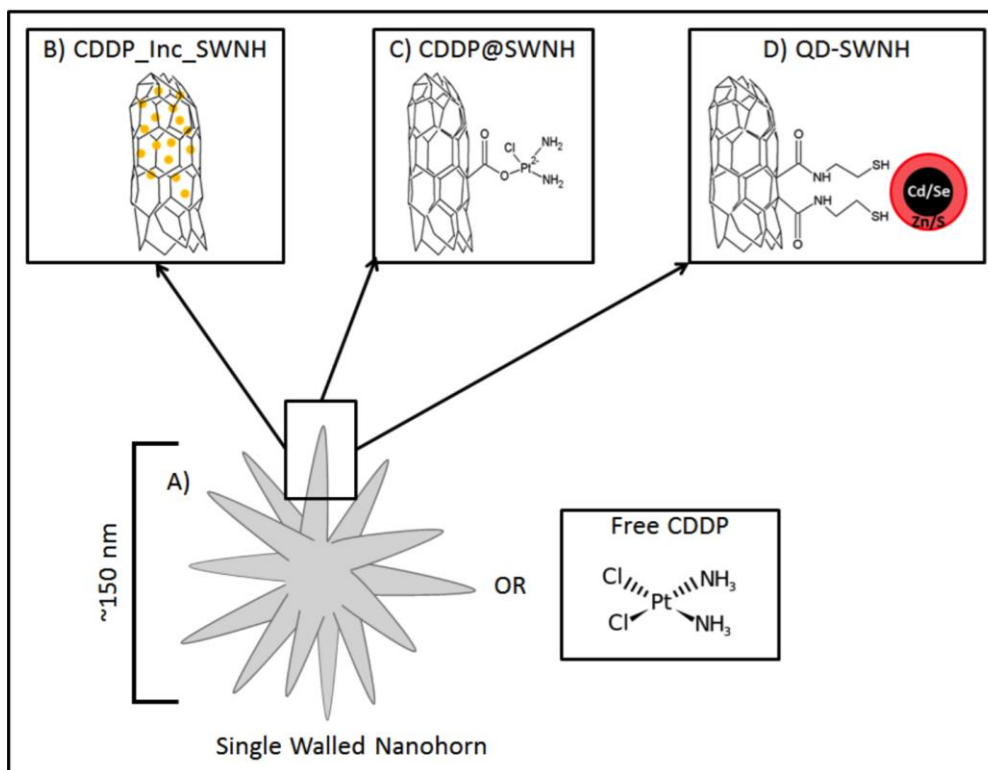
Figure 1: A) an overall cartoon depiction of Single Walled Nanohorns with their aggregated state of many single walled cones forming ~80 nm diameter dahlia shape. In these experiments we tested two types of CDDP-SWNHs conjugates to determine their potential use as photothermal enhancers of the drug. The first SWNH-CDDP is the incorporated CDDP (B) in which the SWNHs are opened and CDDP is loaded into the internal space of the nanoparticle. The second (C) utilizes simple chemistry to attach the CDDP to the outside of the SWNH such that the CDDP is covalently attached to the SWNHs. In order to visualize uptake kinetics, Zn/S shell Cd/Se quantum dots were attached to the SWNHs (D).

These unique characteristics of SWNHs allow for two different types of drug-nanoparticle conjugates which exploit one of the two high drug loading possibilities, surface and interior loading, both of which are depicted in Figure 1. The first of these nanoparticle conjugates is incorporated or trapped CDDP in which the CDDP is located freely inside of the SWNHs to capitalize on the high internal volume; this allows for leaching out over time at a slow rate [38]. Additionally, following methods for attachment of CDDP to chemically similar single walled nanotubes, we for the first time, harness the chemical structure and high surface area of SWNHs to chemically attach CDDP to the surface of the nanohorns [39].

Here we explore the potential uses of SWNHs as a drug delivery vehicle with a payload of CDDP along with its possible use in multimodal hyperthermia treatments. The overall efficacy of two

13

different types of CDDP-SWNH conjugates (attached and incorporated) was examined in an in vitro setting using a rat bladder transitional carcinoma cell line. Additionally, we determined uptake and release kinetics of the CDDP-SWNH conjugates under normal physiological and hyperthermic conditions. We have shown for the first time that the degree of thermal enhancement is strongly influenced by the mode of incorporation of the drug in the nanoparticle and is a function of cellular uptake of the nanoparticle.

2.2 METHODS

2.2.1 Cell Culture

The effects of hyperthermia on the efficacy of SWNHs as drug delivery vehicles were evaluated in N-(4-[5-nitro-2-furyl]-2-thiazolyl) formamide induced rat bladder transitional cell carcinoma cells, AY-27 cells, originally developed by Dr. S. Selman and Dr. J Hampton (medical College of Ohio, Toledo, OH). AY-27 cells were cultured in RPMI Medium 1640 (Invitrogen; Grand Island, NY) supplemented with 10% fetal bovine serum (FBS, Sigma Aldrich; St. Louis, MO), 1% penicillin and streptomycin(Sigma Aldrich), and were maintained in a humidified atmosphere at 37°C with 5% CO2 and 95% air. Cells were passaged every 4 days prior to reaching 80% confluency. Passage numbers 37-42 were used for all experiments.

2.2.2 Preparation of CDDP-SWNHs

SWNHs were obtained from Dr. David Geohegan from Oak Ridge National Laboratory. These pristine SWNHs were oxidized by the addition of 8M nitric acid and heating to 120°C under reflux. Oxidized SWNHs were reprotonated using a 1M hydrochloric acid solution to yield particles with a protonated carboxylic acid groups. For the purposes of this paper, oxidized SWNHs will be referred to as SWNHs subsequently.

Two types of CDDP-SWNH nano-conjugates were investigated in this study to determine the most suitable system for delivery of heat using NIR light and drugs to the cancer cells. The first nano-drug conjugate was a SWNH with cisplatin (cis-diamminedichloroplatinum(II),CDDP; Sigma Aldrich; St. Louis, MO) incorporated freely within its interior. Following Aijima et al's method, CDDP was incorporated into the interior of the SWNH by first dissolving cisplatin in DMSO to make a 1 mg/mL solution [34]. This solution was then sonicated for 1-2 minutes to dissociate aggregates and disperse the CDDP. After stirring for 2 hours, SWNHs were added to make a 1:1 w/w ratio of CDDP to SWNH, sonicated for 15-30 minutes until dispersed, and stirred for an additional 2 hours. Following stirring, the solution was put under nitrogen flow until completely dry (up to 2 days). Before use, the particles were resuspended in Phosphate Buffered Saline (PBS; ThermoScientific; Logan, UT) and sonicated gently to ensure a homogenous mixture. This CDDP-SWNH formulation will be referred to as CDDP_INC_SWNH and can be seen in Figure 1(B).

The second CDDP-SWNH conjugate used in this study involved CDDP covalently attached to the exterior surface of the SWNH. Modified from a study in which CDDP was attached to single walled carbon nanotubes, these particles were created via a carbodiimide reaction [39]. First, SWNHs were sonicated until dispersed in dH20 at a concentration of 0.1 mg/mL. The solution was transferred to a round bottom flask and N-(3-Dimethylamino propyl)-N'-ethylcarbodiimide hydrochloride (EDC; Sigma Aldrich; St. Louis, MO) was added while stirred. After 5 minutes of stirring, N-hydroxysulfosuccinimide sodium salt (sulfo- NHS; Sigma Aldrich; St. Louis, MO) was added to the solution and stirred for an additional 5 minutes. The final concentrations of EDC and sulfo-NHS are 0.1 M and 0.005 M, respectively. Cisplatin was dissolved in dimethyl sulfoxide (DMSO; Fisher Scientific; Fair Lawn, NJ) to make a 1 mg/mL solution, and this solution was added to the SWNH solution such that the ratio of cisplatin to SWNHs was 1:1 w/w. The solution was warmed gently by setting the hot

plate to 37-38°C and allowed to stir at 300 rpm for 1 h. This final solution was filtered through a 0.1 μm Nylon membrane over vacuum filtration. The solid product was washed 2-3 times with water, once with ethanol to sterilize, and an additional 2-3 times with water in order to remove the ethanol and any residual CDDP not attached to SWNHs. To resuspend the particles, the membrane was transferred to a small vial containing PBS. The membrane in PBS was sonicated for 1-2 minutes until the particles were suspended in solution. This CDDP-SWNH complex will be referred to as CDDP@SWNH and can be seen in Figure 1(C).

2.2.3 Preparation of SWNH-QDs

SWNHs like many nanoparticles utilized for photothermal therapies or delivery vehicles, lack an inherent fluorescent signal, making visualization of the particles even in an in vitro setting nearly impossible. To overcome this shortcoming and to facilitate monitoring of uptake of the SWNHs as a function of temperature, quantum dots (QD) (CdSe/ZnS core shell Quantum dots) were attached to the SWNHs using an EDC/NHS reaction. SWNHs were dispersed in dH20 at a final concentration of 0.1 mg/mL and were sonicated for 1 h to reduce aggregations. SWNHs were then added to a round bottom flask containing 0.1 M EDC and stirred for 5 minutes after which 5 mM of sulfo-NHS was added to the solution. Cysteamine hydrochloride (AET; Sigma Aldrich; St. Louis, MO) was then added to the flask at a concentration of 0.2 M and the overall solution was adjusted to a pH of 6.0 using 1.0 M HCL to prevent disulfide formation. After 24 h of stirring, commercially available QD powder (Ocean Nanotech LLc; Springdale, AR) was dissolved in chloroform (1.0 mg/mL) and added to the SWNHs in a weight ratio of 3:1 w/w QD to SWNH. The pH of the solution was then adjusted to 7.0 for enhanced particle stability and the mixture was then mixed for 24 h. The high affinity of thiol for the ZnS coating on the QDs causes them to move from the chloroform phase into the SWNHs, creating the SWNH-QD

complex. A summary of SWNH shape and the nanoparticle conjugates used in this paper can be seen in Figure 1.

2.2.4 Characterization of Nanoparticles

Transmission electron microscopy (TEM) was used to evaluate the presence and localization of CDDP or QDs on different SWNH complexes (Inc, @, and QD) using a Zeiss 10CA TEM equipped with AMT Advantage GR/HR-B CCD camera system (Carl Zeiss AG; OBerkochen, Germany). To prepare TEM grids, samples of SWNHs, SWNH-QD, CDDP@SWNH, and CDDP_INC_SWNH were diluted in methanol to approximately 0.05 mg/mL. This sample was introduced to a 200 nm Lacey carbon mesh TEM grid (Electron Microscopy Sciences; Hatfield,PA) washed twice with hexane and dried for a few minutes before being washed again with hexane.

2.2.5 Viability Studies

To investigate the thermal enhancement properties of mild hyperthermia (42°C) on the different CDDP- SWNH complexes described above and on free CDDP, AY-27 cells were seeded on 12-well tissue culture polystyrene dishes at 20,000 cells per well and were incubated for 24 h to reach their exponential growth phase. Following the incubation period, cells were exposed independently to each type of the SWNH-CDDP conjugates or free CDDP suspended in cell media at 37°C or 42° for 1 h. The concentrations of SWNHs and CDDP were selected based on clinically-relevant doses. The concentration of free CDDP studied was 50 µM (.015 mg/mL) which was selected after performing a parametric analysis on concentration of CDDP for 1 hr that resulted in approximately 50% viability to achieve IC50 for all studies. Concentrations of 0.01 mg/mL of CDDP_INC_SWNHs and CDDP@SWNHs were chosen as this concentration results in the same order of magnitude of CDDP exposure and is achievable in vivo at the tumor site [22, 34]. As mentioned previously, SWNHs were selected due to their ability to act as both drug delivery vehicles and photothermal heat generators under

NIR. However, in this study an isothermal water bath (Lab RTE& water bath system; Thermo Scientific; Albuquerque, NM) set either to 37 °C or 42°C was used to heat the samples to minimize spatial temperature variation within wells (compared to laser heating) and between samples which would confound interpretation of the influence of a specific temperature on cell viability and uptake. However, we have shown SWNHs at concentrations of 0.01 mg/mL can easily be used to generate temperatures of 42° when irradiated with a laser Immediately following the 1 h exposure of either the CDDP-SWNHs or free CDDP, the samples were washed with ice cold PBS three times to remove any residual SWNHs or CDDP from the cell surface and to halt endocytosis processes which could result in additional nanoparticle uptake. Cells were then cultured in fresh RPMI 1640 supplemented medium for 72 h and viability was assessed using an Alamar blue metabolism assay (Life Technologies, Grand Island, NY) using a standard manufacturer's procedure. Briefly, a 10% Alamar blue solution was added to each well of the 12-well plates and the samples were incubated for 3 h to allow for colormetric change. Then, 100 μL aliquots were taken from each sample in triplicate and placed into a clean 96-well plate, totaling 24 reads per group (n=8). Absorbance was then measured with a SpectraMAX M2e microplate reader (Molecular Devices; Sunnyvale, CA) at 570 and 600 nm. The resulting viability was expressed as a mean value ± sample standard deviation. The significance of the results was verified with a Student's t-test and a 95 or 99% confidence was used to signify statistical significance between groups.

2.2.6 Cellular Uptake

In order to measure the influence of hyperthermia on drug delivery, the effect on uptake must be elucidated. Since CDDP acts on DNA, the cellular uptake of the SWNH-QDs was examined utilizing fluorescence-activated cell sorting (FACs) and fluorescence microscopy. AY-27 cells were seeded in tissue culture treated polystyrene 6-well dishes at 200,000 cells per well for each timepoint (0, 30, and 60 minutes) and were incubated for 48 h to reach a confluency of greater than 50%, during which the

medium was changed every 24 h. SWNH-QDs were diluted in RPMI 1640 medium to a final concentration of 0.01 mg/mL and were sonicated for approximately 15 seconds prior to all experiments. The cells were then exposed to SWNH-QD for 0, 30, and 60 minutes at either 37 or 42°C in an isothermal water bath. After treatment, cells were rinsed three times with ice cold PBS to remove any unbound SWNH-QDs. Cells were then trypsinized and centrifuged at 120 G for 5 min at 4° C. The cell pellet was then resuspended in fresh culture media at a final cell concentration of 1×10^6 cells/mL. Cell suspensions were then maintained on ice until they were analyzed with a BD Biosciences FACSARIA cell sorter (San Jose, CA). A 488 nm excitation source was used with a 610/620 nm emission filter and a 595 nm long pass filter. Cellular debris was excluded with a forward vs. side scatter gate and aggregations were excluded. Gating was utilized using a negative sample and the data was expressed as median fluorescence intensity along with a percent positive cell population. In addition to this experiment, another cellular uptake study was performed using a preheat stress in which the cells were exposed to 42°C for either 2 or 4 h and then allowed to return to 37° for 2 h prior to exposure of SWNH-QD at 37°C. This preheat study eliminates the effects of thermally enhanced transport on cellular uptake and instead focuses on cellular changes that could affect endocytotic processes.

Confocal microscopy was used to evaluate the cellular distribution of SWNH-QDs to confirm that nanoparticles were being internalized by the cells and not merely attached to the cell membrane. To accomplish this, cells were seeded in an identical manner as the FACs study, and cellular distribution at 60 minutes was characterized. Following ice cold PBS washes, the cells were fixed in 3.7% Paraformaldehyde (MP Biomedicals; Solon, OH) for 15 minutes. Cells were then rehydrated and their membranes were permeablized with 0.5% Triton-X (Sigma Aldrich; St. Louis, MO) for 15 minutes and blocked with 1% BSA (Santa Cruz Biotech; Santa Cruz, CA) for 1 h. 20 nM Oregon Green 488 Phalloidin (Invitrogen; Grand Island, NY) was then used to image the cytoskeleton. DAPI (Invitrogen;

Eugene, OR) was added for 5 minutes prior to imaging in order to view the nucleus. A Zeiss LSM510 confocal microscope (Carl Zeiss AG; Oberkochen, Germany) was used. Nanoparticles were viewed for their spatial relationship with the nucleus and cytoskeleton in an effort to show internalization.

2.2.7 Release of CDDP from CDDP-SWNH Conjugates

The release kinetics of CDDP from the two CDDP-SWNH conjugates was determined using a size exclusive dialysis based experiment. For both the CDDP_INC_SWNHs and the CDDP@SWNHs, 2 mg of the conjugate formed with a 1:1 w/w CDDP was dispersed in 10 mL of dH20 inside of a dialysis membrane cellulose tube (Spectra/Por, Spectrum Laboratories INC; Rancho Dominguez, CA; MWCO~10,000D). The molecular weight cutoff of the tubing allowed for free CDDP to diffuse across the membrane, but prevented diffusion of SWNHs or CDDP-SWNH conjugates. The dialysis membranes containing the CDPP-SWNH conjugates were immersed in 400 mL of dH20. 20 mL of the solution outside of the tubing was taken for each timepoint (0-12h) and the CDDP concentration was determined by measuring Pt concentration using ICP-AES. The release % compared to the 12 hour timepoint was expressed as a function of time.

2.3 RESULTS

2.3.1 Nanoparticle Characterization
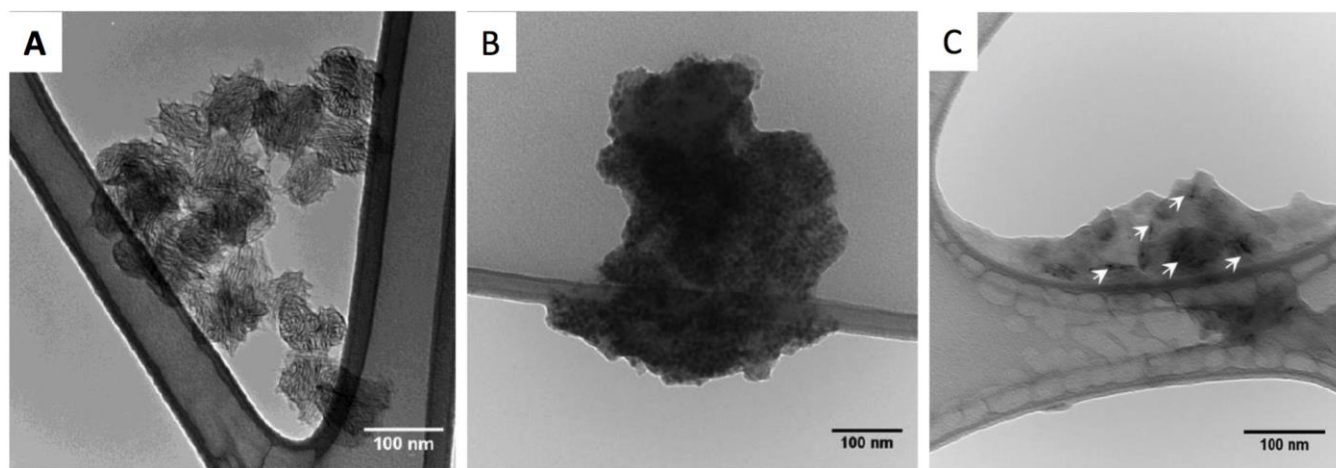
Figure 2: (A) TEM image showing dahlia shape of pristine SWNHs with an average diameter of 80 nm. (B) TEM image

showing high contrast QDs (dark aggregations) on an aggregate of SWNHs attached to lacey carbon mesh. (C) TEM with white arrows illustrating successful incorporation of CDDP (dark aggregations) in SWNHs

As illustrated in Figure 1, the SWNHs used in this study were examined using high contrast TEM imaging to confirm the size of the nanoparticles and the presence of QDs attached to the SWNH surface and cisplatin either within the interior or on the surface of the SWNH for their respective experiments. Figure 2 (A) shows the unique dahlia shape of the SWNHs which is utilized for high drug loading by harnessing both the extensive surface area and large internal volume. This figure also shows the average diameter of the SWNHs to be approximately 80 nm which corresponds with values for increased EPR effects that result in the greatest uptake in the tumor microenvironment [27].Figure 2(B) demonstrates our ability to attach QDs to the surface of the SWNHs which enabled imaging and uptake quantification of the SWNH-QD conjugates. The average diameter did not increase significantly with the addition of QDs to the SWNH surface thereby serving as a representative structure for determining the uptake of CDDP-SWNH conjugates. The white arrows in Figure 2(C) illustrates the aggregates of CDDP inside of the SWNHs with white arrows, which confirms our methods used for incorporating the CDDP into the SWNHs used in the viability studies to determine thermal enhancement properties., Overall the results from this study confirm the existence of both the fluorescent beacons (QDs) and the drug payload (CDDP) which is critical for our analysis of the influence of hyperthermia on drug efficacy and uptake in AY-27 rat bladder cells.

2.3.2 Viability studies:
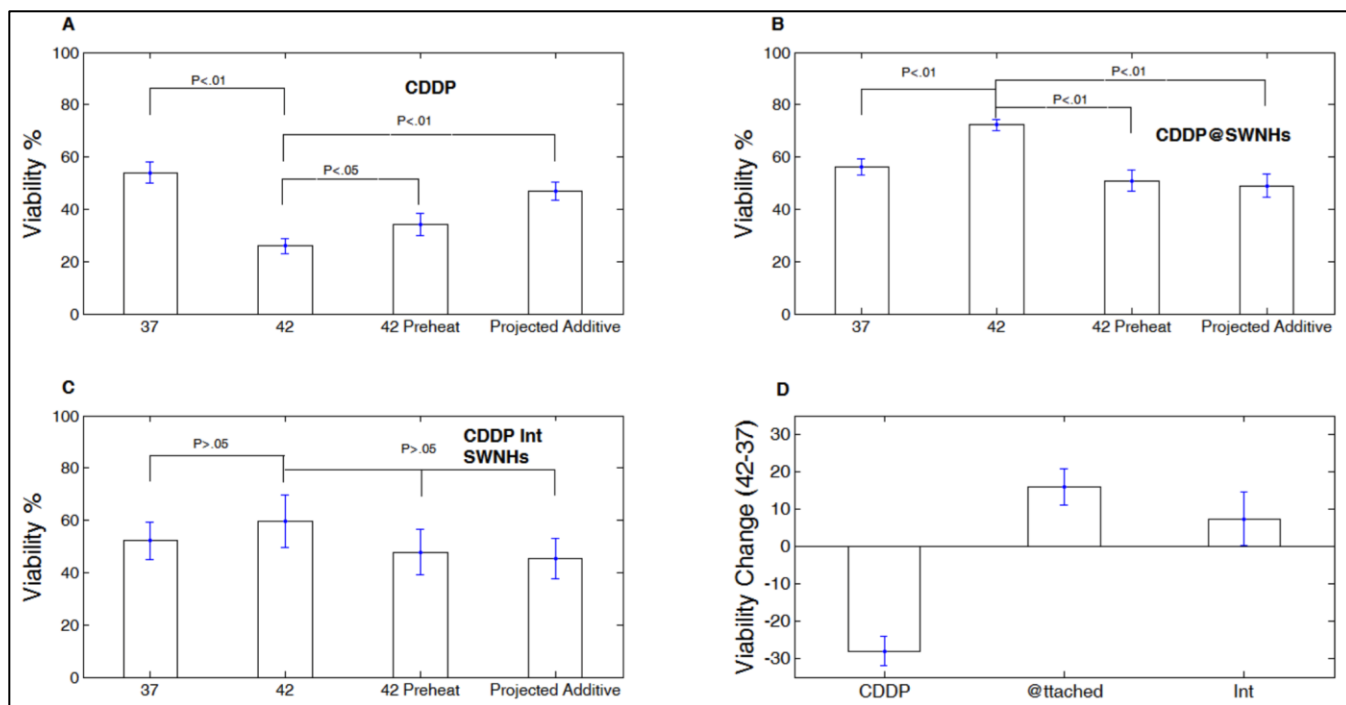
Figure 3: Proliferation(viability) data for AY-27 cells exposed to one of three(a-c) CDDP regiments and the effect of mild hyperthermia on the efficacy of the treatment. (A) provides viability data for Free CDDP exposed to the cells for 1 h for 3 heating profiles explained in methods and compares to the projected additive of mild hypothermia and CDDP. (B) provides similar data for CDDP@SWNHs and (C) shows the viability when the cells are exposed to CDDP_INC_SWNHs. (D) plots the difference between 42 and 37 exposure for the three types and highlights the changes in thermal enhancement

We determined the viability of AY-27 bladder cells following exposure to two types of CDDP-SWNH conjugates, incorporated and attached CDDP, and as a control for thermal enhancement, free CDDP, in AY-27 rat bladder cancer cells. Figure 3(A) plots the viability of 3 different treatment groups using a concentration of 50 μM CDDP after exposure for 72 h. The first group shown was exposed to free CDDP at 37°C and the average viability of the groups (n=8) was 54%. As mentioned in the methods, the concentration was chosen to be clinically relevant and induce approximately 50% cell death at 37°C. Since CDDP is a chemotherapeutic drug that is known to have synergy with heat, an additional group of cells exposed at 42°C was studied and the resulting viability was determined to be 26%. The projective additive which is the viability expected if there was no interplay between heat and CDDP is calculated for this treatment by multiplying the survival fractions of exposure to 42°C with no CDDP with the survival fraction of cells exposed to CDDP at 37°C [4]. The projected additive

interaction was surpassed in this study, proving synergism between the mild hyperthermia and CDDP ($p<0.01$). Additionally, the cells preheated at 42°C for 2 hr showed mild synergism between the CDDP exposure and heat with an overall viability of 38% which was significantly lower than the projected additive($p<0.05$)

Figure 3(B) shows the viability of cells following exposure to CDDP@SWNH conjugates under identical thermal conditions as Figure 3(A). The measured viability for the cells exposed to CDDP@SWNHs at 37°C was 56%. Unlike the free CDDP group, the CDDP@SWNHs exposed at 42°C resulted in a viability of 72%, a significant increase in viability compared to 37°C ($p<0.01$). The preheated samples showed no significant difference between the cells exposed at 37°C and each group resulted in a higher viability than the projected additive meaning there was no synergism seen with heat as there was with the free CDDP studies.

The viability of the CDDP_INC_SWNHs under identical thermal conditions is plotted in Figure 3(C). Cells exposed to the incorporated conjugates at 37°C had an average viability of 52%. Cells exposed to 42°C had a slightly, non-significantly, higher viability at 59% which was greater than the 47% viability shown in the preheated samples. Like the CDDP-SWNH conjugates, the internalized groups showed no thermal enhancement when compared to the projected additive.

When examining the viability of samples after exposure to CDDP@SWNHs and CDDP_INC_SWNHs, the thermal enhancement observed with free CDDP was not only minimized but reversed when combined with heat, even though they had similar IC50 compared to the CDDP-SWNH conjugates at 37°C. The combined results are shown in Figure 3(D), with the viability difference between 42°C and 37°C indicating a negative -28% for the free CDDP. In contrast to this decrease in viability, a positive, or increase in viability, of 15.88% for CDDP@SWNH and 7.42% for CDDP_Inc_SWNH is seen when comparing 42°C and 37°C exposures.

In order to elucidate the mechanism causing the difference in viability observed for hyperthermia in combination with SWNH-CDDP conjugates as compared to free CDDP, we investigated whether this phenomena was due to decreased cellular uptake of the nanoparticles. Cells exposed to 0.01 mg/mL SWNH-QDs for 0, 30, and 60 minutes at either 37°C or 42 °C were measured via flow cytometry to determine quantitatively, the amount of nanoparticles uptaken and the influence of hyperthermia on cellular uptake. Figure 4 displays the results of this study as both a median fluorescence signal (A) and % positive gated cells (B). It is apparent from the data that mild hyperthermia causes a statistically significant ($p<0.01$) decrease in uptake at 42° when compared to 37°C, which is determined from the decrease of 219.7 relative fluorescent units down to 145, a change in almost 35% (n=6-8). Additionally, a negative sample without exposure to SWNH-QDs was used (figure 4(C)) for gating purposes to allow for a percent of population containing the SWNH-QDs to be calculated (4(D) and (E)). The viability decline from 66.2% to 45% when exposed to 42°C for one hour (figure 4(B)) may be attributed to the decrease in treatment efficacy of these SWNH-CDDP conjugates.
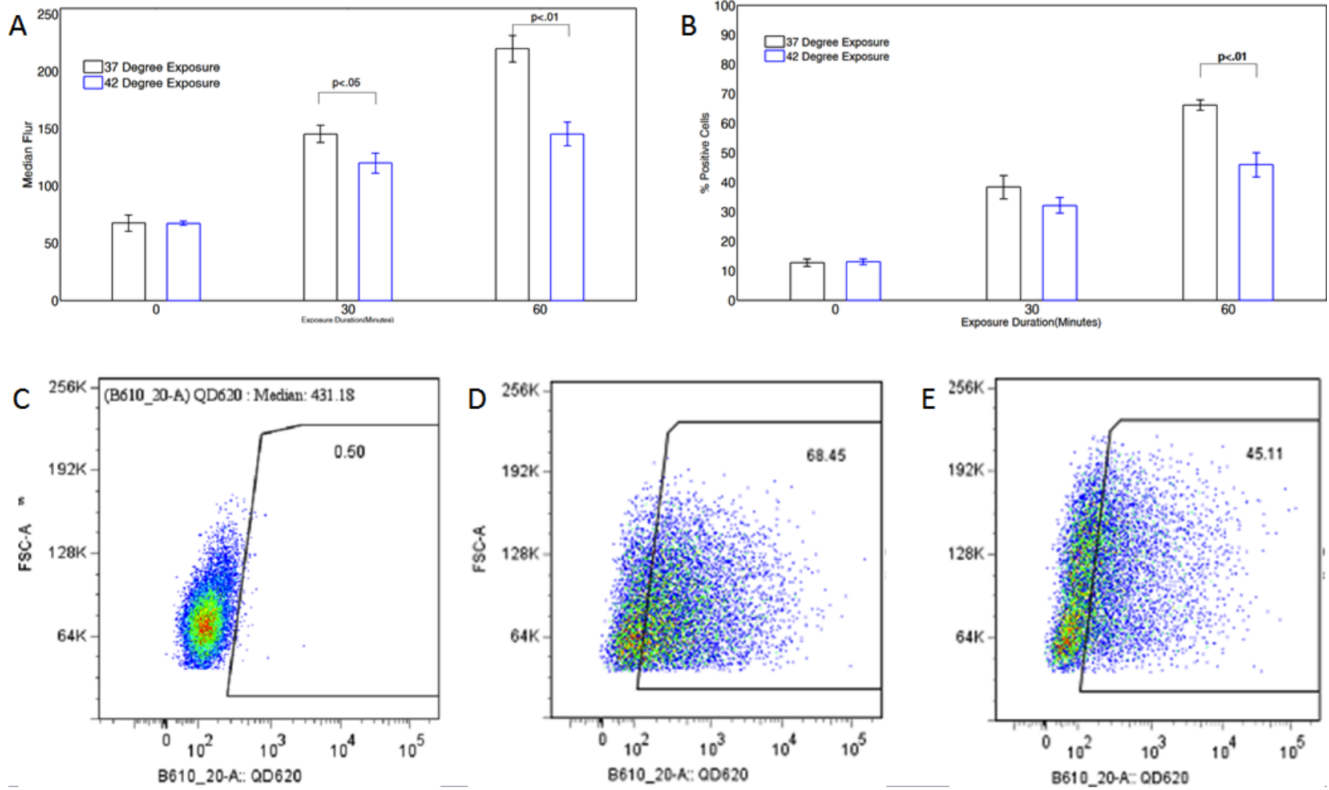
Figure 4: Uptake of SWNH-QD by AY-27 cells under normal physiological conditions (37°C) and hyperthermia(42°C) determined by FACS cytometry. (A) shows the median fluorescent intensity of the cells from 0-60 minutes exposure of heat and SWNH-QD. (B) plots the % positive cells determined by gating the fluorescence signal from (c) a control sample. (D) and (E) are representative data from 37 and 42 °C for 1 hr respectively showing a sharp decrease in both fluorscensce intensity and % gated positive

While the FACs system provides valuable data, it lacks the ability to determine the intracellular distribution of nanoparticles to confirm uptake. In order to determine the cellular distribution of SWNH-QDs following exposure, immunofluorescence staining of the nucleus and cytoskeleton was performed and imaged with confocal microscopy. Figure 5 shows representative images of cellular uptake of SWNH-QDs at 37°C (A-C) and under mild hyperthermia (42°C) (D-F). Cell nuclei were stained with DAPI (Figure 5 (c) and (f)) and the cytoskeleton (F-actin) was stained with Phalloidin and shown in Figure 5 (B) and (E) in order to visualize the localization of the nanoparticles. Figure 5 (A) and (D) provide brightfield images which show the localization and aggregation of SWNH-QDs inside of the cell after numerous cold PBS washes and 24 hour incubation in fresh medium. The larger black dots observed in (A) and (D) infers strongly that the SWNH-QDs are endocytosed and aggregate within the

25

cytoplasm. The F-actin stain seen in (B) and (E) confirm location of the particles inside the cell, not just attached to the membrane, confirming uptake. Nuclear stains(C) and (F) illustrate the location of the SWNH-QDs after 24 h of incubation and show that the delivered cisplatin should be capable of interacting with the nucleus due to its close proximity after 24 h.
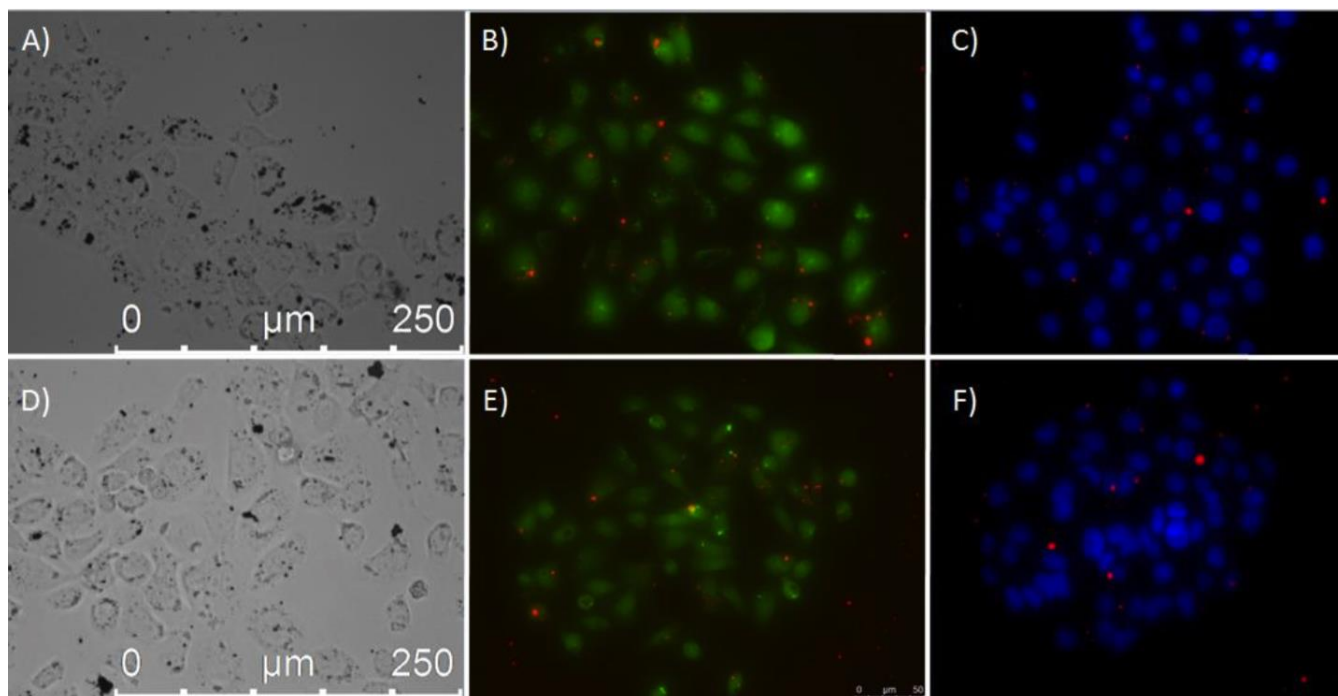
Figure 5: (A) and (D) are brightfield images 24 hours after exposure to 0.01mg/mL SWNH at 37 and 42°C respectively, showing a decrease in uptake at 42 which is seen by a decrease in black dots. (B) and (E) are stained for the cytoskeleton shich show internalization of the nanoparticles at 37 and 42°C respectively and (C) and (F) are stained with DAPI, showing internalization of the nanoparticles reaches the nucleus

The cell viability following exposure to 42°C for two hours followed by a two hour relaxation period and subsequent exposure at 37°C was accomplished Figure 6(A-C). These data provide information to cellular events due to hyperthermia that may not be active during drug and nanoparticle transport, but may have ultimately affected the efficacy of the drug. It was determined for CDDP@SWNHs and CDDP_INC_SWNHs that the preheat stress caused no change in treatment efficacy. In order to determine if this may also hold true for the uptake, cells underwent a similar heating regimen followed by exposure of the SWNH-QDs to 37°C. The data for median fluorescence intensity

was plotted for a control sample of cells exposed to 37 degrees and a 1 and 2 hour preheat group. Results from this study show that there was not a significant difference in uptake in the three samples (~50% uptake).
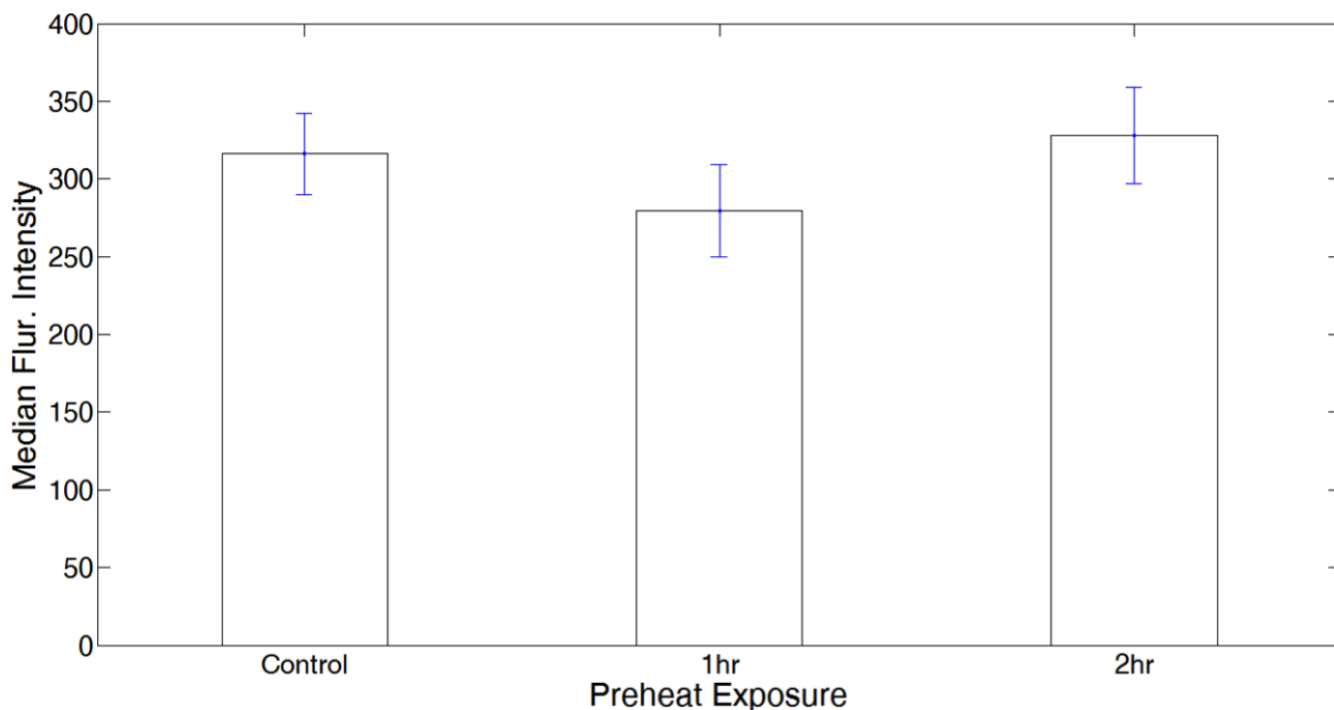
Figure 6: The median Fluorescent intensity for 2 different preheat stresses of 42 °C are compared to the control non-heated samples. Cells were exposed to 0.01 mg/mL SWNH-QD for 1 hour and fluorescent intensity was measured via FACs.

The difference in viability observed between the CDDP@SWNHs and CDDP_INC_SWNHs when exposed to 42°C was noted from the viability studies and implies a change in mechanism of action. This deviation cannot be explained by a difference in uptake, since the size and charge of the particles remains the same and the data from the SWNH-QD experiments should hold true for both of these groups. To determine potential differences between the samples, release rates of CDDP were measured over a 12 h time period for both of the CDDP-SWNH conjugates and the results were plotted in Figure 7. The greatest difference observed exists for the two sets of conjugates. The CDDP@SWNHs possess an immeasurable amount of CDDP released from the SWNHs for all time points most likely due to the strong covalent bond which was not broken within the 12 h period. The CDDP_INC_SWNH at

exposed to both 37 and 42° exhibit a time dependent release profile with majority of the CDDP being released within the first 4 h. It should also be noted that an increase in drug release in the first hour is evident in the sample exposed to 42° compared to the 37°C ($p<0.05$).
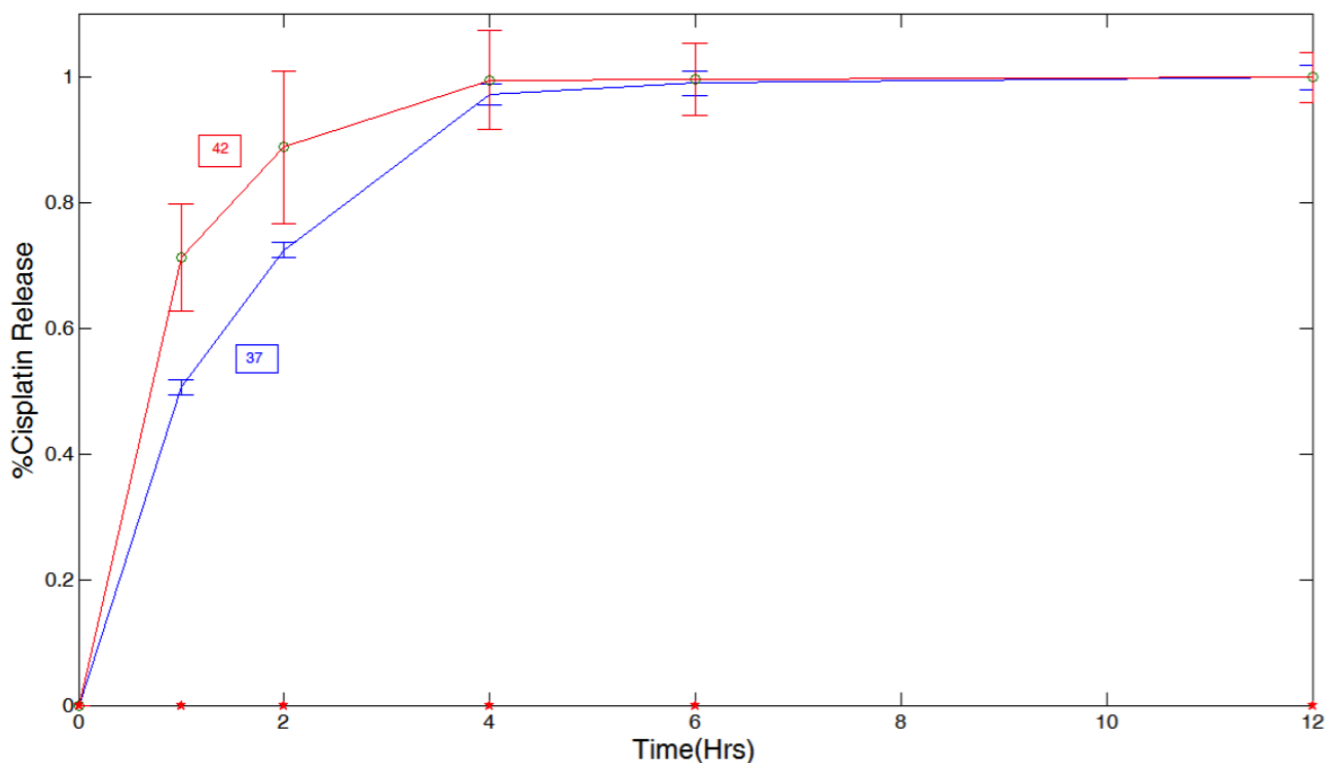
 Figure 7: Release of CDDP from CDDP_Inc_SWNH (red and blue lines) and CDDP@SWNH(red dots along x-axis). The quantities of CDDP released into 400 mL water were measured via ICP-AES for platinum concentration

2.4 DISCUSSION

While other groups have previously explored the capability of photothermal heat absorbing nanoparticles to enhance the delivery and efficacy of chemotherapeutic agents such as cisplatin or doxorubicin, their experimental designs only included the nanoparticles as heat sources and not as a drug delivery vehicle [25]. This results in potentially higher efficacies as cellular uptake of the nanoparticles, and more importantly how the photothermal generated hyperthermia affects the uptake of nanoparticles, is excluded from these studies. Since our objective is to utilize the nanoparticles as both heat absorption and drug delivery vehicles, studying the efficacy and transport kinetics of the drug- nanoparticle

conjugate in a hyperthermic environment is critical. We conducted experiments to determine the effect of hyperthermia on CDDP-SWNH conjugates by evaluating the degree of cell death, uptake, and drug release. While our study does neglect many of the important steps prior to the nanoparticle interacting with the cancer cell such as interaction with blood, extravasation into the tumor site, and drug clearance, this study provides insight into the appropriate method to enhance thermal mediated chemotherapy for alternate drug conjugate designs due to differences seen in our two CDDP- SWNH conjugates.

After TEM imaging was utilized to confirm the creation of the CDDP-SWNH conjugates, the capability of heat to enhance the efficacy of free CDDP in media was determined by measuring the cell viability following treatment using the AY-27 bladder cancer cell line. It was shown that the decrease in viability when free CDDP was exposed to 42°C compared to 37°C was nearly 30% lower (Figure 3(D), CDDP). These values are similar to prior reported literature for the breast cancer cells, MCF7, in vitro which were similarly exposed to hyperthermia of 43°C[25] .The decrease in viability observed with the addition of elevated temperatures likely corresponds to an increase in diffusion of the cisplatin into the cells due to increased membrane fluidity at the higher temperature [5]. As can be noted from Figure 4(A) there is a significant decrease in viability in response to the 42°C exposure compared to the projected additive which further proves synergy in the treatment. Additionally data from the preheat experiments imply synergism is possible even prior to exposure which has been shown before in clinical studies involving human bladders in which the timing was shown to be important for drug enhancement with heat [40].

We investigated whether thermal enhancement occurred when CDDP@SWNHs in which the CDDP was covalently attached to the surface of SWNHs and CDDP_INC_SWNHs in which CDDP was located in the interior space of the SWNH were exposed to 42°C for 1 hr. Compared to the thermal enhancement of free CDDP, we observed an increase in viability when cells were exposed to 42°C and

either CDDP@SWNHs or CDDP_INC_SWNHs ($p<0.01$) (Figure 3B). Furthermore, cells preheated to 42 °C and exposed to CDDP@SWNHs or CDDP_INC_SWNHs exhibited a similar viability as the cells maintained at 37°C, indicating the importance of concurrent heating to cellular uptake and drug efficacy. These results contradict other in vitro studies which show greater efficacy of CDDP when exposed to gold nanorods and NIR heating (viability decrease of almost 30% for MCF-7 cells) compared to CDDP alone, resulting in [25]. These gold nanorods however, were not used to traffic the drug into the cells and only employ the nanorods as a localized heat source. While these studies can show efficacy in vitro, they do not provide a system that is capable of delivery of both heat and drugs in vivo. Our SWNH system demonstrates the need for a drug delivery vehicle as well as a platform for photothermal enhancement.

The difference between our lack of enhancement and enhancement previously shown with work by others with nanoparticle mediated photothermal-chemotherapy[4, 23, 25] led us to examine the mechanism causing thermal enhancements of free CDDP as opposed to the decreased toxicity observed for CDDP-SWNH conjugates in combination with heat. There exists a large size difference between free CDDP (4 angstrom) and CDDP-SWNH conjugates (~100nm). The size of free CDDP should permit simple diffusion across the cell membrane[12] while the CDDP-SWNH conjugates may necessitate endocytosis in order to enable uptake. Chithrani et al found that spherical gold nanoparticles of 50 nm diameters, which are of similar size to our CDDP-SWNH conjugates, were endocytosed, which implies that endocytosis should be the main mechanism of intracellular transport [41]. With this in mind, we investigated the influence of hyperthermia on cellular uptake of the nanoparticles and thus the drug's ultimate intracellular concentration through endocytosis. Studies of QD labeled SWNH conjugates confirmed that hyperthermia, while allowing for greater diffusion of smaller particles, may diminish endocytosis and halt the larger nanoparticle from entering which is not seen with the smaller moieties.

These results imply that a delivery system that utilizes a heating mechanism, but requires entrance of the nanoparticle into the cells for the drug to function, may encounter an extra barrier to treatment efficacy. This decrease in uptake almost certainly explains why the treatments at 42°C with the CDDP- SWNH conjugates resulted in lower efficacy compared to free CDDP, since these nanoparticles did not enter cells and the drug was unable to act during the 72 hour incubation period. The results from our microscopy study (Figure 5) confirm the quantitative data that SWNHs are internalized since they are evident in the same focal plane as the cytoskeleton and nucleus and do not correspond to just surface attached SWNHs which would have no effect on drug efficacy.

In addition to the uptake studies in Figure 4, the preheat stress studies help confirm that the decrease in efficacy of the CDDP-SWNH conjugates is due to reduced internalization. Figure 6 shows that for both preheat stress periods (1 and 2 h), the amount of CDDP-SWNH conjugate uptake is unaffected. Likewise, the viability of the preheated samples compared to the samples maintained at 37°C when exposed to CDDP-SWNH conjugates was statistically insignificant. This likely indicates that the preheat stress did not affect non-hyperthermic cellular events and subsequent endocytotic uptake. It has been shown that a preheat stress is capable of inducing unknown cellular changes which result in synergism with CDDP [42, 43]. By studying the uptake of CDDP-SWNH conjugates as a function of the preheat stress, the amount of drug exposed to the cells is unchanged because of a lack of modification in internalization. This preheat stress data confirms that the decrease in uptake occurring in response to hyperthermic conditions results in a decreased activity of the CDDP-SWNH conjugates.

While the uptake data of the SWNH-QDs provided an explanation for the decreased efficacy of the CDDP-SWNH conjugates under mild hyperthermia, it did not explain the differences observed between the conjugation methods. CDDP@SWNHs exhibited a greater decrease in thermal enhancement and had a statistically significant thermal hindrance, or increase in viability. The drug

release studies shown in figure 7 did provide an explanation between the differences observed in the two CDDP-SWNH conjugates. Because the attached drug in the case of CDDP@SWNHs is covalently linked to the SWNH, CDDP is only capable of entering the cell whenever the SWNH enters. The attached CDDP was not released in the 12 h time period during exposure to either 37 or 42°C. This indicates that the internalization of the CDDP@SWNH would have a larger role in the overall efficacy of treatment. The CDDP_INC_SWNHs exhibit a release profile in which most of the drug that exits the complex does so in the first 4 hours. This means that during the one hour exposure, the drug is free to enter the cell via both diffusion and endocytosis, thus minimizing the effect of uptake on treatment efficacy. Further supporting the difference in viability between the two CDDP-SWNH conjugates at 42°C is the increased release profile in the first hour at 42°C compared to 37°C for the CDDP_INC_SWNH. The results from the interior loaded CDDP follow similar trends to Ajima's group in which cisplatin was incorporated within SWNHs [34]. However, his group did not explore the effect of hyperthermia on release. Our results imply that if more CDDP can interact with the cell prior to being uptaken as a complex, and capitalize on hyperthermic conditions to enter the cell through increased diffusion overall efficacy might be increased. Therefore, a particle that uses this difference in temperatures to release more drug load at the target site prior to uptake could achieve the thermal enhancement associated with free drug, but eliminate side effects..

Based upon the results from this study, we believe that the most efficacious thermo-chemotherapy treatments would selectively release the payload at the tumor site prior to uptake of the particle. One particular method for this to occur is through a thermally responsive polymer that acts as a linker between the heat generating nanoparticle core and the reactive drug species such as CDDP. Currently there is research utilizing thermally responsive polymers to trigger a drug release at certain temperatures, but there is little work into combining these polymers to the photo-absorbing, heat

generating nanoparticles capable of localized heating, as most of these still rely on more traditional regional heating [44, 45]. The combination of these two technologies may provide the optimal platform for combined delivery of heat and drug .

2.5 CONCLUSION

We have compared two methods to conjugate cisplatin with single walled carbon nanohorns for use in photothermal-chemotherapy treatments. CDDP was successfully loaded into and attached to NIR absorbing SWNHs. The CDDP-SWNH conjugates were examined for their potential as thermal enhancing drug carriers capable of synergism between heat and drug. Unlike free CDDP, no thermal enhancement of the efficacy of the CDDP-SWNHs around the IC50 of the drug in vitro was observed. FACs and microscopy were used to confirm a decrease in uptake of the conjugates at 42°C which was most likely responsible for the decrease in efficacy. Release profiles of CDDP from the two nanoparticle conjugates indicate that careful consideration should be made to ensure the drug payload is released prior to uptake by the tumor cells to allow for full thermal enhancement. We envision a combination therapy that is capable of localized delivery of heat and chemotherapeutic drugs to the extracellular space of a tumor that will allow for optimized synergism between the modalities, impacting the treatment of bladder cancer and other malignancies.

2.6 ACKOWLEDGMENTS

2.7 References:

1. Yuan, Y., et al., Utility of treatment planning for thermochemotherapy treatment of nonmuscle invasive bladder carcinoma. Med Phys, 2012. 39(3): p. 1170-81.
2. Moskovitz, B., et al., Thermo-chemotherapy for intermediate or high-risk recurrent superficial bladder cancer patients. Annals of Oncology, 2005. 16(4): p. 585-589.
3. Bronk, B.V., R.J. Wilkins, and J.D. Regan, Thermal enhancement of DNA damage by an alkylating agent in human cells. Biochem Biophys Res Commun, 1973. 52(3): p. 1064-70.
4. Hahn, G.M., Potential for Therapy of Drugs and Hyperthermia. Cancer Research, 1979. 39(6): p. 2264-2268.
5. Gabano, E., et al., The influence of temperature on antiproliferative effects, cellular uptake and DNA platination of the clinically employed Pt(II)-drugs. Journal of Inorganic Biochemistry, 2008. 102(4): p. 629-635.
6. Itoh, Y., et al., Combination of chemotherapy and mild hyperthermia enhances the anti-tumor effects of cisplatin and adriamycin in human bladder cancer T24 cells in vitro. Experimental and Therapeutic Medicine, 2010. 1(2): p. 319-323.
7. Gofrit, O.N., et al., Combined local bladder hyperthermia and intravesical chemotherapy for the treatment of high-grade superficial bladder cancer. Urology, 2004. 63(3): p. 466-471.
8. Issels, R.D., Hyperthermia adds to chemotherapy. European Journal of Cancer, 2008. 44(17): p. 2546-2554.
9. Oliveira, T.R., et al., Preclinical Dosimetry of Magnetic Fluid Hyperthermia for Bladder Cancer. Energy-Based Treatment of Tissue and Assessment Vii, 2013. 8584.
10. Ohno, S., et al., Thermal Enhancement of Drug Uptake and DNA-Adducts as a Possible Mechanism for the Effect of Sequencing Hyperthermia on Cisplatin-Induced Cytotoxicity in L1210 Cells. Cancer Chemotherapy and Pharmacology, 1994. 34(4): p. 302-306.
11. Kaufmann, S.H. and W.C. Earnshaw, Induction of apoptosis by cancer chemotherapy. Experimental Cell Research, 2000. 256(1): p. 42-49.
12. Ghezzi, A., et al., Uptake of antitumor platinum(II)-complexes by cancer cells, assayed by inductively coupled plasma mass spectrometry (ICP-MS). J Inorg Biochem, 2004. 98(1): p. 73-8.
13. Bull, J.M., A review of systemic hyperthermia. Front Radiat Ther Oncol, 1984. 18: p. 171-6.
14. Wust, P., et al., Hyperthermia in combined treatment of cancer. Lancet Oncol, 2002. 3(8): p. 487- 97.
15. Yildiz Bayatzitoglu, S.K., Toni K. Tullius, An overview of nanoparticle assisted laser therapy. International Journal of Heat and Mass Transfer, 2013. 67: p. 17.
16. Feng, Y. and D. Fuentes, Model-based planning and real-time predictive control for laser-induced thermal therapy. Int J Hyperthermia, 2011. 27(8): p. 751-61.
17. von Maltzahn, G., et al., Computationally Guided Photothermal Tumor Therapy Using Long-Circulating Gold Nanorod Antennas. Cancer Research, 2009. 69(9): p. 3892-3900.
18. Huang, H.C., K. Rege, and J.J. Heys, Spatiotemporal Temperature Distribution and Cancer Cell Death in Response to Extracellular Hyperthermia Induced by Gold Nanorods. Acs Nano, 2010. 4(5): p. 2892-2900.

19. Kessentini, S. and D. Barchiesi, Quantitative comparison of optimized nanorods, nanoshells and hollow nanospheres for photothermal therapy. Biomedical Optics Express, 2012. 3(3): p. 590-604.
20. Fisher, J.W., et al., Photothermal response of human and murine cancer cells to multiwalled carbon nanotubes after laser irradiation. Cancer Res, 2010. 70(23): p. 9855-64.
21. Iijima, S., et al., Nano-aggregates of single-walled graphitic carbon nano-horns. Chemical Physics Letters, 1999. 309(3-4): p. 165-170.
22. Whitney, J.R., et al., Single Walled Carbon Nanohorns as Photothermal Cancer Agents. Lasers in Surgery and Medicine, 2011. 43(1): p. 43-51.
23. Ren, F., et al., Gold Nanorods Carrying Paclitaxel for Photothermal-Chemotherapy of Cancer. Bioconjugate Chemistry, 2013. 24(3): p. 376-386.
24. Su, D., R.H. Ma, and L. Zhu, Numerical study of nanofluid infusion in deformable tissues for hyperthermia cancer treatments. Medical & Biological Engineering & Computing, 2011. 49(11): p. 1233-1240.
25. Hauck, T.S., et al., Enhancing the Toxicity of Cancer Chemotherapeutics with Gold Nanorod Hyperthermia. Advanced Materials, 2008. 20(20): p. 3832-+.
26. Zhang, W., et al., Synergistic effect of chemo-photothermal therapy using PEGylated graphene oxide. Biomaterials, 2011. 32(33): p. 8555-8561.
27. Peer, D., et al., Nanocarriers as an emerging platform for cancer therapy. Nature Nanotechnology, 2007. 2(12): p. 751-760.
28. Maruyama, K., Intracellular targeting delivery of liposomal drugs to solid tumors based on EPR effects. Advanced Drug Delivery Reviews, 2011. 63(3): p. 161-169.
29. Brannon-Peppas, L. and J.O. Blanchette, Nanoparticle and targeted systems for cancer therapy. Advanced Drug Delivery Reviews, 2004. 56(11): p. 1649-1659.
30. Kong, G., R.D. Braun, and M.W. Dewhirst, Hyperthermia enables tumor-specific nanoparticle delivery: Effect of particle size. Cancer Research, 2000. 60(16): p. 4440-4445.
31. Byrne, J.D., T. Betancourt, and L. Brannon-Peppas, Active targeting schemes for nanoparticle systems in cancer therapeutics. Advanced Drug Delivery Reviews, 2008. 60(15): p. 1615-1626.
32. Azami, T., et al., Large-scale production of single-wall carbon nanohorns with high purity. Journal of Physical Chemistry C, 2008. 112(5): p. 1330-1334.
33. Ajima, K., et al., Carbon nanohorns as anticancer drug carriers. Molecular Pharmaceutics, 2005. 2(6): p. 475-480.
34. Ajima, K., et al., Enhancement of In Vivo Anticancer Effects of Cisplatin by Incorporation Inside Single-Wall Carbon Nanohorns. Acs Nano, 2008. 2(10): p. 2057-2064.
35. Whitney, J., et al., Spatiotemporal Temperature and Cell Viability Measurement Following Laser Therapy in Combination with Carbon Nanohorns. Proceedings of the Asme Summer Bioengineering Conference, 2010, 2010: p. 79-80.
36. Whitney, J., et al., Carbon Nanohorns as Photothermal and Photochemical Laser Cancer Therapeutic Agents. Lasers in Surgery and Medicine, 2009: p. 3-3.
37. Hood, R.L., et al., Spatially controlled photothermal heating of bladder tissue through single-walled carbon nanohorns delivered with a fiberoptic microneedle device. Lasers in Medical Science, 2013. 28(4): p. 1143-1150.
38. Matsumura, S., et al., Dispersion of cisplatin-loaded carbon nanohorns with a conjugate comprised of an artificial peptide aptamer and polyethylene glycol. Molecular Pharmaceutics, 2007. 4(5): p. 723-729.

39. Bhirde, A.A., et al., Targeted Killing of Cancer Cells in Vivo and in Vitro with EGF-Directed Carbon Nanotube-Based Drug Delivery. Acs Nano, 2009. 3(2): p. 307-316.

40. Greco, C., et al., Effect of Sequential Application of Hyperthermia and Chemotherapy on the Survival of a Thermoresistant Human-Melanoma Cell-Line. Cancer Biochemistry Biophysics, 1987. 9(3): p. 223-232.

41. Chithrani, B.D., A.A. Ghazani, and W.C. Chan, Determining the size and shape dependence of gold nanoparticle uptake into mammalian cells. Nano Lett, 2006. 6(4): p. 662-8.

42. Mella, O. and O. Dahl, Timing of Combined Hyperthermia and 1,3-Bis(2-Chloroethyl)-1-Nitrosourea or Cis-Diamminedichloroplatinum in Bd-Ix Rats with Bt4a Tumors. Anticancer Research, 1985. 5(3): p. 259-263.

43. Douple, E.B., Effects of Hyperthermia in Combination with Radiation on Survival of Unfed, Plateau-Phase Cells. Radiation Research, 1976. 67(3): p. 576-576.

44. Chilkoti, A., et al., Targeted drug delivery by thermally responsive polymers. Adv Drug Deliv Rev, 2002. 54(5): p. 613-30.

45. Peng, J., et al., Controlled release of cisplatin from pH-thermal dual responsive nanogels. Biomaterials, 2013. 34(34): p. 8726-40.

Chapter 3: Tunable Collagen Based Microfluidic Platform to Study Nanoparticle Transport in the Tumor Microenvironment

Matthew R. DeWitt[1] and M. Nichole Rylander[2]

1.Virginia Tech- Wake Forest School of Biomedical Engineering and Sciences, Blacksburg VA

dewitt@vt.edu

2. Mechanical Engineering, University of Texas at Austin, Austin TX

Running head

Nanoparticle Transport in Tumor Platform

3.i. Abstract

This chapter describes the motivation and protocol for creating a perfused 3D microfluidic *in vitro* platform representative of the tumor microenvironment to study nanoparticle transport. Current research in early nanoparticle research and development commonly utilizes 2D cell culture. These models fail to effectively mimic the physiologically complex features of the *in vivo* tumor microenvironment key for understanding how environmental conditions and nanoparticle features impact transport. This limits the ability to optimize nanoparticle properties to enhance transport and localization in the target tumor site. The cylindrical vascularized tumor platform described consists of a central endothelialized microchannel surrounded by a collagen hydrogel matrix containing cancer cells. This system can be employed to investigate key nanoparticle transport events in the tumor such as extravasation, diffusion within the extracellular matrix, and nanoparticle uptake. This easily-manufactured tumor platform can be used for novel nanoparticle refinement focused on optimizing

nanoparticle features such as size, shape, and functionalization method. This can yield ideal nanoparticles with properties that facilitate increased transport within the tumor microenvironment; leading to more effective nanoparticle treatments for cancer including nanoparticle based drug delivery systems.

3.ii. Key Words

Tumor Engineering, Microfluidics, Nanoparticle Transport, Tumor Microenvironment, Drug-delivery

3.1. Introduction

The ultimate goal of nanoparticle based cancer therapy is to deliver a sufficient concentration of particles to a targeted tumor site, resulting in high treatment efficacy with minimal systemic toxicity [1]. Nanoparticles have shown promise in enhancing localized delivery of drug payloads at effective concentrations to achieve therapeutic benefit, highlighting their potential as drug-delivery systems [2,3]. Nanoparticles have also been utilized as antennas to direct external energy sources to deliver therapeutic heat to ablate tumors from within [4-7]. Biomedical application of nanoparticles is based on harnessing the unique pathophysiology of tumors to result in passive targeting and customizing features of nanoparticles to develop active targeting strategies that enhance specificity of particles [1]. Novel nanomedicines made of a variety of materials are currently studied including polymers[8,9], magnetic materials [10,11], gold [12-15], and a wide range of carbon nanoparticles [6,16-18]. With the ongoing development of novel materials and unique methods to create nanoparticles, new particles are being developed at increasing rates. Rigorous and established preclinical models are needed to optimize these novel particles in the early stages of research and development. The use of proven models to

study nanoparticle transport, will lead to improved therapeutic efficacy and functionality in future cancer treatments.

The efficacy of nanoparticle based tumor therapies relies on the ability of the particles to make their way from a vascular network to target tumor cells [19]. Along this journey, particles encounter a variety of different barriers to transport that regulate the ultimate particle concentration at their targeted site. The pro-angiogenic environment of the tumor, which is hypothesized to occur as the result of a rapidly growing vascular bed that feeds the expanding tumor, is known to result in a leaky vasculature, leading to localized transvascular nanoparticle transport[20]. The leakiness and lack of a functioning lymphatic bed leads to the well known enhanced permeability and retention (EPR) effect[21]. This phenomenon results in passive targeting for accumulation of particles <400 nm into the tumor [22,23]. Tumors were shown to have an order of magnitude larger endothelial pore size than healthy tissue, which corresponded to selective nanoparticle extravasation[24]. Nanoparticle transvascular transport is an important first step in nanoparticle tumor transport and can be modeled as a flux across a semi-permeable membrane down a pressure gradient and diffusion down a concentration gradient, which allows for coupling of experimental and *in silico* models[25]. Locally increasing nanoparticle extravasation at the tumor site should be studied in the early stages of nanoparticle formulations to develop more targeted and less toxic treatments[26].

After translocation across the tumor capillaries nanoparticles must travel through the tumor interstitium to the targeted tumor cells. The interstitial area of the tumor is known to be predominantly composed of collagen and other elastic fibers along with a matrix of extracellular biomacromolecules that together form an extracellular matrix (ECM)[27]. Unlike most healthy tissues, there is a high interstitial pressure due to the EPR effect that is known to limit NP

transport from the convective forces observed in healthy tissue with a functioning lymphatic bed[28]. Previous research has shown even with elimination of pressure gradients, penetration of macromolecules is hindered in the ECM resulting in nanoparticle transport exclusively by diffusion as particles larger than approximately 5 nm are known to undergo mass transport by diffusion once inside the tumor[29-31]. Netti et al have shown that transport of 68 kDa bovine serum albumin (BSA) can be significantly hindered in the interstitial area of xenograft tumor models and nanoparticles are typically 10-30 times larger than BSA[32]. The properties of nanoparticles including shape, size, surface charge, and solubility have been shown to affect their interaction with the ECM and can ultimately influence their mass transport[33,34]. Careful consideration of tumor interstitium/nanoparticle interactions is important to optimize novel nanoparticles that are capable of diffusing deep into the tumor to achieve efficacy. Thus novel nanoparticle therapies should be studied in a controlled environment before costly animal models are utilized as shown in Fig. 1(a) to determine nanoparticle extravasation and diffusion in the tumor.

Specific uptake of nanotherapeutics is another significant consideration when designing nanoparticles to achieve maximum therapeutic efficacy with minimal toxicity [35]. There have been many avenues of research to maximize localization of particles within the tumor volume and internalization of particles within cancer cells [36]. Surface modification including the attachment of targeting moieties such as small peptides and growth factors are currently the primary method for increasing targeted uptake[37]. Additionally it has been found that nanoparticle shape and size can play important roles in the process of internalization and therefore must be considered for optimization[38]. Current work has utilized tools such as flow activated cell sorting (FACS) and confocal imaging to study the dynamics of cellular uptake of

nanoparticles [39]. However, many of these studies are accomplished in 2D cell culture models and therefore may not accurately model the uptake process. Internalization or uptake of particles represents the last transport barrier nanoparticles must overcome in order to achieve therapeutic efficacy, and the role of uptake in the treatment process cannot be overlooked. While there is a broad research field focused in optimizing nanoparticle features for increased circulation or extravasation, these factors may compound other transport processes and therefore should be studied in parallel with particle uptake[40].

Many novel therapeutic and diagnostic nanoparticles have been developed and optimized utilizing *in vitro* studies; however there has been relatively minimal success in their *in vivo* translation These static *in vitro* models do not mimic transport processes that nanoparticles encounter in the tumor microenvironment and are primarily used to understand how particle features affect uptake by affecting their interaction with cell membrane byendocytosis [41]. In order to develop nanoparticles that achieve successful delivery to the targeted tumor site, the particles should be developed and studied considering these complex multiscale transport barriers including extravasation, diffusion, and cellular uptake as highlighted in Fig. 1(a). Animal models can provide a framework for understanding the dynamic transport barriers nanoparticles face, but they can be highly variable and fail to provide an easily accessible platform that demonstrates how nanoparticle features impact each individual step of the transport process. Additionally, the significant cost associated with animal models can be prohibitive in parametric analysis of nanoparticle feature optimization for increased efficacy[42]. *In vitro* 3D cultures such as multicellular spheroids can provide a functional platform for studying particle penetration into avascular regions of tumors, but they do not recreate the transport boundary of extravasation and do not necessarily contain the physiologic fluid flow seen in tumors[43].

The integration of protocols developed in tissue engineering, microfluidics, and cancer biology has spurred the field of tumor engineering[44-46]. Tumor engineering is the creation of biomimetic microfluidic based scaffolds that recreate the native 3D tumor microenvironment within a highly controllable cell culture system predominantly utilizing collagen or a mixture of proteins that make up the tumor ECM[47]. These systems have primarily been utilized and developed to study key events in tumor progression such as angiogenesis and to access drug efficacy[48-50]. Conventional polydimethylsiloxane (PDMS) microfluidic platforms allow for precise control of chemical and nutrient gradients within a micro-scale system and can permit the study of cellular migration and remodeling of ECM during tumor progression[51]. Additionally, these *in vitro* systems have been designed to enable high-resolution visualization of cell events in tumor progression such as angiogenesis, tumor hypoxia, and metastasis in real-time in a non-destructive manner[52,53].

Recently, groups have begun to utilize tumor engineering to study nanoparticle transport. Ng et al have developed PDMS-Matrigel microfluidic devices to study nanoparticle penetration in a 3D matrix under varied pressure gradients and fluid flows, highlighting the importance of convective flow and showing the steric hindrance from ECM components on nanoparticle transport[54]. However, this model does not include an endothelial barrier, which is an important transport barrier that should be considered when optimizing nanoparticles to increase aggregation in the tumor. More recently, Kwak et al has developed a tumor-microenvironment-on-chip platform to simulate transport of particles and were able to show the size dependent transport of nanoparticles within a tumor microenvironment that has physiologic flow. Their platform is shown in Fig. 1(b) where lithographic techniques are used to create endothelial and lymphatic vessels with a central area containing a bulk collagen hydrogel to

study nanoparticle transport[55]. However the PDMS based platform utilized does not contain a sufficient quantity of cells to allow for FACS to determine uptake of particles by cells within the system and therefore cannot be used to draw conclusions on nanoparticle properties that affect uptake in a 3D microenvironment. Additionally, the lithography techniques used to create these platforms cannot produce a cylindrical vessel, which is important for flow profile estimation and for simplifying *in silico* modeling of transport to a 1D axisymmetric system. Finally, the need for a clean room to create these PDMS based platforms can be prohibitive for researchers.
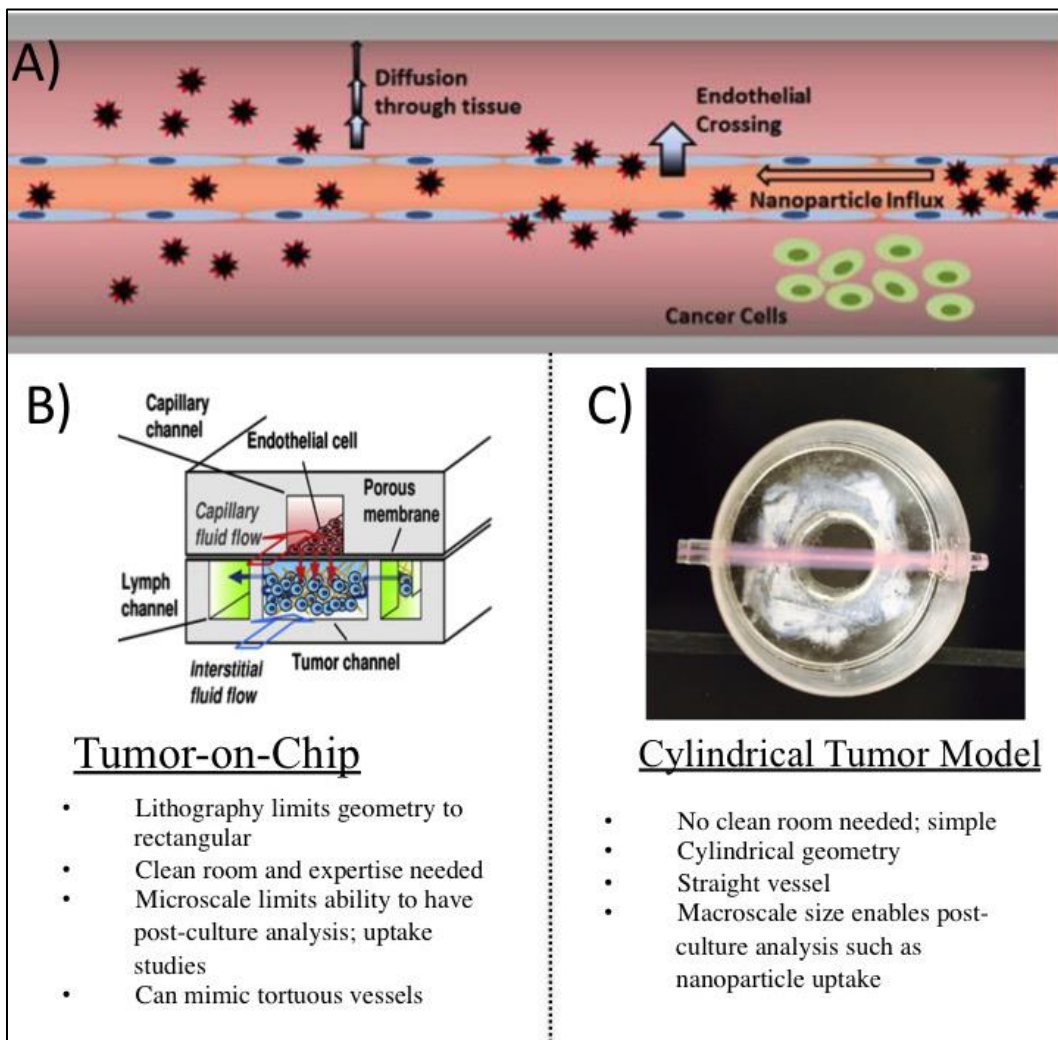
Figure1: *In vitro* modeling of the tumor microenvironment for nanoparticle transport studies. (a) Depiction of key transport barriers in the tumor microenvironment including extravasation of nanoparticles across a leaky endothelium, and diffusion in the ECM. (b) Tumor-on-chip platforms used to study nanoparticle transport and its

key features[55] (c). Image of cylindrical tumor platform described in this protocol with a central microvessel filled with fluorescent nanoparticles.

Here we present a protocol for a high throughput 3D microfluidic tumor engineered platform that recreates the tumor microenvironment through the incorporation of a cylindrical endothelialized microchannel within a collagen 3D matrix containing human cancer cells in order to study nanoparticle transport as shown in Fig. 1(c). The optically clear platform allows for high imaging resolution without the need for a clean room microlithography and the size of the platform allows for post-culture recovery and analysis. This is the first use of a cylindrical model of the tumor microenvironment containing an endothelialized microvessel to measure nanoparticle transport at the tissue and cellular level, and a comparison of this system Fig. 1(c) with tumor-on-a-chip platforms is seen in Fig. 1(b). The system can be utilized to quantify transvascular transport and transport within the ECM using particles delivered via the central microchannel. A fluorescence microscope can be used to track intensity of particle translocation from the central vessel to the collagen ECM matrix containing cancer cells over time. Lastly this system can be used to study the last step of nanoparticle transport in tumors, cellular uptake as the system enables post-culture analysis. Ultimately, novel 3D cell culture models such as the one described in this protocol should be used during development stages of nanoparticle design. The use of these models will allow for optimization of particles based on predicted *in vivo* transport barriers, and lessening of the disparity between *in vitro* and *in vivo* efficacy.

3.2. Materials

3.2.1 Construction of Tumor Platform and Endothelial Cell Preconditioning

1.MatTek 35 mm petri dish, 14 mm Microwell No. 1.0 Coverglass (Part No. P35G-1.0-14-C)

2.Fluorinated Ethylene Propylene (FEP) tubing 1/4 ID, 3/8 OD

3.Tygon 3350 Silicone 1/16 x 1/8 tubing

4. 60 ml Syringes with leur connection

5. Programmable Syringe Pump

7. 70% Ethanol

8. Female and Male luer x 1/16 in barb adapter

9. 22G 2 in and 0.5 in blunt needles

10. Pall Supor AEF Filter (bubble trap)

11. Endothelial culture media (Lonza EBM-2 with bullet kit)

12. Cancer cell culture media (DMEM with 10% FBS, 1% Pen-Strep)

12. Trypsin/EDTA

13. 500 ml Erlenmeyer flask with 3-way stopper

14. 1% polyethyleneimine (PEI) in dH_2O

15. 0.1% glutaraldehyde in dH_2O

16. 3 3 ml syringes

17. 18G Needle

18. Spatula

3.2.2 Nanoparticle Imaging and Post Culture Analysis

1. Fluorescent nanoparticles

2. Microscope with environmental chamber

3. Phosphate Buffered Saline (PBS)

4. ImageJ(NIH) or other image-processing software

5. Collagenase Type 3- Filtered (Worthington Biochemical Corporation)

6. Flow Activated Cell Sorter (FACSaria)

7. Falcon Round-Bottom Polystyrene Tubes

3.3. Methods

In this protocol described below, a cylindrical 3D *in vitro* tumor is formed that is capable of recapitulating the major transport barriers that nanoparticles face in the tumor microenvironment that are shown in Fig. 1(a). A collagen hydrogel is used to represent tumor ECM tissue and a central vessel with controlled flow represents a blood vessel within the tumor, which can be used to deliver nanoparticles representing systemic delivery. This axisymmetric platform will be utilized for imaging and uptake studies and is shown in Fig. 1(c) with nanoparticles in the center vessel.

3.3.1 Platforms and Accessory Preparation and Sterilization

1. Prepare and cut tubing for fluid flow (Tygon 3350 Silicone 1/16 x 1/8); cutting input tubing, output tubing, and bubble trap tubing as seen in Fig. 2(a). Input tubing should be cut to ~0.2 m, bubble trap ~0.05 m, and output ~0.15 m.

2. Autoclave all tubing, syringes, and needles.

3. Sterilize all valves and connectors by submerging them in 70% ethanol under ultraviolet light for 1h; allow drying overnight in sterile environment.

4. Clean petri dishes with 70% ethanol, ensuring imaging glass is clean and secure.

5. Cut FEP tubing slightly longer than petri dish (+0.5 cm) and clean FEP tubing and PDMS needle guides in 70% ethanol and UV; allow drying overnight (See Note 1).

3.3.2 Experimental System Setup

1. Plasma treat the cut FEP tubing held in a petri dish without PDMS needle guides for 4 min to enable collagen attachment to surface through surface activation.

2. Insert PDMS needle guides and use soldering iron to heat shrink FEP tubing around needle guides until firmly secure as seen in Fig. 2(b).

3. Use 3 ml syringe and 22G needle to inject 1% polyethyleneimine in dH_2O into FEP tubing capped with PDMS needle guides and incubate at 37°C for 15 min.

4. Vacuum PEI solution out of system and inject sterile 0.1% glutaraldehyde in dH_2O into FEP tubing; incubate at 37^oC for 30 min.

5. Carefully remove glutaraldehyde and wash (2x) with dH_2O, removing residual glutaraldehyde and ensuring a dry surface. The surface is now treated, has active carboxyl groups to interact with collagen, and is ready to be filled.

6. During surface treatment of FEP make sure to wipe down incubators and syringe pump with 70% ethanol.

7. Place sterile syringes, stoppers, tubing, and valves in biological safety hood.

8. Connect tubing to syringes and fill syringe with media using the tubing submerged in media, and prime syringes to remove air and visible bubbles.

9. Attach male luer barb adapter to end of media tubing as seen in Fig. 2(a)

10. Prepare collection reservoirs by attaching 3-hole stopper on Erlenmeyer flask and insert tubing into the flask. Attach a male luer barb adapter to the end of tubing, then attach 22G needle to male luer barb and place in incubator (See Note 2).

11. Secure syringes on syringe pump, maintaining the sterility of tubing and syringes while placing pump with loaded syringes into incubator. Setup the tubing and syringes in parallel as seen in Fig. 2(c) to enable higher throughput.

12. After collagen hydrogels are prepared, set syringe pump to preconditioning flow protocol shown in Fig. 2(d) and described subsequently.

3.3.3 Collagen Hydrogel Microchannel Fabrication

1. Immediately after experimental flow setup, place collagen reagents and supplies on ice.

2. Prepare a neutralizing solution based on a mixture described previously[45]. Briefly, rat tail tendons ill be dissolved in 10 mM HCl (pH 2.0) overnight at 4°C. Following centrifugation at 30,000g for 30 min, the monomerized collagen supernatant is collected and lyophilized for long-term storage. The collagen hydrogel is prepared by mixing a collagen stock solution (2x final concentration) with 10% 10x DMEM, sufficient 1N NaOH to neutralize the HCl, supplemented with DMEM containing a final concentration of $1x10^6$ MDA-MB-231 cells to bring the final solution to 5-20 mg/ml collagen. Use a spatula for an evenly mixed solution without bubbles. If co-culture with tumor cells within the matrix is desired, mix a final concentration of $1x10^6$ cells/ml cancer cells into neutralizing buffer before adding the collagen, and mix on ice. (See Note 3)

3. Add appropriate volume of collagen type I from rat-tails using syringe and 18G needle on ice. Quickly mix full solution with spatula, paying close attention to not generate bubbles in the mixture.

4. Swiftly use 1 ml syringe with 18G needle to pull up neutralized collagen and switch needle with 22G needle (See Note 4).

5. Carefully inject the neutralized collagen solution into the treated FEP tubing through the PDMS needle guide. We have previously published on the ability to select collagen polymerization parameters to result in tunable collagen hydrogels with desired pore size and stiffness. Specific collagen polymerization parameters and collagen concentrations should be chosen to best model the specific tissue properties based on work previously published by our group[56].

6. Insert 2in 22G needle into platform concentrically using the PDMS needle guides to create central void or vessel as seen in Fig. 2(d).

7. Incubate platform containing collagen and 2in 2G needle at 37°C for 20-25 min allowing the collagen to gel around the needle (See Note 5).

8. Gently remove the 22G needle, creating the central microchannel void within the collagen hydrogel.

3.3.4 Endothelial Seeding and Flow Preconditioning

A 3-day graded shear stress or flow rate protocol previously developed should be utilized in order to maintain endothelial integrity and establish a confluent monolayer of endothelial cells within the central vessel[57]. The 72 h preconditioning scheme is described below and a final flow rate that results in a wall shear stress of 1 dyne/cm^2 should be reached for a total of 6h after the 72h preconditioning in order to align endothelial cells according to previously published literature and shown in Fig. 2(e)[58]. The platform can then be used for nanoparticle flow experiments. If tumor-endothelial cell co-culture is used, we have previously shown an increase in permeability in co-culture compared to endothelial monoculture occurs due to pro-angiogenic crosstalk between endothelial and cancer cells, highlighting the systems capability to accurately model a leaky tumor microenvironment[58].

1. Start trypsinizing endothelial cells during collagen incubation according to endothelial cell protocols defined by ATCC.

2. Prepare a 20 x 10^6 cells/ml cell solution in culture medium (i.e. 400,000 cells in 20 μl) by spinning cells at 120 g for 5 min and suspending cells in an appropriate volume of cell culture medium.

3. Use 20μl pipette to inject endothelial cell solution into microchannel (20 μl).

4. Rotate complete platform 90° around central vessel axis every 30 s (4x), 1 min (4x), 2 min (8x), for a total 22 min to ensure even distribution of endothelial cells along the central vessel.

5. Carefully repeat steps 3 and 4 for a total of 2 cell solution injections to ensure complete endothelialization.

6. Attach input tubing along with an in-line bubble trap as seen in Fig. 2(e). Prime the input line with syringe pump, allowing the media to flow through bubble trap. The platforms can be placed in parallel as seen in Fig. 2(f) to allow multiple studies and high throughput.

7. Use 72 h graded increase preconditioning protocol shown in Fig. 2(e) and described previously to align and elongate endothelial cells within microvessel and to allow interactions with cancer cells within collagen matrix that leads to leaky vasculature as seen in *in vivo* tumors[44]. An example of a confluent monolayer of endothelial cells along this central vessel is seen in Fig. 2(f).

8. Collect media from reservoirs after 48 h. Use 22 μm filter to sterilize and reuse media as necessary.

9. Continue flow for 72 h followed by 6 h of increased flow with a wall shear stress of 1 dyne/cm^2 before experimentation. (See Note 6)
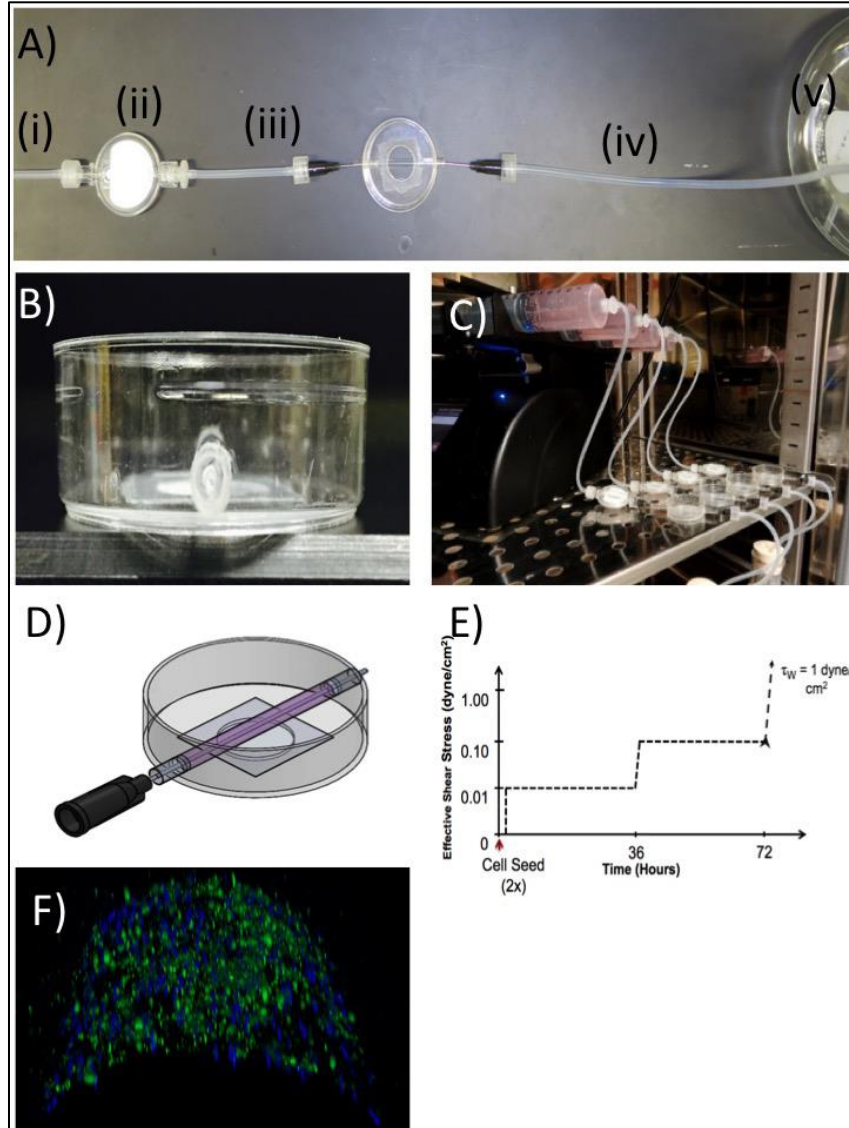
Figure 2: Protocol for forming and conditioning 3D cylindrical tumor model. (a) Flow setup with (i) input line connected to Syringe on Syringe pump (ii) bubble trap (iii) 2 in. line to connect the platform input (iv) output line connected to output of platform and (v) collection flask. (b) Side image of platform showing central hole in PDMS needle guides used to direct and hold 22G needles (c) Image of setup showing ability to have multiple platforms in-line (d) Depiction of collagen hydrogel polymerization with 22G needle in place to form central cylindrical microvessel (e) 72 h Preconditioning flow profile where flow rates are adjusted to achieve plotted wall shear stress in central vessel. (f) Fluorescent image of confluent and aligned endothelium on central microvessel after 72 h flow protocol

3.3.5 Imaging of Nanoparticle Transport

This section will describe how to dynamically and nondestructively image nanoparticle transport in the 3D tumor platform after it has undergone 78 h of endothelial preconditioning. Data from this system can be utilized to compare extravasation time constants, diffusion constants, and

51

penetration of nanoparticles into the tumor space. The data can be used to quantitatively compare transport for different nanoparticles of similar or varying properties to elucidate the effects of particle parameters on overall transport efficacy or the 1D data can be utilized easily for *in silico* models.

1. Set the microscope incubated chamber to 37°C.

2. Measure nanoparticles for desired concentration using a microbalance and resuspend in 20 mL of cell culture media (see Note 7).

3. Sonicate cell culture media containing fluorescent nanoparticles for 30 min to disassociate aggregates. (see Note 8).

4. Place the platform in microscope stage (see Note 9).

5. Add 37°C dH$_2$0 to petri dish holder as seen in Fig. 3(a), using a small amount of vacuum grease where FEP tubes meet petri dish to avoid water leakage. The water acts both as a temperature regulator and to match refractive indices of the platform to enable high-resolution imaging.

6. Place a 20 ml syringe of nanoparticle media on syringe pump. Prime the tubing and connect a 22G needle using male luer adapter and connect 22G needle at output of platform as seen in Fig. 3(a).

7. Use fluorescently tagged endothelial cells or brightfield imaging to locate endothelial vessel in the collagen hydrogel, set the focus of the microscope.

8. Take background image of vessel (make sure there are no fluorescent particles in the media).

9. Connect the input flow needle that is connected to a syringe containing nanoparticle solution on syringe pump to the input needle guide. Connect output tubing to nanoparticle waste collection and start flow

10. Capture an initial image as seen in Fig. 3(b) where nanoparticles are located completely within microvessel and the vessel is aligned in the middle of the image. Find the z-axis where vessel is at widest (center of vessel).

11. Wait 5 min and capture another image, acquiring an image every 5 min for the next 6-12 h, creating a time-lapse of the same location in the vessel keeping same image settings for each image.

12. Collect nanoparticle waste from output line.
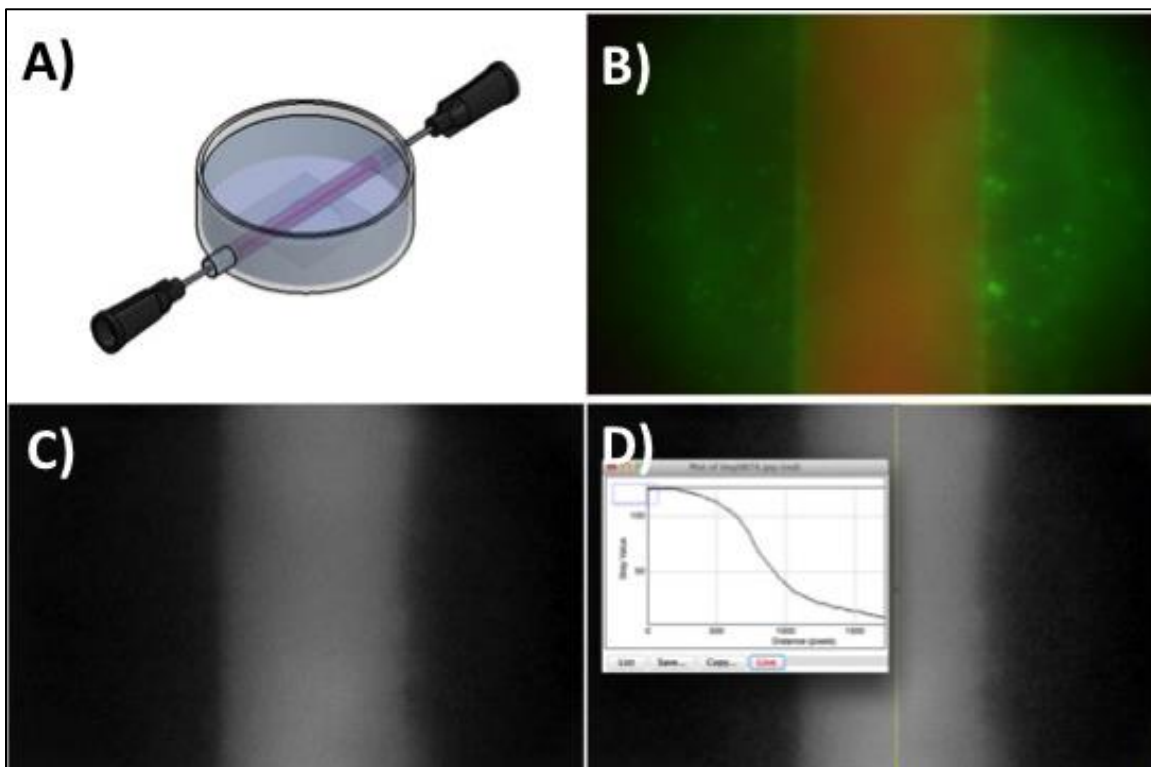
Figure 3: Nanoparticle Transport Imaging and Analysis. (a) Depiction of platform with heated water to enable high resolution imaging with steady exposed temperature with input and output needle. (b) Example image at early time point showing red nanoparticles contained within vessel and green cancer cells in the matrix. (c) Grey scale image produced for comparison showing location of nanoparticles. (d) image analysis to create radial distribution

3.3.6 Image Analysis for Nanoparticle Transport

Imaging nanoparticle transport within the system allows for understanding the dynamic process of extravasation including accumulation around the endothelial wall and diffusion into the collagen matrix over time. By performing image analysis on a time-lapse series, a better

understanding of the timing of nanoparticle transport can be accomplished. Data collected in this manner can be used to understand how these properties affect extravasation and diffusion to optimize these features to result in increased transport.

1. Take time-lapse image set for each experiment and import into ImageJ or other image processing software.

2. Separate color layers if multiple fluorescence wavelengths are used, selecting for signal corresponding to nanoparticles and transform data to grey scale as seen in Fig. 3(c) (see Note 11).

3. Find the middle of central microvessel using measuring tools.

4. Plot the average pixel intensity from the center of the vessel to the edge of image. Export the now radial data as seen in Fig. 3(d).

5. Average the left and right half of the vessel to get an average radial distribution of nanoparticles for each time point. Plot data at different time points to show translocation of particles across endothelial wall and diffusion throughout the matrix. An example of 50 nm polystyrene fluorescent particles data is shown in Fig. 4 (a-d), highlighting the value of quantitative data that could be used to refine nanoparticles to optimize their transport based on different particle properties such as size, shape, and surface charge.

In this specific case a co-culture setup Fig. 4(a) is compared to a tumor only setup Fig. 4(b) in which endothelialization of the vessel does not occur. The results seen in Fig. 4(c and d) show the importance of the barrier function of the endothelialized channel and highlight the importance of including an endothelium in an *in vitro* tumor platform through the differences in accumulation at wall and level of nanoparticle extravasation. Nanoparticle features such as size or shape can be varied and data can be displayed radially, showing axisymmetric data, to better

understand how quickly and efficiently these particles can extravasate and diffuse in the matrix of the tumor microenvironment to result in less accumulation along the wall and deeper penetration into the tumor. Computational modeling can be coupled with the data in Fig. 4 (a and b) to optimize these particles to result in higher extravasation and deeper penetration into the tumor microenvironment.
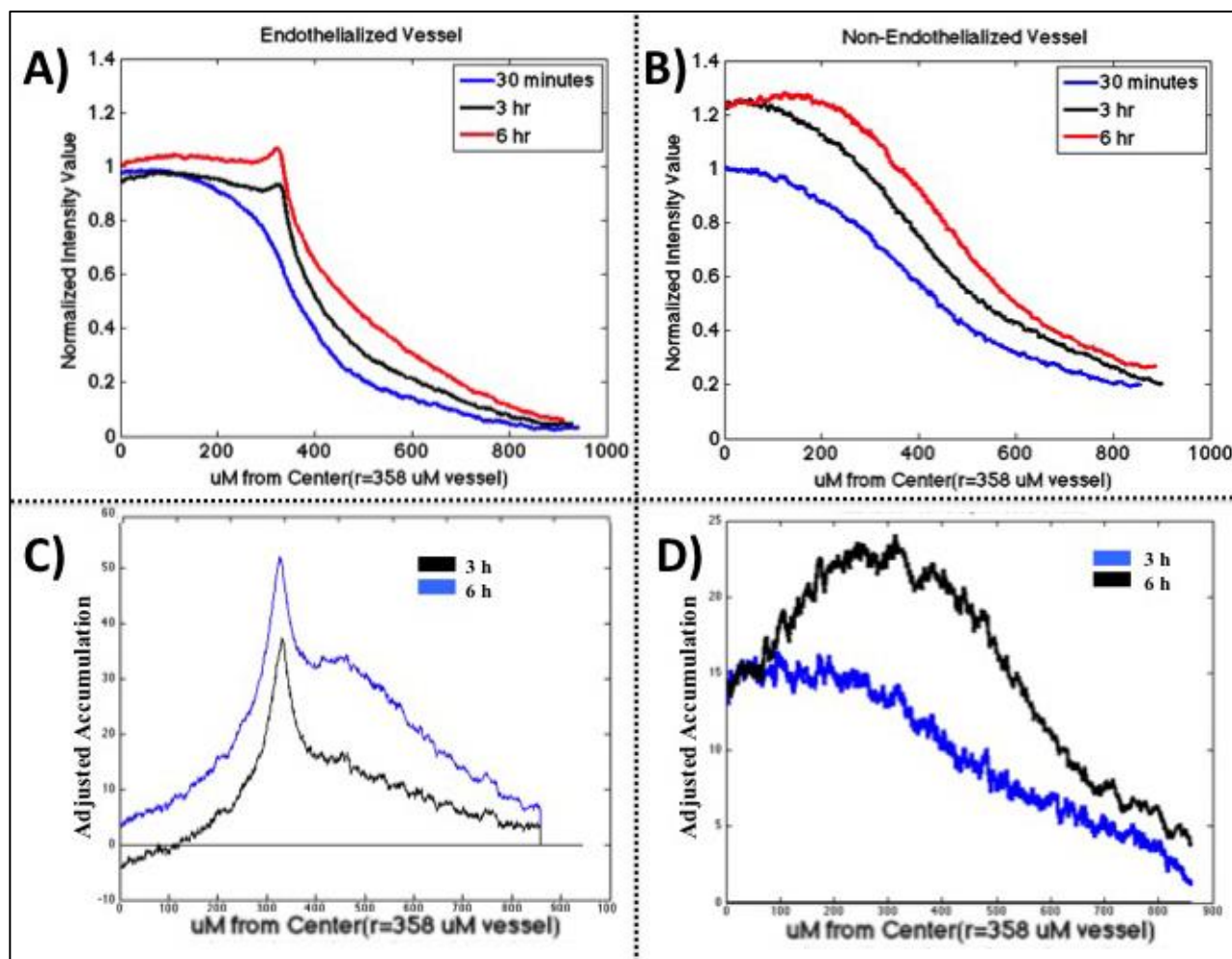
Figure 4: Example of normalized radial transport data in platform. (a) Radial distribution of relative fluorescence for 50 nm polystyrene nanoparticles in a co-culture platform at different time-points over 6 h. (b) radial data for non-endothelialized channel. (c and d) difference in intensity in 6 h and 3 h and 30 min, showing accumulation of particles near endothelial wall as the characteristic peaks seen at ~350 micron from vessel center and diffusion of particles in collagen matrix for both endothelialized and non-endothelialized platforms.

3.3.7 Nanoparticle Uptake Analysis

A nanoparticle uptake assay is described in order to show the versatility of the platform for both imaging and post-culture analysis to optimize nanoparticle transport in every stage of nanoparticle transport in the tumor microenvironment. While great strides are being made to highlight the usefulness of tumor-on-chip platforms for studying nanoparticle transport, the microscale of many of these systems limit their ability to perform post-culture analysis due to the quantity of cells required for these assays. Recovery and isolation of a sufficient quantity of cells in a macroscale platform exposed to nanoparticles allows for analysis and conclusion of nanoparticle uptake, the last step of nanoparticle transport. The protocol described below allows for post-culture analysis of nanoparticle uptake by tumor and endothelial cells in the tumor platform so that uptake studies could be coupled simultaneously with extravasation and diffusion live imaging studies to more fully understand nanoparticle transport in the tumor microenvironment.

1. After nanoparticles are flowed through the system for sufficient time (1-6 h), remove all nanoparticle media and tubing and replace with clean, sterilized tubing connected to PBS in a syringe on a syringe pump. Wash samples with perfused PBS for 1 h to wash all uninternalized nanoparticles.

2. To recover and isolate cells from the device, remove all tubing and use tweezers to remove PDMS needle guides.

3. Gently push collagen hydrogel into a cell culture well containing a collagenase solution in PBS. Incubate for 3 h for complete collagen dissolution without harm to the cells.

4. Add EDTA (5 mM) to halt collagen degradation and add fresh cell culture media. Centrifuge at 150g for 5 min.

5. Wash cell suspension 2x with ice cold PBS, centrifuging for 5 min between each wash.

6. Resuspend cells in 200 µl PBS placed on ice in a Falcon round-bottom polystyrene tube until analysis with flow cytometer.

7. Use side scattering vs. forward scattering on flow cytometer (FACSaria) to differentiate between cell debris and live cells.

8. To separate endothelial and tumor cells, endothelial (TIME-ATCC) cells were utilized that stably produce green fluorescent protein (GFP) and cancer (MDA-MB-231-ATCC) cells, which have no fluorescence signature, were used. It is only necessary to have one fluorescent cell type and for the emission of those cells to be different than the chosen nanoparticle fluorophore.

9. Uptake of red (ex/em 660/680nm) particles was assessed using FACSaria.

10. A plot of nanoparticle fluorescence as a function of cell fluorescence can then be created as seen in Fig. 5 (a-c) for 1-12 h respectively where the top two quadrants are nanoparticle positive cells and the right two quadrants are green endothelial cells.

11. Take control groups with no nanoparticle exposure for each cell type.

12. Employ gating to first separate cell type based on fluorescence (green-endothelial negative – cancer)

13.Utilizing nanoparticle negative groups and each cell types to separate based on particle uptake (y-axis).

12. Median Uptake % can be plotted as seen in Fig. 5(d) where % uptake is defined by gating determined from controls (see Note 10).

In this case the data highlights the capability of the system to show increased uptake of particles over time. Since ultimately many nanoparticles must be uptaken by cells, these experiments can impart important quantitative information on this last step of nanoparticle transport so that optimization of particle features that result in higher uptake can be

accomplished in parallel with dynamic extravasation and diffusion imaging which is nondestructive.
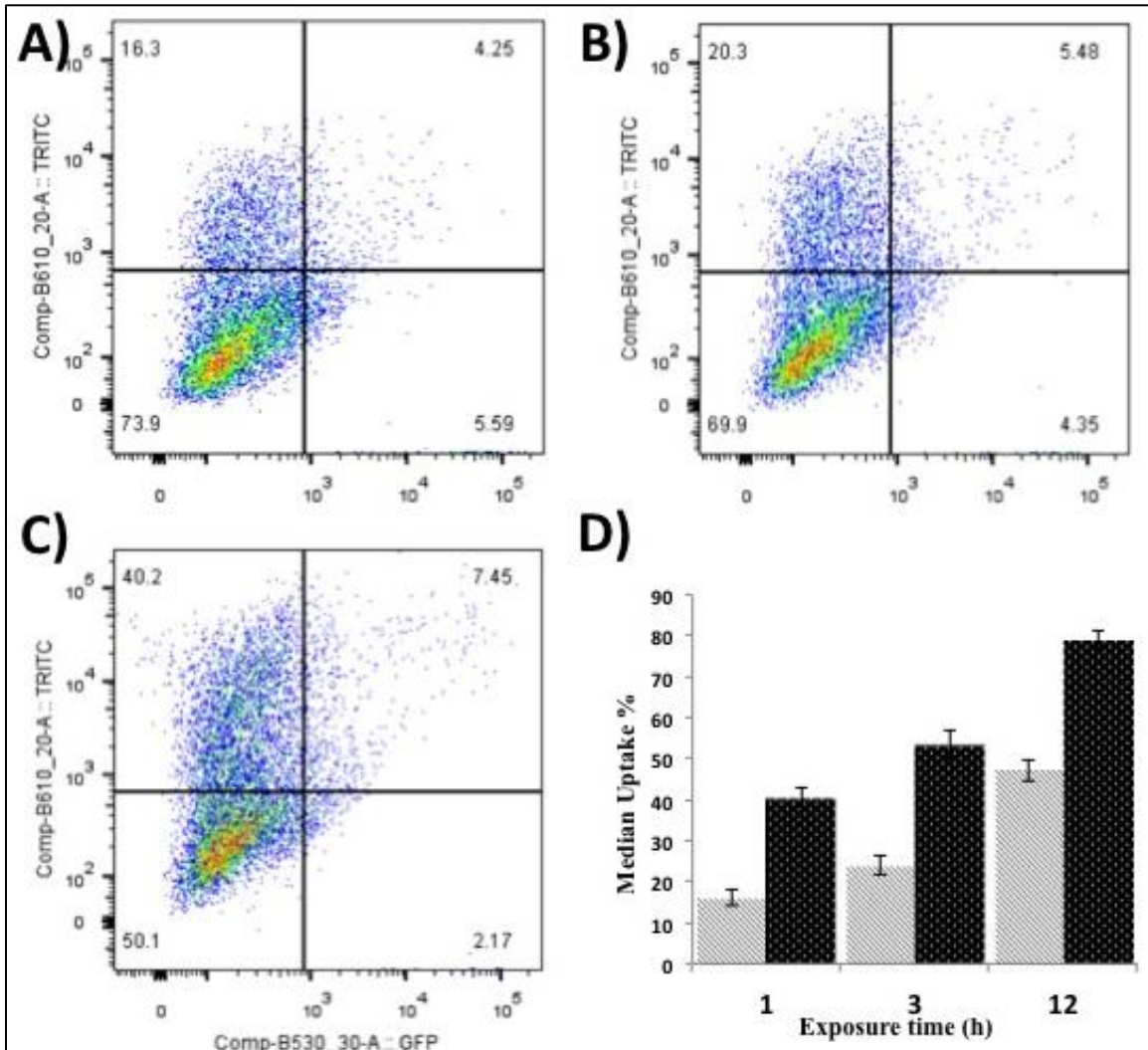
Figure 5: FACS data for nanoparticle uptake in platform. Highlighting platforms ability to get sufficient quantity of cells for post-culture analysis. (a-c) following 1, 3, 12 h exposure to nanoparticle flow in central vessel representative data showing gating employed for cell type(x-axis) and nanoparticle uptake (y-axis) (d) Uptake % of cancer and endothelial cells over the 12 h experiment, showing a statistically significant increase ($p<0.01$) in uptake over time by both cancer (grey) and endothelial cells (black).

3.4. Notes

The development of tissue engineered platforms to study key events of nanoparticle transport will ultimately lead to optimized nanoparticle treatments of cancer. In this study, a transparent microfluidic device that recapitulates many of the barriers nanoparticles face during

tumor transport including transvascular transport, diffusion and interaction with an extracellular matrix, and nanoparticle uptake. The design of the system is simple and does not require a clean room or microfabrication techniques, which makes its implementation as simple as the static 2D cell cultures that are currently used but do not recreate these tumor microenvironmental factors. Nanoparticle penetration and uptake studies show the versatility of the system and confirmed a particle size cutoff for efficient nanoparticle delivery deep into the ECM. Bioengineers can utilize this platform to study and understand nanoparticle features such as size and shape and can use the system to test the efficacy of tumor cell active targeting to result in greater uptake by cancer cells.

1) It is important that the holes in the petri dish that hold FEP tubing are as close to the size of the FEP tubing as possible to ensure a tight seal to prevent leakage with the addition of water. To make sliding of the FEP into the petri dish easier, the front end of FEP tubing can be cut at an angle. PDMS guides should be just long enough to be able to heat shrink FEP around it and hold a 22G needle during flow.

2.For collection of endothelial media previously flowed through the system the flask must be sealed. Parafilm can be used to ensure a closed system where tubing goes through stopper.

3. An appropriate collagen concentration should be chosen to result in a sturdy platform. At least a final 5 mg/ml collagen solution has been used for reproducible collagen platforms.

4. Make sure collagen completely fills FEP tubing, from one PDMS guide to the other. Any holes at the ends will result in collagen collapse and leaks.

5. Collagen Polymerization time should be kept at a minimum to ensure viability of cancer cells in the matrix

6. A final flow resulting in a shear stress of 1 dyne/cm^2 for 6 h results in a leaky co-culture setup that nanoparticles up to 200nm can extravasate[58]. Increased flow rates (10 dynes/cm^2) will result in tighter endothelial barrier and can be varied to result in changes in permeability.

7. Nanoparticle concentration for different fluorescent nanoparticles depends on the intensity of the fluorophore. Concentration of nanoparticles should be chosen to result in adequate signal to noise ratio with minimal concentration of particles and ensuring colloidal stability of particles. A sensitivity analysis should be performed to find optimized nanoparticle concentration for imaging.

8. Leave the lid off of the sonicator to reduce heat that could possibly confound results.

9. A petri dish stage can be utilized that comes with microscope. Or a plate adapter can be cut that fits to the size of a well plate with a whole cut to the size of the petri dish and needles in place as shown in Fig. 3(a).

10. Pick a wavelength for particle fluorescence in red or blue as collagen hydrogels can be highly autofluorescent in green wavelengths, which can confound results.

11. The data presented in Fig. 5 is gated so that the left two quadrants are green negative tumor cells and to the right is green positive endothelial cells. Positive and negative for cell uptake can be gated using cell populations with no particle exposure.

3.5. Acknowledgements

3.6. References:

1. Cho K, Wang X, Nie S, Chen ZG, Shin DM (2008) Therapeutic nanoparticles for drug delivery in cancer. Clin Cancer Res 14: 1310-1316.

2. Singh R, Lillard JW, Jr. (2009) Nanoparticle-based targeted drug delivery. Exp Mol Pathol 86: 215-223.

3. Stover TC, Kim YS, Lowe TL, Kester M (2008) Thermoresponsive and biodegradable linear-dendritic nanoparticles for targeted and sustained release of a pro-apoptotic drug. Biomaterials 29: 359-369.

4. Whitney J, DeWitt M, Whited BM, Carswell W, Simon A, et al. (2013) 3D viability imaging of tumor phantoms treated with single-walled carbon nanohorns and photothermal therapy. Nanotechnology 24: 275102.

5. Carpin LB, Bickford LR, Agollah G, Yu TK, Schiff R, et al. (2011) Immunoconjugated gold nanoshell-mediated photothermal ablation of trastuzumab-resistant breast cancer cells. Breast Cancer Res Treat 125: 27-34.

6. Burke A, Ding X, Singh R, Kraft RA, Levi-Polyachenko N, et al. (2009) Long-term survival following a single treatment of kidney tumors with multiwalled carbon nanotubes and near-infrared radiation. Proc Natl Acad Sci U S A 106: 12897-12902.

7. Hood RL, Carswell WF, Rodgers A, Kosoglu MA, Rylander MN, et al. (2013) Spatially controlled photothermal heating of bladder tissue through single-walled carbon nanohorns delivered with a fiberoptic microneedle device. Lasers Med Sci 28: 1143-1150.

8. Kumari A, Yadav SK, Yadav SC (2010) Biodegradable polymeric nanoparticles based drug delivery systems. Colloids Surf B Biointerfaces 75: 1-18.

9. Owens DE, 3rd, Peppas NA (2006) Opsonization, biodistribution, and pharmacokinetics of polymeric nanoparticles. Int J Pharm 307: 93-102.

10. McBain SC, Yiu HH, Dobson J (2008) Magnetic nanoparticles for gene and drug delivery. Int J Nanomedicine 3: 169-180.

11. Giustini AJ, Petryk AA, Cassim SM, Tate JA, Baker I, et al. (2010) Magnetic Nanoparticle Hyperthermia in Cancer Treatment. Nano Life 1.

12. Kennedy LC, Bickford LR, Lewinski NA, Coughlin AJ, Hu Y, et al. (2011) A new era for cancer treatment: gold-nanoparticle-mediated thermal therapies. Small 7: 169-183.

13. O'Neal DP, Hirsch LR, Halas NJ, Payne JD, West JL (2004) Photo-thermal tumor ablation in mice using near infrared-absorbing nanoparticles. Cancer Lett 209: 171-176.

14. Loo C, Lowery A, Halas N, West J, Drezek R (2005) Immunotargeted nanoshells for integrated cancer imaging and therapy. Nano Lett 5: 709-711.

15. Qin Z, Bischof JC (2012) Thermophysical and biological responses of gold nanoparticle laser heating. Chem Soc Rev 41: 1191-1217.

16. Pekkanen AM, DeWitt MR, Rylander MN (2014) Nanoparticle enhanced optical imaging and phototherapy of cancer. J Biomed Nanotechnol 10: 1677-1712.

17. Whitney JR, Sarkar S, Zhang J, Do T, Young T, et al. (2011) Single walled carbon nanohorns as photothermal cancer agents. Lasers Surg Med 43: 43-51.

18. DeWitt MR, Pekkanen AM, Robertson J, Rylander CG, Nichole Rylander M (2014) Influence of hyperthermia on efficacy and uptake of carbon nanohorn-cisplatin conjugates. J Biomech Eng 136: 021003.

19. Jain RK (1987) Transport of molecules across tumor vasculature. Cancer Metastasis Rev 6: 559-593.

20. Nagy JA, Chang SH, Shih SC, Dvorak AM, Dvorak HF (2010) Heterogeneity of the tumor vasculature. Semin Thromb Hemost 36: 321-331.

21. Maeda H, Wu J, Sawa T, Matsumura Y, Hori K (2000) Tumor vascular permeability and the EPR effect in macromolecular therapeutics: a review. J Control Release 65: 271-284.

22. Hobbs SK, Monsky WL, Yuan F, Roberts WG, Griffith L, et al. (1998) Regulation of transport pathways in tumor vessels: role of tumor type and microenvironment. Proc Natl Acad Sci U S A 95: 4607-4612.
23. Hashizume H, Baluk P, Morikawa S, McLean JW, Thurston G, et al. (2000) Openings between defective endothelial cells explain tumor vessel leakiness. Am J Pathol 156: 1363-1380.
24. Yuan F, Dellian M, Fukumura D, Leunig M, Berk DA, et al. (1995) Vascular permeability in a human tumor xenograft: molecular size dependence and cutoff size. Cancer Res 55: 3752-3756.
25. Kedem O, Katchalsky A (1958) Thermodynamic analysis of the permeability of biological membranes to non-electrolytes. Biochim Biophys Acta 27: 229-246.
26. Jain RK, Stylianopoulos T (2010) Delivering nanomedicine to solid tumors. Nat Rev Clin Oncol 7: 653-664.
27. Jain RK (1987) Transport of molecules in the tumor interstitium: a review. Cancer Res 47: 3039-3051.
28. Goel S, Duda DG, Xu L, Munn LL, Boucher Y, et al. (2011) Normalization of the vasculature for treatment of cancer and other diseases. Physiol Rev 91: 1071-1121.
29. Baxter LT, Jain RK (1991) Transport of fluid and macromolecules in tumors. III. Role of binding and metabolism. Microvasc Res 41: 5-23.
30. Baxter LT, Jain RK (1989) Transport of fluid and macromolecules in tumors. I. Role of interstitial pressure and convection. Microvasc Res 37: 77-104.
31. Flessner MF, Choi J, Credit K, Deverkadra R, Henderson K (2005) Resistance of tumor interstitial pressure to the penetration of intraperitoneally delivered antibodies into metastatic ovarian tumors. Clin Cancer Res 11: 3117-3125.
32. Netti PA, Berk DA, Swartz MA, Grodzinsky AJ, Jain RK (2000) Role of extracellular matrix assembly in interstitial transport in solid tumors. Cancer Res 60: 2497-2503.
33. Adriani G, de Tullio MD, Ferrari M, Hussain F, Pascazio G, et al. (2012) The preferential targeting of the diseased microvasculature by disk-like particles. Biomaterials 33: 5504-5513.
34. Decuzzi P, Godin B, Tanaka T, Lee SY, Chiappini C, et al. (2010) Size and shape effects in the biodistribution of intravascularly injected particles. J Control Release 141: 320-327.
35. Barua S, Mitragotri S (2014) Challenges associated with Penetration of Nanoparticles across Cell and Tissue Barriers: A Review of Current Status and Future Prospects. Nano Today 9: 223-243.
36. Bareford LM, Swaan PW (2007) Endocytic mechanisms for targeted drug delivery. Adv Drug Deliv Rev 59: 748-758.
37. Xu S, Olenyuk BZ, Okamoto CT, Hamm-Alvarez SF (2013) Targeting receptor-mediated endocytotic pathways with nanoparticles: rationale and advances. Adv Drug Deliv Rev 65: 121-138.
38. Chithrani BD, Ghazani AA, Chan WC (2006) Determining the size and shape dependence of gold nanoparticle uptake into mammalian cells. Nano Lett 6: 662-668.
39. Iversen TG, Skotland T, Sandvig K (2011) Endocytosis and intracellular transport of nanoparticles: Present knowledge and need for future studies. Nano Today 6: 176-185.
40. Lazarovits J, Chen YY, Sykes EA, Chan WC (2015) Nanoparticle-blood interactions: the implications on solid tumour targeting. Chem Commun (Camb) 51: 2756-2767.
41. Ozcelikkale A, Ghosh S, Han B (2013) Multifaceted transport characteristics of nanomedicine: needs for characterization in dynamic environment. Mol Pharm 10: 2111-2126.
42. Stirland DL, Nichols JW, Miura S, Bae YH (2013) Mind the gap: a survey of how cancer drug carriers are susceptible to the gap between research and practice. J Control Release 172: 1045-1064.

43. Gao Y, Li M, Chen B, Shen Z, Guo P, et al. (2013) Predictive models of diffusive nanoparticle transport in 3-dimensional tumor cell spheroids. AAPS J 15: 816-831.
44. Buchanan C, Rylander MN (2013) Microfluidic culture models to study the hydrodynamics of tumor progression and therapeutic response. Biotechnol Bioeng 110: 2063-2072.
45. Szot CS, Buchanan CF, Freeman JW, Rylander MN (2011) 3D in vitro bioengineered tumors based on collagen I hydrogels. Biomaterials 32: 7905-7912.
46. Griffith LG, Swartz MA (2006) Capturing complex 3D tissue physiology in vitro. Nat Rev Mol Cell Biol 7: 211-224.
47. Ghajar CM, Bissell MJ (2010) Tumor engineering: the other face of tissue engineering. Tissue Eng Part A 16: 2153-2156.
48. Cross VL, Zheng Y, Won Choi N, Verbridge SS, Sutermaster BA, et al. (2010) Dense type I collagen matrices that support cellular remodeling and microfabrication for studies of tumor angiogenesis and vasculogenesis in vitro. Biomaterials 31: 8596-8607.
49. Esch MB, King TL, Shuler ML (2011) The role of body-on-a-chip devices in drug and toxicity studies. Annu Rev Biomed Eng 13: 55-72.
50. Verbridge SS, Chandler EM, Fischbach C (2010) Tissue-engineered three-dimensional tumor models to study tumor angiogenesis. Tissue Eng Part A 16: 2147-2152.
51. Farahat WA, Wood LB, Zervantonakis IK, Schor A, Ong S, et al. (2012) Ensemble analysis of angiogenic growth in three-dimensional microfluidic cell cultures. PLoS One 7: e37333.
52. Sung KE, Yang N, Pehlke C, Keely PJ, Eliceiri KW, et al. (2011) Transition to invasion in breast cancer: a microfluidic in vitro model enables examination of spatial and temporal effects. Integr Biol (Camb) 3: 439-450.
53. DelNero P, Song YH, Fischbach C (2013) Microengineered tumor models: insights & opportunities from a physical sciences-oncology perspective. Biomed Microdevices 15: 583-593.
54. Ng CP, Pun SH (2008) A perfusable 3D cell-matrix tissue culture chamber for in situ evaluation of nanoparticle vehicle penetration and transport. Biotechnol Bioeng 99: 1490-1501.
55. Kwak B, Ozcelikkale A, Shin CS, Park K, Han B (2014) Simulation of complex transport of nanoparticles around a tumor using tumor-microenvironment-on-chip. J Control Release 194: 157-167.
56. Antoine EE, Vlachos PP, Rylander MN (2015) Tunable collagen I hydrogels for engineered physiological tissue micro-environments. PLoS One 10: e0122500.
57. Buchanan CF, Voigt EE, Szot CS, Freeman JW, Vlachos PP, et al. (2014) Three-dimensional microfluidic collagen hydrogels for investigating flow-mediated tumor-endothelial signaling and vascular organization. Tissue Eng Part C Methods 20: 64-75.
58. Buchanan CF, Verbridge SS, Vlachos PP, Rylander MN (2014) Flow shear stress regulates endothelial barrier function and expression of angiogenic factors in a 3D microfluidic tumor vascular model. Cell Adh Migr 8: 517-524.

Chapter 4: The Effect of Mild Hyperthermia on Transport of Carbon Nanohorns in an In Vitro Model of the Tumor Microenvironment

4.1 INTRODUCTION

The ability to modify the biodistribution of anti-neoplastic chemotherapeutic drugs resulting in higher drug concentration within the tumor and lower systemic toxicity is a major medical challenge that has spurred extensive research [1,2]. Classic chemotherapeutic drugs such as platinum based Cisplatin affect rapidly dividing cells, an attribute of cancer cells, in order to selectively kill tumors[3]. However, these non-targeted powerful drugs are known to cause adverse side effects including liver and kidney toxicity, leading to significant discomfort and potential morbidity [4]. Advances in nanotechnology have led to the quest to develop a "magic bullet" capable of selectively targeting cancer cells while leaving healthy cells unaffected, utilizing nanoparticles to carry a shielded drug load to the tumor [5-7]. Passive targeting of the tumor microenvironment using nanoparticles is thought to result from exploitation of the enhanced permeability and retention (EPR) effect, a hallmark of the biophysical properties of a tumor [8,-10]. The EPR effect results from a rapidly growing, pro-angiogenic tortuous vascular network in the tumor coupled with a lack of functioning lymphatics, allowing for particles less than 400nm to selectively accumulate in the targeted tumor site[11]. Additionally, novel approaches to add targeting moieties such as epidermal growth factor receptor (EGFR) and transferrin to nanoparticles can lead to active targeting approaches for nanoparticle delivery of drug payloads[12,13]. Novel nanoparticles are currently developed and investigated from a wide range of materials including polymers, gold, and carbon,

with the goal of more selective drug targeting, harnessing both intrinsic passive and active targeting schemes [10].

Thermal therapies utilize a multitude of energy sources to produce a targeted therapeutic effect for cancer therapy and can include supralethal thermal ablation where temperatures above 50°C are delivered for minutes to coagulate and destroy a tumor. Additionally, mild hyperthermia (40-45°C) can be utilized as an adjuvant to chemotherapeutic drugs as a potential method to increase the therapeutic efficacy. Although studies have shown that the integration of these two modalities can result in enhanced efficacy of the delivered drug, the field of mild hyperthermia has stalled after a period of optimism and high clinical use in the 1980s[14]. A variety of clinical methods to deliver therapeutic hyperthermia for a synergistic effect have been studied including whole body or regional water bath, heated organ perfusion or heated blood perfusion, and regional heating through ultrasonic radiation or microwave applicators[16-18]. Although these modalities of heat delivery are effective in their ability to sufficiently heat tissue, they are not selective in nature and can result in healthy tissue damage or systemic toxicity and are often not optimized which can deliver inadequate heating and create the impression that the combination is not effective for cancer treatment [17,19]. While the therapeutic translation of this modality has encountered a fair share of boundaries, there is still much promise for hyperthermia as a potent sensitizer for chemotherapy.

In addition to potential applications in diagnostics, and gene and drug delivery, nanoparticles have great promise for enhanced delivery of therapeutic hyperthermia as highlighted in Figure 1a. By harnessing the same passive and active targeting techniques in drug delivery, tuned nanoparticles have the potential to create spatially confined heating in the tumor

when activated by an external energy source, reducing nonspecific tissue damage[20,21]. Plasmonic nanoparticles such as gold nanorods or nanospheres can convert high tissue-depth-penetrating near-infrared light (NIR) into heat through production of surface plasmon resonance to ablate a tumor [22-24]. Similarly, carbon nanomaterials have been shown to produce ablative thermal temperatures due to their high absorbance to coupled NIR light [25,26]. Single Walled Carbon Nanohorns (SWNHs) are dahlia shaped aggregates of single walled carbon cones with average diameters of 150-200 nm [45,46]. Their high carbon content makes them excellent photo-absorbers in the NIR range, which enables their use as photothermal agents for the thermal destruction of tumors[47,48]. Additionally their high surface area to volume ratio makes them outstanding drug delivery candidates, which is highlighted in Figure 1a [49]. Most published photothermal studies have been focused on delivering sufficient heat to destroy a tumor [27]. However, there are many potential shortcomings that include limited heating due to heat sink effects near blood vessels and incomplete heating throughout the tumor and insufficient nanoparticle concentrations resulting from EPR effect heterogeneity. In combination, SWNHs can be an excellent candidate for the co-delivery of mild hyperthermia and chemotherapeutic drugs and there might be great promise in utilizing these particles for the selective delivery of mild hyperthermia for a synergistic effect with a drug payload where the boundary to deliver sublethal temperatures is more easily overcome.

As previously described, mild hyperthermia has classically been viewed as a form of adjuvant therapy to increase the efficacy of chemotherapeutic drugs with the two major hypotheses for synergism including; increased diffusion of the drug into the tumor and cells and increased DNA lesions as a result of heating, on which the drugs can act[15]. However, with the development of co-delivery nanoparticles, thermal exposure should be considered to augment not

only drug efficacy but also particle transport. Groups have looked at co-delivery of mild hyperthermia and chemotherapeutics in photothermal-chemotherapy studies where particles are utilized to enhance chemotherapeutic efficacy, however they often neglect the role of hyperthermia on particle transport [28-30]. Mild hyperthermia has previously been shown to increase tumor blood flow and tumor microvascular pore size, which affects the transvascular transport of nanoparticles into the tumor [31]. The effects of mild hyperthermia on the permeability of tumor vessels for a wide variety of sizes has been studied and have highlighted the role heat plays on not only synergistic drug efficacy, but mass transport of particles[32]. More recent studies have looked at how reversible and repeatable this application is, determining the thermotolerance of the endothelial cells to secondary heating and its effect on particle vascular transport[34]. More recently, groups are beginning to study how particles coupled with heating can affect extracellular matrix-nanoparticle interactions that determine nanoparticle penetration into tumors [34]. Despite the breadth of research into utilizing nanoparticles to co-deliver mild hyperthermia and a drug payload for increased drug efficacy, less is known about how mild hyperthermia affects the transport of these particles in the tumor.
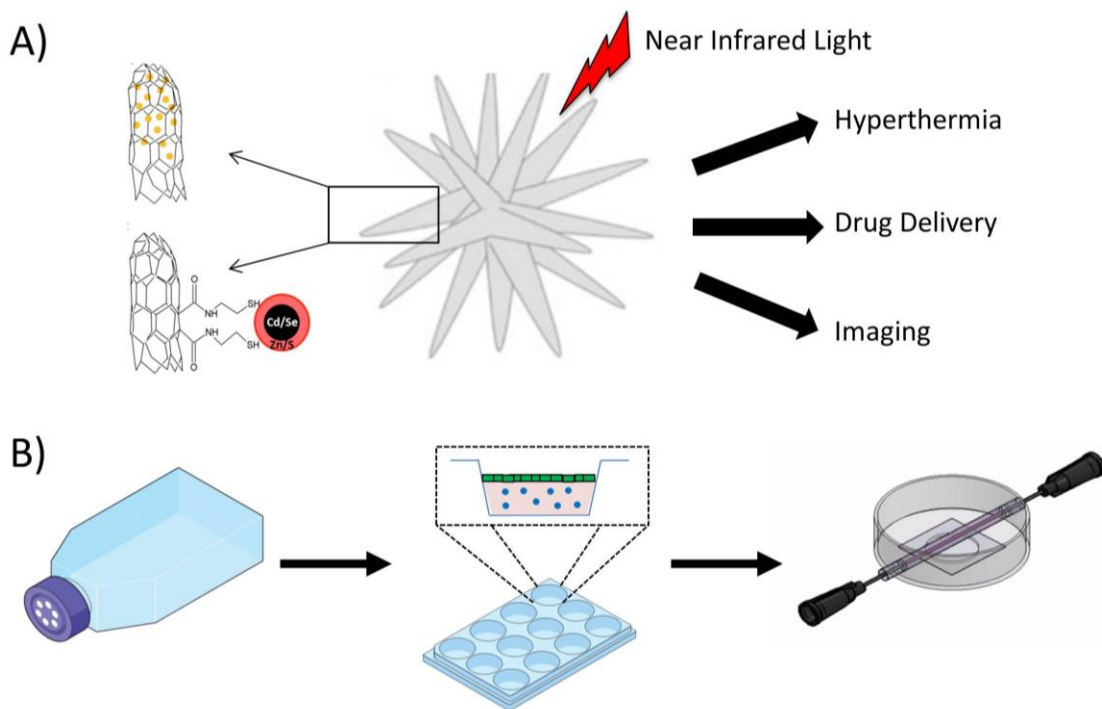
Figure 1: Multimodal Nanoparticle Development and *In Vitro* Testing Models. Depiction of SWNHs **(A)** and our ability to add the QDs(left-lower) allowing for high imaging resolution and neoplastic drugs to the internal structure and surface for drug delivery(left -upper). When the carbon particle is coupled with NIR light heating results for either thermal destruction or thermal enhancement(right). **(B)** Depiction of *in vitro* tumor models ranging from overly simple 2D cell culture (left) to 3D static tumor hydrogels (middle) and more advanced 3D dynamic cylindrical models utilized in the study with a central endothelialized vessel from which SWNHs undergo transport barriers of extravasation, diffusion, and cellular uptake

Transport processes that can be enhanced by mild hyperthermia are often unaccounted for in traditional two dimensional, static cell culture protocols commonly utilized during the particle design and optimization stages. Therefore, a possible explanation for the disparity between *in vitro* efficacy and *in vivo* translation of these novel nanoparticle thermal enhancement schemes can be explained by the models systems in which they are tested and optimized and their shortcomings [35]. Frequently, efficacy of these co-delivery protocols are tested in a flat, static environment where particles are directly exposed to tumor cells in a solution. This setup can overstate drug synergism and effects of perturbation on nanoparticle uptake, while additionally not accounting for changes in nanoparticle transport at the tissue level [36]. Animal models are

useful for providing a macroscopic evaluation for the effect of mild hyperthermia on nanoparticle transport in tumors as previously shown in studies of liposomes, albumin, and other macroscopic materials[32]. In these xenografic models, groups were able to show an increase in liposomal permeability from tumor capillaries as a function of applied temperature[37]. However, animal models can lack the ability to elucidate microscopic changes in permeability and often do not allow for precise control of temperature and particle distribution and often only serve as efficacy evaluators and not parameter refiners [38]. Furthermore animal models can be complicated with many uncontrollable variables that may prevent isolation of a single stimulus effect such as mild hyperthermia on transport while additionally being cost prohibitive in early design stages and difficult to analyze with high resolution.

A novel field of tissue engineering, termed tumor engineering, aims to use techniques developed in cancer biology, microfluidics, and tissue engineering to create *in vitro* biomimetic three dimensional (3D) platforms that more closely mimic the tumor microenvironment. These model systems have shown promise as an intermediate between *in vitro* and *in vivo* studies in the past decade [39-41]. Tumor engineered platforms generally consist of cancer cells seeded within bio-polymeric scaffolds, allowing cell-matrix interaction and can be created with inclusion of physiologic fluid flows through the introduction of microfluidic channels, representative of tumor vasculature [42]. Many of these platforms have been carefully designed to elucidate key events in tumor progression and have been utilized to study angiogenesis, tumor normalization, and therapeutic response[43]. In addition to studying tumor biology, groups are beginning to use these models to evaluate transport of nanoparticles within the tumor microenvironment. Ng et al have recently developed a microfluidic platform that highlights the importance of interstitial fluid flow on nanoparticle penetration within tumors, a variable that cannot be mimicked in a 2D

culture system [44]. With the introduction of complex and controllable 3D *in vitro* models it is now possible to study how adjuvants such as mild hyperthermia or other tumor vasculature perturbation methods affect nanoparticle transport in a highly repeatable and precisely controllable manner to optimize next generation therapies. We have previously developed multiple three dimensional models of the tumor microenvironment including a collagen disk model and a cylindrical collagen hydrogel matrix with embedded cancer cells in the matrix that contains a central endothelialized microchannel subjected to physiological flows as seen in Figure 1b and described subsequently[39]. This model has shown to recreate key events of cancer progression such as angiogenesis, and vascular organization, in a simple cost effective manner that does not require the use of a clean room.

In this study we explore the effects of mild hyperthermia (42°C) on the tissue and cellular level transport of SWNHs to highlight the potential mechanism of synergy between heat and nanoparticle drug delivery and how tumor engineering can be utilized to optimize novel therapies. After characterizing the particles we demonstrate, in a high throughput perfused 3D microfluidic platform of the tumor microenvironment, that mild hyperthermia affects the vascular permeability of 200 nm SWNHs in the tumor vasculature. Additionally we highlight how this increase in permeability results in a higher concentration of particles beyond the vasculature into the tumor space only in a tumor-vascular co-culture setup, highlighting the potential of a selective tumor transport enhancement mitigating drug delivery to off target tissue. Finally we show that mild hyperthermia has no significant effect on SWNH uptake in a 3D environment for a breast cancer cell line. When these particles are utilized as co-delivery vehicles for hyperthermia and drugs, careful optimization must occur to result in increased transport at the tissue level and increased drug efficacy at the cellular level. This feat can be

engineering through methods such as thermally responsive materials that can selectively release a drug payload in the tumor interstitial space, taking advantage of the multi-scale transport processes resulting in increased particle transport at the tumor tissue level and drug synergy from therapeutic mild hyperthermia at the cell level.

4.2 Methods

Nanoparticle Synthesis

While SWNHs are used extensively for both drug delivery and photothermal heat generation, their carbon composition makes tracking of mass transport challenging especially in a 3D matrix. We therefore modified the SWNHs with a fluorescent beacon in order to track nanoparticles in our *in vitro* tumor model. Quantum dot (QD) decorated SWNHs were prepared through a carbodiiamide reaction as described previously by our group [50]. Briefly; after oxidation of SWNHs through exposure of 8M HNO_3 under reflux for 24 h at 100°C and reprotonation through exposure of 1M HCL overnight at 110°C as described previously created oxidized SWNHs (SWNH-OX). 0.1 M 1-ethyl-3-(3-dimethylaminopropyl carbodiimide) (Sigma Aldrich, EDC) was then added to the 0.1 mg/ml SWHN-OX solution in water for and vigorously stirred for 5 minutes. N-Hydroxysufosuccimide sodium salt (Sulfo-NHS, Sigma Aldrich) was then added at a concentration of 5 mM and gently stirred for 5 min. An AET ligand was then added at a concentration of 2 M. After adjustment of solution pH to between 5-6, the solution was stirred for 16 h and filtered with a 0.1 μm PVDF membrane (Millipore) and suspended at a concentration of 0.1 mg/ml in water. 630 nm CdSe/ZnS QD (Ocean Nanotech) suspended in chloroform was then mixed with the SWNH-AET at a 3:1 w/w QD/SWNH ratio and allowed to attach for 24 h and subsequently filtered and dried over nitrogen. Dried SWNH-QD were stored until needed at which time they were sonicated in a 0.5 mg/ml DPSE-PEG aqueous solution to

enhance dispersibility and reduce aggregation. An overall depiction of this attachment chemistry is shown in Figure 3A. Solutions of SWNH-QD were diluted for transport studies.

Nanoparticle Characterization

Transmission electron microscopy (TEM) grids were prepared by introducing SWNH-QD, QDs, or SWNHs diluted in dH_2O to Lacey Carbon Mesh grids (Electron Microscopy Sciences). Grids were then dried with 100% EtOH and imaging was executed on a JEOL 2100 TEM at a central facility. Dynamic light scattering (DLS) and zeta potential measurements were performed on a Malvern Zetasizer Nano ZS utilizing Malvern Zetasizer Software v 7.03. Measurements were performed with a 4 mW He-Ne laser at a 633nm wavelength with a scattering angle of 173. Measurements were acquired in triplicate at 37°C after suspension of nanoparticles in dH_2O at a concentration of 0.1 mg/mL following sonication for 1h.

Cell Culture

A human breast carcinoma cell line MDA-MB-231(ATCC) breast carcinoma and a telomerase-immortalized human microvascular endothelial (TIME-ATCC) cell line were used in this study. A lentiviral vector system was used to genetically modify MDA-MB-231 and TIME to stably produce either a green fluorescent protein (GFP) or a red fluorescent protein (RFP) respectively for real time imaging studies. Stable fluorescent TIME cells were a generous gift from Dr. Shay Soker at the Wake Forest Institute for Regenerative Medicine (Winston-Salem, NC).

MDA-MB-231 cells were cultured in Dulbecco's Modified Eagle's medium, nutrient mixture F-12 (DMEM/F12)(Sigma Aldrich) supplemented with 1% penicillin-streptomycin (P/S) (Invitrogen) and 10 % fetal bovine serum (FBS), all according to information provided from ATCC. MCF7 cells were cultured in DMEM media supplement with 10% FBS and 1% P/S.

TIME cells were cultured in EBM-2 endothelial growth media supplemented with a growth factor BulletKit (Lonza CC-4176). All cell cultures utilized in this study were maintained in a 5% CO_2 atmosphere at 37°C in an incubator.

Microfluidic Platform

3D microfluidic co-culture models of the tumor microenvironment utilized to study mass transport of SWNH-QDs were fabricated as described previously [40]. Type I collagen was prepared by dissolving excised rat tail tendons in a pH 2.0 HCl solution overnight at 4°C and then centrifuged at 30,000 G for 30 min. After collection of the collagen containing supernatant, the collagen solution was frozen overnight and subsequently lyophilized for long term storage. The collagen was then suspended at 16 mg/ml in HCL as a working stock solution for use in the platform. A final concentration of 8 mg/ml collagen was neutralized for use in the model as it was previously shown to recreate an elastic modulus that is similar to neoplastic tissue, and can support cellular remodeling while providing a sturdy framework for maintaining the integrity of the microfluidic system with the presence of flow in the channel [51].
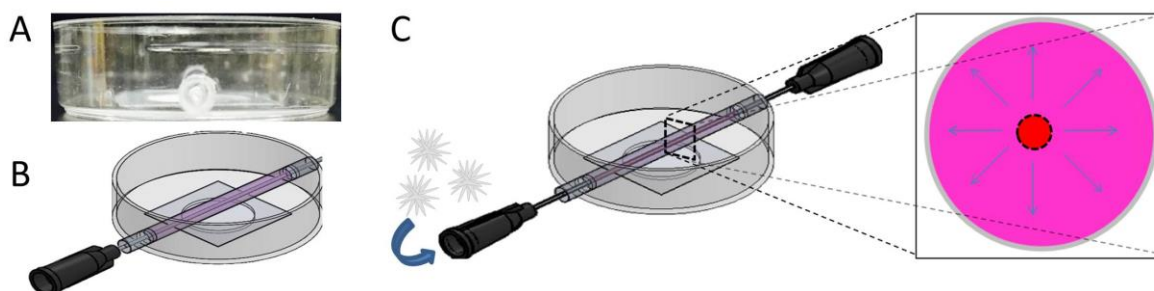
Figure 2: Three Dimensional Perfusable Platform for Studying Nanoparticle Transport (a) Side view of petri dish holding FEP tubing with central vessel PDMS guide **(b)** Polymerization of collagen hydrogel in FEP with 2" 22G needle used to create central void **(c)** Depiction of model with input and output needles connected to syringe pump containing SWNHs and output to media collection. Transport can be measured radially around the central vessel delivering SWNHs

An 8 mg/ml collagen solution was created by diluting stock solution with 10% final volume 10x DMEM, and sufficient NaOH resulting in a pH between 7.0-7.4, and cell culture medium containing a final concentration of $2x10^6$ MDA-MB-231 cells per ml. The hydrogel

73

solution was then added into a fluorinated ethylene propylene (FEP) tubing capped with 2 central needle guides created with poly-dimethylsiloxane (PDMS) as shown in Figure 2A. Prior to collagen addition, the FEP surface was functionalized to promote collagen attachment, reducing collagen collapse over the duration of experiments. After sterilization with ultraviolet light for 1 h and 70% ethanol for 1 h, the FEP tubing was exposed to air plasma for 5 min to activate hydroxyl groups on the FEP inner surface. The FEP was then treated with 1% polyethyleneimine in dH_2O for 15 min followed by 0.1% glutaraldehyde solution for 20 min to create carboxyl groups for collagen interaction. The collagen hydrogel was allowed to crosslink for 30 minutes at 37°C with a 2 in 22 gauge needle placed in the platform as shown in Figure 2B. The needle was then carefully removed after polymerization, creating a centralized cylindrical microchannel with a diameter equal to the diameter of the needle (711 μm) and containing cancer cells suspended within the bulk of the collagen hydrogel. TIME cells were added to the central microchannel at a concentration of 20 x 10^6 cells/ml and rotated 90° every minute for 15 minutes to encourage complete coverage of the microvessel wall.

Cell culture media flow was introduced into the microchannel via the attachment of 22 gauge stainless needles partially into the PDMS needle guides as shown in Figure 4A. The input needles of multiple platforms were then connected to media containing syringes on a syringe pump via sterilized Tygon silicone tubing with an in-line bubble trap. An output line is connected to a closed erlenmeyer flask which can be subsequently filtered and reused. A 3-day graded shear stress or flow rate protocol previously developed was utilized in order to maintain endothelial integrity and establish a confluent monolayer. After the 72 h preconditioning scheme, a rate of 1 dyne/cm^2 was reached for a total of 6 h to align endothelial cells according to previously published literature. The platform could then be used for nanoparticle transport

experiments where particles were introduced into one side of the model through the vessel, where it could then radially diffuse through the tumor after transvascular transport as demonstrated in Figure 2C.

Nanoparticle uptake

2D cell culture uptake studies were utilized as previously described in [49]. MDA-MB-231 cells were seeded in six-well tissue culture treated polystyrene dishes at a concentration of approximately $5x10^6$ cells/well. Cells were incubated for 36 hours to result in a confluency greater than 50%. SWNH-QDs were exposed to cells in a serum free DMEM solution at a concentration of 0.01 mg/ml for 60 minutes at either 37°C or 42°C. Cells were then washed with cold PBS (4x) and centrifuged at 120G for 5 minutes. Cells were then suspended and kept on ice until they were analyzed with a BD Biosciences FACSAria cell sorter (San Jose, CA).

A hanging well insert was used in the nanoparticle uptake studies to negate the role flow has on transvascular transport and focus only on the role of hyperthermia in cellular uptake in a 3D system. Following similar collagen gelation protocols as the microfluidic model, 4 $x10^6$ MDA-MB-231 cells were mixed in neutralizing collagen and 200 µL were dispensed in each hanging well, having a final height of 1.67 mm to minimize effects of heating on diffusion as seen in Figure 3G. TIME endothelial cells were either added on top of an approximately 200 µm acellular collagen region after 24h of cancer cell culture at a density of 3x104 cells/ cm2. The transwell culture setup allows for endothelial media to be exposed on the endothelial cells and cancer cell medium on the tumor platform. The model system was cultured for 72h, replacing media every 24h, to allow for cell interactions and endothelialization as previously described by Szot et al[51].

Serum free endothelial media was mixed with 0.05 mg/ml SWNH-QDs and exposed to collagen hydrogels for 1 hour. After exposure, the gels were rinsed 4x with cold PBS to halt endocytosis and remove nanoparticles from the extracellular space. The hydrogels were then gently dissociated with collagenase (Sigma Aldrich) for 3h in order to keep cells intact for FACS analysis. After digestion, the cells were transferred to centrifuge tubes and centrifuged at 150x g for 5 min at 4°C. Supernatant was aspirated and 200 µL of fresh media was added and suspensions were kept on ice until analysis. Forward and side scattering was utilized to rule out nanoparticles and cellular debris. 1.5×10^5 cells were then counted for each sample and a mean uptake percentage determine from gating and a median fluorescence was calculated for each sample for comparison between groups. If multiple cell types were used, green fluorescence was utilized to distinguish TIME cells from MDA-MB-231.

Permeability Assay

A quantitative permeability assay was utilized to compare the permeability of the central microvessel to the SWNH-QD as a function of applied temperature according to previous studies [52]. The approximately 200 nm diameter SWNH-QD were suspended in serum free cell culture medium at 0.05 mg/ml to minimize aggregation with significant signal to noise ratio. The SWNH solution was perfused at a wall shear stress of 0.1 dyn/cm^2 (26 µl/min) for 1 h. Images were captured every 5 min after 30 min to allow for the affects of hyperthermia to manifest. An inverted fluorescent microscope (Zeiss Axiovert 20) was utilized to visualize nanoparticle permeability. Heating was applied by adding heated water from a water bath set to either 37°C or 42°C to the platform petri dish, with vacuum grease employed to reduce leaking at FEP/ petri dish junction. Temperature was set and monitored utilizing an incubated stage (Zeiss stage). ImageJ (NIH) was utilized to analyze an average fluorescent intensity in a region of interest

76

(ROI) that spanned the width of the platform with the microchannel in the middle as seen in Figure 4A and B. An effective permeability coefficient was calculated in this region as previously described utilizing the following equation.

$$P_d = \frac{1}{I_1 - I_b}\left(\frac{I_2 - I_1}{\Delta t}\right)\frac{d}{4}$$

where I_b is the background intensity, I_1 is the first time point average intensity in the ROI, I_2 is the average intensity after Δt (5 minutes) and d is the internal diameter (711 µm). 3 time points were used to determine the coefficient and averaged. An n=4 was used for each temperature.

A second permeability and diffusion assay was utilized where average intensity after 3 h of nanoparticle containing media flow was calculated $100\,\mu$ m from the vessel wall. An inverted fluorescent microscope (Zeiss Axiovert 20) was utilized to measure the radial distribution of nanoparticle fluorescence after 1 h of either 37°C or 42°C exposure and 2 h of additional nanoparticle flow at 37°C. A total time period of 3 h was chosen to allow for sufficient signal to noise $100\,\mu$ m from the vessel wall. However, 3 h of heating cannot be utilized as this amount of heat would result in significant damage to the endothelial wall and would not represent transient changes in the permeability. Three platform setups were utilized in these studies to help determine the effect of hyperthermia on transvascular transport in healthy vs pathological tissue and the effect on transvascular transport vs diffusion. A tumor endothelial co-culture was used similar to the first permeability studies, an endothelial mono-culture with no cancer cells in the collagen matrix was used to represent non-disease state tissue, and lastly a tumor monoculture was used with no active endothelial wall on the central vessel to study the effects on diffusion in the ECM.

4.3 RESULTS

Nanoparticle modification and characterization

The attachment of the fluorescent beacon QDs to the outside of the SWNHs occurred as expected in order to visualize the transport of the carbon particle, based on methods described previously [50]. After acid oxidation of pristine SWNHs through nitric acid and hydrochloric acid reflux, the particle underwent a carbodiiamide bond to functionalize the surface with an AET ligand. QDs were then added and attached through an interaction with the AET ligand. TEM images shown in Figure 3C indicate the presence of QDs on the surface of the SWNHs, which is confirmed by the clear lattice structure of the QDs located on the SWNHs. STEM images also reflect the approximately 200 nm size of these particles and the lack of severe aggregation. STEM performed shows a SWNH-QD on the carbon lacy mesh in Figure 3D. Elemental analysis shows the presence of oxygen, cadmium, and carbon in Figure 3 E-G respectively. An overlay of these elements is shown in Figure 3H, showing the oxidation of SWNHs and even distribution of QDs(Cadmium) throughout the carbon particles. DLS of the conjugates compared to pristine SWNHS in Figure 3B confirm the increase in size through the attachment of QDs as the peak of the curve shifts to the right and a lack of peak around the QD size shows complete stable attachment with no free QD in solution. These sizes average diameter of SWNHs increased from 110 ± 3.7 nm to 203± 16.5 nm for the SWNH-QD. Some slight aggregation was observed with SWNH-QD which is likely only small (<4) particle clusters of nanoparticles and does not represent large-scale aggregation. The zeta potential, which is used to signify colloidal stability when a potential of magnitude great than 30 mV is measured, was found to be -32± 0.68mv for SWNH-QDs and -51 ± 1.8 for SWNHs which confirms stability of the particles in solution.

Nanoparticle Uptake

Cells that were directly exposed to 0.01mg/ml SWNH-QD for 1 hour at either 37C or 42 C were first measured to determine quantitatively the amount of nanoparticles uptaken and the influence of hyperthermia on cellular uptake to determine if values corresponded with a decrease in uptake at mild hyperthermia in bladder cells as previously published [49]. Figure 4a shows a representative image set of MDA-MB-231 after exposure to SWNH-QD at 37C (top) and 42 C (bottom). Qualitatively, little difference can be confirmed from the bright field imaging, however localization within the cell and around the nucleus confirm uptake as opposed to surface attachment. A FACs analysis was then employed to provide valuable quantitative data where fluorescence was measured at 660nm and cell count and fluorescent signal was measured as shown in Figure 4b. The uptake percentage of SWNH-QD by MDA-MB-231 in a 2D cell culture system fell from 81.5 ±4.5% to 68.2 ±5.6% when exposure at 37C was compared to 42C, mirroring results from previously published bladder cancer cell lines and is shown in Figure 4E (2D). Additionally, the median signal intensity was reduced in the 42C exposed group with an median of 725 ± 172 compared to 1151 ± 150 when exposed at 37 degrees as summarized in Figure 4F (2D).
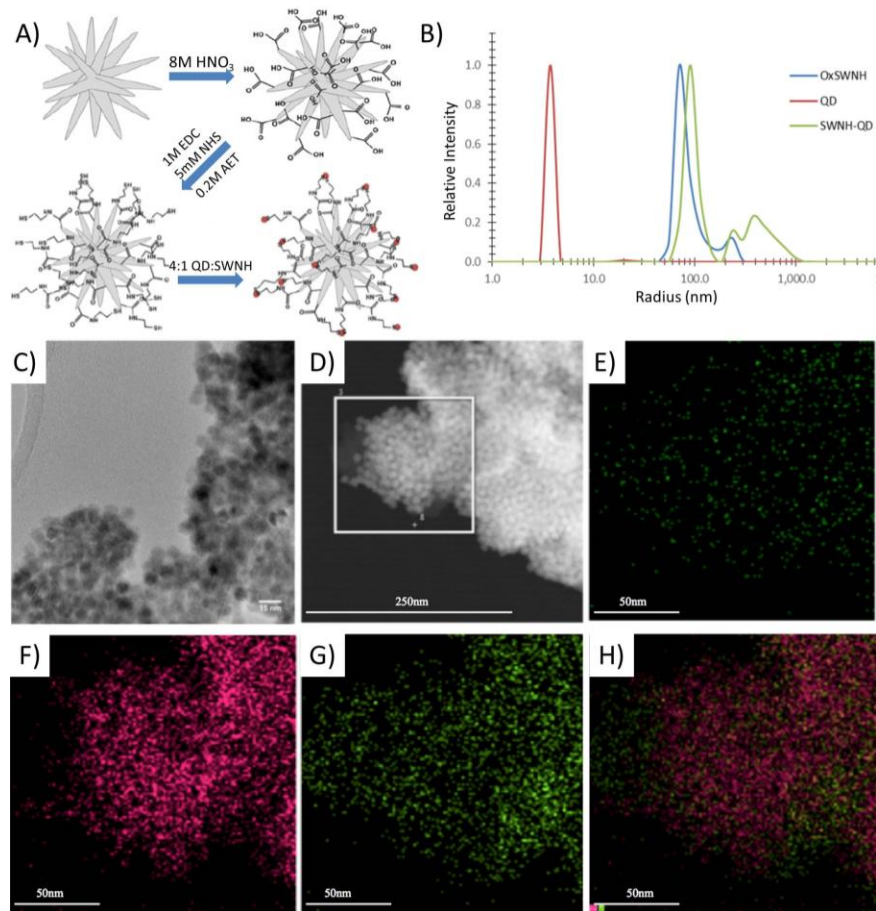
Figure 3: Characterization of SWNH-QD for visualizing nanoparticle transport. (a) Depiction of carbodiimide chemistry technique to attach fluorescent QDs to surface of SWNH cones **(b)** DLS of SWNHs, QDs, and SWNH-QDs showing increase in size of SWNH-QD and lack of QD peak **(c)** TEM image showing attachment of QD to SWNH **(D)** STEM of SWNH-QD for elemental analysis **(E-G)** colorimetric representation for oxygen, cadmium, and carbon respectively. **(H)** Overlay of elements showing even distribution of QD on SWNHs

A static 3D model of the tumor microenvironment then utilized to determine the effects of mild hyperthermia on uptake of SWNHs in a 3D environment where particles were not in direct exposure to cells cultured on a plate where transport barriers to nanoparticle diffusion are not recreated. A 12-well hanging well insert was utilized as depicted in Figure 4G where 4×10^6 MDA-MB-231 cells were suspended within a collagen matrix with either the presence or absence of an endothelial monolayer. 1 h exposure of SWNH-QD at either 37 or 42°C was accomplished and calcein life imaging shown in Figure 4H demonstrates an intact tumor and high viability of well dispersed MDA-MB-231 cells. After 3 h of mild digestion of the matrix

with collagenase, cells were analyzed with FACS as shown in Figure 4 C,D for monoculture and co-culture respectively. MDA-MB-231 showed no significance in either uptake percentage, 70.7 ± 2.1 vs 66.4 ± 4.2 % (37 vs 42°C), determined through gating nor average intensity of each cell, 1465 ± 182 vs 1104 ± 124.8 (37 vs 42°C), as shown in Figure 4 E and F (3D MC). However, when a 3D co-culture system was utilized, a significant increase in percentage of MDA-MB-231 positive for uptake of SWNH-QD was seen for 42C vs 37C (58.7 ± 2.3 % vs 39.3 ± 1.7 %) as seen in Figure 4 E (3D CC). Additionally, the median signal intensity increased from 848 ± 120 at 37°C to 1186 ± 147 at 42°C as shown in Figure 4F(3D CC). The difference in uptake is further demonstrated qualitatively in Figure 4I where 5000 MDA-MB-231, digested from a monoculture setup, show a QD fluorescent distribution profile with a characteristic right peak demonstrating high uptake of particles where x-axis is fluorescence signal. When a co-culture is utilized (37 CC) there are now two peaks due to an active endothelial layer acting as a barrier to nanoparticle transport lowering uptake by a larger percentage of the cells. When 42°C is exposed to the same co-culture setup, the peak shifts back to the right which indicates greater uptake by the MDA-MB-231. Overall this could signify a potential disruption of endothelial barrier which allows a greater concentration of particles to the cancer cells.
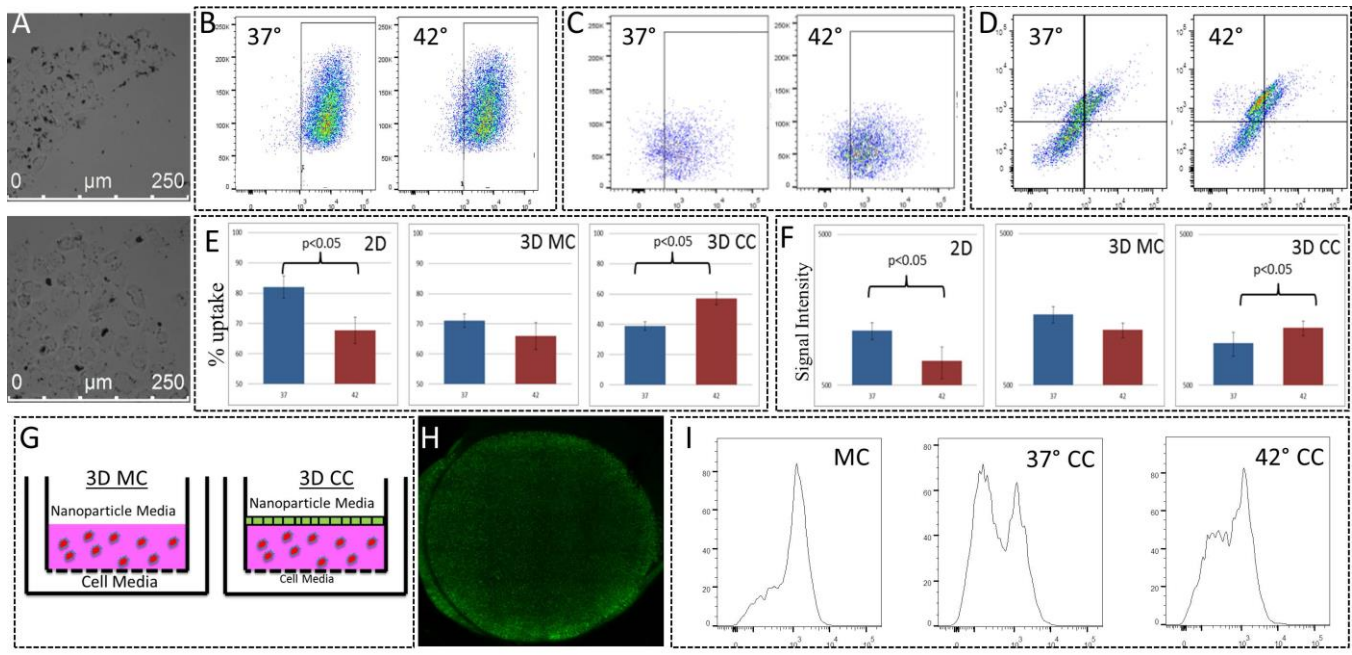
Figure 4 Effect of hyperthermia on SWNH Uptake in Multiple Models (A) Brightfield image of MDA-MB-231 cancer cells in 2D cell culture with uptake of SWNHs (black) at 37°C (top) and 42°C bottom **(B)** Representative data from FACS analysis used to determine nanoparticle uptake of 2D cell culture. **(C)** Representative data from FACS analysis used to determine nanoparticle uptake in 3D monoculture. **(D)** Representative data from FACS analysis used to determine nanoparticle uptake in 3D co-culture with gating employed to distinguish cell type **(E)** SWNH uptake percentage for each model setup (2D, 3D MC, 3D CC) **(F)** SWNH signal intensity for each model setup (2D , 3D MC, 3D CC). **(G)** Schematic of setup with cancer cells dispersed within a 3D collagen matrix in a hanging well in monoculture (3D MC) and with endothelial layer co-culture(3D CC). **(H)** Viability of cancer cells in 3D matrix after exposure to SWNHs and 42°C. **(I)** Distribution plots of 3D MC and 3D CC at 37 and 42 °C to highlight relative distribution of SWNH uptake

Microfluidic Platform

A 3D microfluidic model of the tumor microenvironment previously developed by our group was successfully produced to study nanoparticle transport and the effect of mild hyperthermia on nanoparticle transport. A platform containing a collagen hydrogel with a central microvessel is shown in Figure 5B. EBM-2 endothelial growth media was utilized to pre-conditional the tumor platform as shown in Figure 5A through the system using a graded increase preconditioning protocol as previously described [42]. TIME cells that stably produce red fluorescent protein (RFP) are shown in Figure 5B, 24h after injection showing homogenous coverage (top), but not complete confluence and with areas of cell aggregation or clumps. Figure 5 B (middle rows) show endothelial confluence after 48h and 72h respectively, highlighting the

82

importance of the graded shear stress protocol in creating a confluent endothelium aligned in the direction of flow within the vessel. Figure 5B (bottom row) depicts a complete co-culture model after 72 h preconditioning, showing viable green cancer cells evenly distributed throughout the collagen tumor model and an intact red endothelium ready to study nanoparticle extravasation, diffusion in collagen, and cellular uptake. Figure 5 C demonstrates an F-actin stained endothelial monolayer when no cancer cells are present and 5D is a representative image of the same setup with cancer cells evenly distributed within the collagen matrix. No quantifiable differences can be seen in the overall confluency or direction of the cells indicating that any differences between the models are microscopic and likely due to changes in cell-cell interactions.
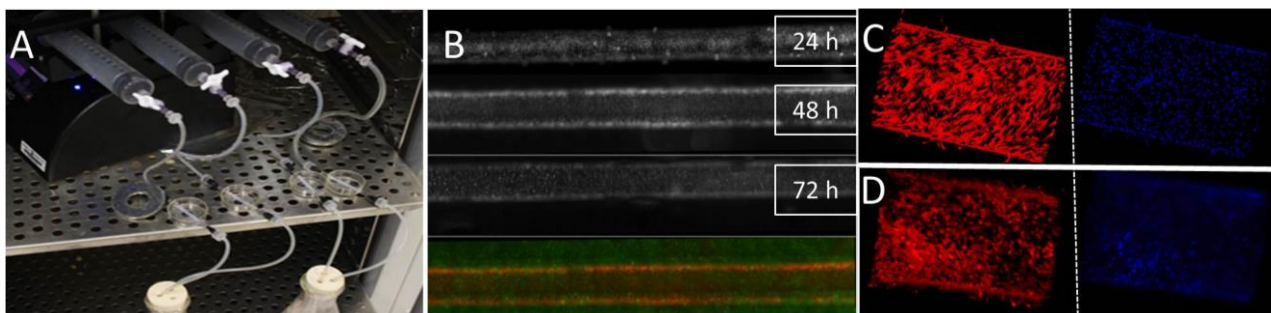
Figure 5: 3D Microfluidic Tumor Model (a) preconditioning setup with multiple models in parallel using single syringe pump. **(b)** evolution of endothelial confluency over 72h preconditioning and overall co-culture setup with green cancer cells in matrix **(C-D)** F-Actin and DAPI staining for endothelial monoculture and co-culture respectively

Permeability Assay

The co-culture microfluidic model was first utilized to determine the permeability coefficient of SWNH-QDs as a function of applied temperature in a tumor-endothelial co-culture setup. After the 72h preconditioning and 6 h of a wall shear stress of 1 dyn/cm^2 to align the cells, a water bath was used to warm water to either 37°C or 42°C and the platform was filled with heated water as shown in Figure 6(C). The water served two purposes, to heat the platform to the desired temperature, acting as a thermoregulator, and to match the refractive indices of the materials as previously described to enable high resolution imaging deep into the collagen [40].

Temperature was maintained utilizing an incubated stage for 1 h and was monitored using multiple thermocouples to ensure steady temperature. Surface temperature of the platform after 10 min exposure in the incubator is shown with and without water in Figures 6 E and F respectively. Uniform, steady temperature within the platform is evident in the water filled platform whereas significant (±1.5°C) temperature gradients are seen in the platform in contact with air and temperature could not be maintained with the open system. The measured effective permeability coefficient, P_d, of the endothelialized microchannel as a function of temperature indicates that the P_d of SWNH-QD significantly increases during mild hyperthermia (42°C) to 44.62± 8.83 $\mu m*10^2$/s compared to 29.14± 5.2 $\mu m*10^2$/s at 37°C for 1h. The Pd was calculated according to methods described by Chen et al where the average intensity of the fluorescent signal is calculated in a region of interest, shown in dashed lines in Figures 6 A and B with the endothelialized microvessel in the middle. Images were taken every 5 minutes for 30 min during heating. The P_d was found to be statistically significantly different between the two groups (α <0.05), showing higher permeability of SWNH-QD at 42°C compared to 37°C in our tumor platform model (Figure 6D).
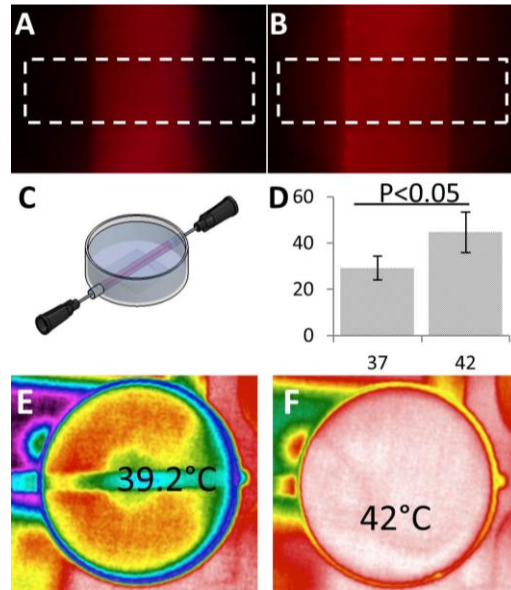
Figure 6: Permeability coefficient calculation for SWNHs in Microfluidic Platform. Pd was calculated by taking a region of interest (white box) with central microvessel over 1h and solved with Eq. 1. **(A)** Representative image of SWNH permeability at 37°C for 1 h **(B)** Representative image at 42°C for 1h. **(C)** Platform Setup for Pd calculation of SWNH with heated water for temperature control and imaging (d) Increased Pd for co-culture setup at 42°C compared to 37°C *P<0.05. The difference in temperature profile for platform without the use of insulating water **(E)** and with the inclusion of water **(F)** as measured by thermal camera.

Nanoparticle transport in Microfluidic Platform

Figure 7A shows a high resolution image of the co-culture platform with a red endothelial wall surrounded by green cancer cells and Figure 7B is an example of a volumetric projection of nanoparticles (red) extravasating from a central microchannel into the collagen matrix containing green MDA-MB-231 cancer cells. Particles were perfused in the system at the same rate as the permeability assay and a radial plot of intensity value from the center of the vessel was created as shown in Figure 7A overlaid on image. It has previously been shown that 100 μm is the expected diffusion length from the tumor microvasculature for nanoparticles between 100-300 nm in diameter and successful delivery to the tumor for effective treatment requires sufficient nanoparticle transport to this distance. In order for direct comparison between samples this distance was chosen to compare average intensity values of particles flown through the system.

In the first setup an endothelial monoculture was considered to represent a healthy vessel, as it has previously been shown to be less leaky than a tumor-endothelial co-culture setup[42]. The results are shown in Figure 7c where the average intensity value 100 μm from the vessel for 42°C is 64.1 ± 5.1 and 60.7± 4.4 for the 37°C sample. The values for the tumor co-culture are expressed in Figure 7c with values of 90.1±6.7 and 75±5.8 for 42°C and 37°C respectively, a statistically significant difference (α <0.05). Figure 7 d&e demonstrate an F-actin and DAPI stain for 42C mono-culture (D) and 42C co-culture (E) which show no significant change in DAPI distribution, signifying no loss in cell density, however there is marked disruption of the endothelial cytoskeleton shown by the F-Actin staining in Figure 7 E which seemingly demonstrates the effect of mild hyperthermia is more pronounced in the co-culture setup.   The last experiment for a tumor monoculture with no endothelial cells lining the central vessel was performed in order to determine the effect of hyperthermia on diffusion in the absence of an active endothelial barrier. The values for these cases are additionally shown in Figure7c where the average intensity is 121.2± 8.9 for 42°C and 126.7±7.8 for 37°C. The findings from these results show that hyperthermia affects nanoparticle transport only in the co-culture system highlighting the promise for heat-enhanced transport localized to the tumor microenvironment.
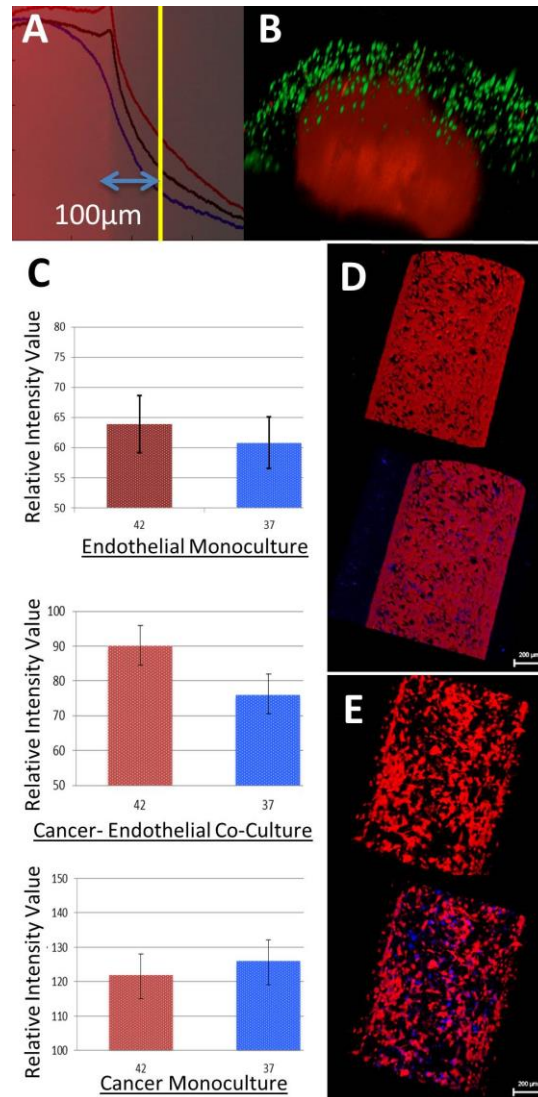
Figure 7: Use of microfluidic model to determine effect of hyperthermia on SWNH transport.(A) High resolution image of co-culture setup with depiction of comparison setup where radial profile of fluorescence intensity is plotted and a value is calculated at 100 μm distance from vessel wall **(B)** Representative 3D projection of SWNHs (Red) extravasating past endothelium into the collagen matrix containing green MDA-MB-231 cells **(C)** Values for endothelial mono-culture showing no significant change in transport between 42°C and 37°C (top), tumor-endothelial co-culture with significant change in transport between temperatures (middle), tumor monoculture showing no significant difference (bottom). The mean and SE are shown for an n=4. F-actin and DAPI staining for 42°C monoculture **(D)** and 42°C co-culture **(E)** exposure highlighting cytoskeletal changes with co-culture hyperthermia with no change in overall cell distribution

4.4 Discussion

The field of nanomedicine is focused on harnessing the unique features of nanoparticles such as infrared absorptive properties for photothermal applications, drug and fluorophore loading capabilities, and properties of the tumor including the EPR effect for passive targeting of

particles[53-55]. Overall, the goal of nanoparticle enhanced therapies is to limit nonspecific damage to healthy tissue while destroying the tumor. Hauck et al recently used gold nanorods to enhance uptake of Cisplatin, but did not explore the effects of hyperthermia on cell uptake of nanoparticles [36]. If particles are used to deliver both heath and drug, the final uptake of the particles can be important and the resulting changes in transport throughout the tumor. However, many of these novel therapies are often tested in overly simplistic two dimensional cell culture models which can neglect many features of nanoparticle transport in the tumor microenvironment such as extravasation, and diffusion limitations in a dense ECM while overstating effects on nanoparticle uptake. In order to better optimize these novel nanotherapeutic approaches for the enhancement of chemotherapeutics, a better fundamental understanding of how hyperthermia affects these different transport barriers particles face in the tumor is imperative.

Recently, groups have begun to utilize tumor engineered platforms developed based on cancer biology, microfluidics, and tissue engineering to create *in vitro* 3D tumors to study nanoparticle transport, in order to overcome the limitations of 2D cell culture [44,58]. PDMS microfluidic platforms have been used to study the effect of particle size on mass transport of particles in the tumor microenvironment[59]. Raeesi et al have recently utilized a tumor platform to show how photothermal destruction of collagen by gold nanorods results in deeper tumor penetration [60]. However, temperatures chosen were used to increase diffusivity of particles through ECM destruction and not for photothermal enhancement through mild hyperthermia augmentation of mass transport and drug efficacy. In this study we present a cost efficient, high imaging resolution platform that can be created without the need for a clean room that is capable of measuring nanoparticle transport at the tissue and cellular level to test the influence of the

microenvironment on nanoparticle transport and demonstrate how under different model conditions the effect of hyperthermia can even be reversed as seen in SWNH uptake by cancer cells in 2D vs 3D co-culture. A model that is able to recapitulate the tumor microenvironment and the dynamic transport barriers that mild hyperthermia can positively enhance during photothermal-chemotherapy treatments while enabling dynamic high resolution probing of the spatiotemporal nanoparticle transport will allow for nanoparticle refinement and optimization, ultimately leading to better treatments.

In this study we utilized SWNHs as our model nanoparticle to test in our 3D in vitro system. SWNHs stand out as a promising nanoparticle for multimodal photothermal chemotherapy treatments due to their highly controllable heat generation under NIR excitation, significant drug loading capability, and lack of inherent toxicity [45,47]. However, implications of this work go far beyond just SWNHs as many other types of nanoparticles can be utilized for these therapies such as gold nanoparticles which are currently investigated for their ability to enhance chemotherapeutic drugs through mild hyperthermia [56,57]. We were able efficiently tag our nanoparticles with a stable fluorescent signal that is capable of high signal to noise ratio. The effectiveness of this protocol is demonstrated in Figure 3 where we were able to attach the QDs to SWNHs, confirmed by multiple characterization techniques. Ultimately the ability to visualize these particles using a fluorescent signal allows for quantitative data obtained by both imaging and FACs.

We first utilized a static 3D tumor model to elucidate the effect of mild hyperthermia on the last mass transport stage in the tumor microenvironment, cellular uptake. The purpose of this work was to both show one mechanism for mild hyperthermia to augment cancer-nanoparticle efficacy and to demonstrate how when used incorrectly, a 2D cell culture system can overstate

these effects. Our first 3D model is based on a previous hydrogel platform developed in our lab that replicates many tumor features[62]. The results from the breast cancer cell line uptake indicate that mild hyperthermia has no effect on cellular uptake of SWNHs in a 3D tumor model when the cancer cells are evenly distributed with an ECM containing hydrogel. These results contradict previous results published with 2D cell culture in which uptake of SWNHs is minimized during mild hyperthermia and additionally do not correspond with 2D cell culture uptake studies demonstrated in this study with MDA-MB-231 break cancer cells[49]. This suggests that 2D cell culture might over exaggerate the effects of mild hyperthermia on cellular uptake of nanoparticles as the cells are in direct contact with the nanoparticle c containing fluid and are more likely to have cytoskeleton dysregulation on a 2D platform where lifting can occur. When a 3D co-culture setup is utilized where a confluent monolayer of endothelial cells acts as a barrier to nanoparticle transport into a bulk matrix containing cancer cells, we demonstrate an increase in uptake in SWNHs by the MDA-MB-231 cancer cells, which was not seen in the case of the cancer monoculture which had insignificant differences between different thermal groups. Overall the data shown in Figure 4 E & F highlight the utility of *in vitro* tumor engineered platforms for studying nanoparticle transport, especially cellular uptake where 2D platforms fail to represent the complex processes that mild hyperthermia can augment such as an endothelial barrier that can disrupted, leading to greater delivery.

Mild hyperthermia has previously been shown *in vivo* to increase the delivery of nanotherapeutics such as liposomes and antibodies through the already hyperpermeable tumor microvasculature [32]. While the exact mechanism of this effect is not completely elucidated, based upon previous knowledge that large vessel pores exist exclusively in the tumor microvascular network, it can be hypothesized that an increased delivery of particles in response

90

to hyperthermia results from pore size argumentation. Morphological changes in the endothelial cytoskeleton can cause shrinking of cells and therefore increased extravasation. Additional hypotheses for mild hyperthermia effects on nanoparticle extravasation include tumor blow flow modulation, increased intravascular pressure and decreased intratumoral pressure, however these parameters are impossible to test in 3D platform[61]. Results from our permeability study highlighted in Figure 6 confirm that mild hyperthermia results in an increase in extravasation or permeability to SWNH-QDs in the tumor co-culture platform as demonstrated by a statistically significant increase in permeability coefficient presented in Figure 6D. Heated water and environmental temperature were utilized rather than photothermal heating to ensure homogenous heating throughout the platform as shown in the difference in temperature distribution in Figure 6 E&F. However, the particles could be coupled with an NIR source to produce heat as previously shown in our group [46]. These results additionally show the value in a controllable model of the tumor microenvironment. Since blood flow and fluid pressure cannot change in the *in vitro* system, this result helps confirm the hypothesis that mild hyperthermia induces endothelial changes resulting in increased pore sizes and extravasation.

Transvascular transport, or extravasation of nanoparticles represents only the first transport process in the tumor microenvironment that must occur to affect the targeted tumor cells. While hyperthermia has previously been shown to affect extravasation of nanoparticles *in vivo*, a controllable system to highlight how hyperthermia affects transport deep into the tumor is additionally important. Previous research has demonstrated that delivery of particles into a tumor 100 μm past the vasculature into the tumor is needed for treatment. In Figure 7 we investigate the effect of mild hyperthermia on SWNH penetration 100 μm past the vessel wall in three platform setups. There was only a significant increase in nanoparticle transport in the co-culture

setup shown in Figure 7C. To elucidate the effect of hyperthermia on just particle diffusion in the ECM, a third setup was used with no endothelial wall and no significant difference was seen between 37° and 42°C. We have previously shown that co-culture tumor platform results in hyper-permeability as a result of angiogenic signaling. High resolution confocal staining of not only transport of the particle but additionally the marked difference in cytoskeleton arrangement of endothelial cells in a co-culture experimental setup exposed to 42°C without a decrease in DAPI coverage seems to demonstrate that this temporary cell change results in the pore formation through cell shrinkage, thus allowing more nanoparticles to flow into the tumor. These results suggest that mild hyperthermia results in transvascular pore size increase in the tumor microenvironment that is already more permeable, and therefore could be harnessed to result in specific delivery of nanoparticles selectively to the tumor due to the limited effect of mild hyperthermia on an intact vasculature in healthy tissue. Overall, these results suggest that mild hyperthermia has a primary tissue level adjuvant effect in nanoparticle treatments by affecting vessel permeability and this affect can be tuned to be selective to the tumor microenvironment.

Although the 3D perfusable *in vitro* tumor model described in this study and highlighted in Figures 2 and 4 is a simplistic recreation of the tumor microenvironment, we have previously shown how this model mimics many features of the tumor environment including angiogenesis, hypoxia, and hypermeability[39,40]. It can therefore be hypothesized that *in vitro* tumor platforms such as the one presented will respond to external stimuli such as hyperthermia similarly to an *in vivo* response, permitting this system to be utilized as a cost efficient, reproducible tool for optimizing a number of nanoparticle based treatments early in the development stage, prior to the use of expensive *in vivo* models. Additionally, as highlighted by our permeability study, the simplistic nature of our platform allows for precise control of

microenvironmental cues that are not possible in a highly complex *in vivo* study, allowing for elucidation of stimuli effects that can confirm *in vivo* postulations. While small animal tumor models including flank models will continue to be gold standards for studying nanoparticle mediated tumor treatments, these studies should be performed simultaneously with 3D *in vitro* systems to help control failures from animal to human translation, leading to higher efficacy treatments.

En masse, the results of this study suggest that optimization of future nanoparticle enhanced thermo-chemotherapy treatments can occur through increased mass transport from the tumor vasculature. Using mild hyperthermia for increased tumor targeting has several other benefits. Similar temperatures have been used to trigger drug release from thermoregulated polymeric nanoparticles, making it possible to deliver drugs selectively[63]. Additionally, unstudied in this experiment, mild hyperthermia can result in synergy with chemotherapeutic drugs resulting in superaddative cytotoxic effects. Examining these drug dependent cell efficacy effects with other tumor models could expand the results of this study to formulate schemes in which both nanoparticle transport and drug efficacy are optimized. Ultimately, determining the optimum timing and temperature to result in increased extravasation, diffusion, and efficacy of carried chemotherapeutic drugs through multiscale thermal enhancement will leady to novel, high efficacy nanoparticle based phothermally enhanced treatments. Future studies will involve the addition of drugs to the nanoparticles to understand not only the transport of the particles, but the resulting efficacy of treatment in these multimodal therapies and other adjuvants to nanoparticle cancer therapies.

4.5 Conclusion

In an environment where continuously evolving nanomedicines for cancer treatment are facing increased skepticism due to perceived lack of *in vivo* translation, novel tumor model systems must be developed and employed to optimize nanomedicine based on measurable data in a system that recreates biophysical properties of the tumor more so than traditional cell culture. Here we have demonstrated that tumor engineering models can be utilized to study the transport of SWNHs within the tumor microenvironment. Two tissue engineered models, a cylindrical model with the introduction of convective flow and a static flow disk model were developed and validated to understand the effect of hyperthermia on nanoparticle transport which is crucial when developing novel photothermal enhancement therapies. A more comprehensive and controlled understanding of the transport of SWNHs at the tumor tissue level and the effects of mild hyperthermia on key transport boundaries in the tumor microenvironment such as extravasation, diffusion within the matrix, and cellular uptake will enable optimization of such dual nanoparticle-heat delivery vehicles to result in greater efficacy in treatment prior to the use of costly animal models. Additionally these "simple-yet-complex" model systems can provide valuable data for optimization of wide variety of nanoparticle mediated cancer therapies.

4.6 References:

1. Lowenthal RM, Eaton K (1996) Toxicity of chemotherapy. Hematol Oncol Clin North Am 10: 967-990.
2. Minchinton AI, Tannock IF (2006) Drug penetration in solid tumours. Nat Rev Cancer 6: 583-592.
3. Larsen AK, Escargueil AE, Skladanowski A (2000) Resistance mechanisms associated with altered intracellular distribution of anticancer agents. Pharmacol Ther 85: 217-229.
4. Schimmel KJM, Richel DJ, van den Brink RBA, Guchelaar HJ (2004) Cardiotoxicity of cytotoxic drugs. Cancer Treatment Reviews 30: 181-191.
5. Cho K, Wang X, Nie S, Chen ZG, Shin DM (2008) Therapeutic nanoparticles for drug delivery in cancer. Clin Cancer Res 14: 1310-1316.
6. Farokhzad OC, Langer R (2006) Nanomedicine: developing smarter therapeutic and diagnostic modalities. Adv Drug Deliv Rev 58: 1456-1459.
7. Peppas NA (2004) Intelligent therapeutics: biomimetic systems and nanotechnology in drug delivery. Adv Drug Deliv Rev 56: 1529-1531.

8. Maeda H (2001) The enhanced permeability and retention (EPR) effect in tumor vasculature: the key role of tumor-selective macromolecular drug targeting. Adv Enzyme Regul 41: 189-207.

9. Yuan F, Dellian M, Fukumura D, Leunig M, Berk DA, et al. (1995) Vascular permeability in a human tumor xenograft: molecular size dependence and cutoff size. Cancer Res 55: 3752-3756.

10. Maeda H, Nakamura H, Fang J (2013) The EPR effect for macromolecular drug delivery to solid tumors: Improvement of tumor uptake, lowering of systemic toxicity, and distinct tumor imaging in vivo. Adv Drug Deliv Rev 65: 71-79.

11. Hashizume H, Baluk P, Morikawa S, McLean JW, Thurston G, et al. (2000) Openings between defective endothelial cells explain tumor vessel leakiness. Am J Pathol 156: 1363-1380.

12. Qian ZM, Li H, Sun H, Ho K (2002) Targeted drug delivery via the transferrin receptor-mediated endocytosis pathway. Pharmacol Rev 54: 561-587.

13. El-Sayed IH, Huang X, El-Sayed MA (2006) Selective laser photo-thermal therapy of epithelial carcinoma using anti-EGFR antibody conjugated gold nanoparticles. Cancer Lett 239: 129-135.

14. Ohno S, Siddik ZH, Kido Y, Zwelling LA, Bull JM (1994) Thermal enhancement of drug uptake and DNA adducts as a possible mechanism for the effect of sequencing hyperthermia on cisplatin-induced cytotoxicity in L1210 cells. Cancer Chemother Pharmacol 34: 302-306.

15. Alvarez-Berrios MP, Castillo A, Mendez J, Soto O, Rinaldi C, et al. (2013) Hyperthermic potentiation of cisplatin by magnetic nanoparticle heaters is correlated with an increase in cell membrane fluidity. Int J Nanomedicine 8: 1003-1013.

16. Gofrit ON, Shapiro A, Pode D, Sidi A, Nativ O, et al. (2004) Combined local bladder hyperthermia and intravesical chemotherapy for the treatment of high-grade superficial bladder cancer. Urology 63: 466-471.

17. Wust P, Hildebrandt B, Sreenivasa G, Rau B, Gellermann J, et al. (2002) Hyperthermia in combined treatment of cancer. Lancet Oncol 3: 487-497.

18. Issels RD (2008) Hyperthermia adds to chemotherapy. Eur J Cancer 44: 2546-2554.

19. Meyer JL, Kapp DS, Fessenden P, Hahn GH (1989) Hyperthermic oncology: current biology, physics and clinical results. Pharmacol Ther 42: 251-288.

20. Pekkanen AM, DeWitt MR, Rylander MN (2014) Nanoparticle enhanced optical imaging and phototherapy of cancer. J Biomed Nanotechnol 10: 1677-1712.

21. Day ES, Morton JG, West JL (2009) Nanoparticles for thermal cancer therapy. J Biomech Eng 131: 074001.

22. von Maltzahn G, Park JH, Agrawal A, Bandaru NK, Das SK, et al. (2009) Computationally guided photothermal tumor therapy using long-circulating gold nanorod antennas. Cancer Res 69: 3892-3900.

23. Kennedy LC, Bickford LR, Lewinski NA, Coughlin AJ, Hu Y, et al. (2011) A new era for cancer treatment: gold-nanoparticle-mediated thermal therapies. Small 7: 169-183.

24. Choi WI, Kim JY, Kang C, Byeon CC, Kim YH, et al. (2011) Tumor regression in vivo by photothermal therapy based on gold-nanorod-loaded, functional nanocarriers. ACS Nano 5: 1995-2003.

25. Moon HK, Lee SH, Choi HC (2009) In vivo near-infrared mediated tumor destruction by photothermal effect of carbon nanotubes. ACS Nano 3: 3707-3713.

26. Fisher JW, Sarkar S, Buchanan CF, Szot CS, Whitney J, et al. (2010) Photothermal response of human and murine cancer cells to multiwalled carbon nanotubes after laser irradiation. Cancer Res 70: 9855-9864.
27. Burke A, Ding X, Singh R, Kraft RA, Levi-Polyachenko N, et al. (2009) Long-term survival following a single treatment of kidney tumors with multiwalled carbon nanotubes and near-infrared radiation. Proc Natl Acad Sci U S A 106: 12897-12902.
28. Li TJ, Huang CC, Ruan PW, Chuang KY, Huang KJ, et al. (2013) In vivo anti-cancer efficacy of magnetite nanocrystal--based system using locoregional hyperthermia combined with 5-fluorouracil chemotherapy. Biomaterials 34: 7873-7883.
29. Ren F, Bhana S, Norman DD, Johnson J, Xu L, et al. (2013) Gold nanorods carrying paclitaxel for photothermal-chemotherapy of cancer. Bioconjug Chem 24: 376-386.
30. Rao W, Zhang W, Poventud-Fuentes I, Wang Y, Lei Y, et al. (2014) Thermally responsive nanoparticle-encapsulated curcumin and its combination with mild hyperthermia for enhanced cancer cell destruction. Acta Biomater 10: 831-842.
31. Dewhirst MW, Vujaskovic Z, Jones E, Thrall D (2005) Re-setting the biologic rationale for thermal therapy. Int J Hyperthermia 21: 779-790.
32. Kong G, Braun RD, Dewhirst MW (2001) Characterization of the effect of hyperthermia on nanoparticle extravasation from tumor vasculature. Cancer Res 61: 3027-3032.
33. Dermietzel R, Streffer C (1992) The cytoskeleton and proliferation of melanoma cells under hyperthermal conditions. A correlative double immunolabelling study. Strahlenther Onkol 168: 593-602.
34. Alexander Bagley RS-S, Peter A. Galie, Angela Q. Zhang, Jeffery Wyckoff, Luke Whitesell, Christopher S. Chen, Susan Lindquist, Sangeeta Bhatia (2015) Endothelial Thermotolerance Impairs Nanoparticle Transport in Tumors. Cancer Res: 3255-3267.
35. Bhise NS, Ribas J, Manoharan V, Zhang YS, Polini A, et al. (2014) Organ-on-a-chip platforms for studying drug delivery systems. J Control Release 190: 82-93.
36. Hauck TS, Jennings TL, Yatsenko T, Kumaradas JC, Chan WCW (2008) Enhancing the Toxicity of Cancer Chemotherapeutics with Gold Nanorod Hyperthermia. Advanced Materials 20: 3832-+.
37. Kong G, Dewhirst MW (1999) Hyperthermia and liposomes. Int J Hyperthermia 15: 345-370.
38. Stirland DL, Nichols JW, Miura S, Bae YH (2013) Mind the gap: a survey of how cancer drug carriers are susceptible to the gap between research and practice. J Control Release 172: 1045-1064.
39. Buchanan C, Rylander MN (2013) Microfluidic culture models to study the hydrodynamics of tumor progression and therapeutic response. Biotechnol Bioeng 110: 2063-2072.
40. Buchanan CF, Voigt EE, Szot CS, Freeman JW, Vlachos PP, et al. (2014) Three-dimensional microfluidic collagen hydrogels for investigating flow-mediated tumor-endothelial signaling and vascular organization. Tissue Eng Part C Methods 20: 64-75.
41. Antoine E, Buchanan C, Fezzaa K, Lee WK, Rylander MN, et al. (2013) Flow measurements in a blood-perfused collagen vessel using x-ray micro-particle image velocimetry. PLoS One 8: e81198.
42. Buchanan CF, Verbridge SS, Vlachos PP, Rylander MN (2014) Flow shear stress regulates endothelial barrier function and expression of angiogenic factors in a 3D microfluidic tumor vascular model. Cell Adh Migr 8: 517-524.

43. Sung JH, Kam C, Shuler ML (2010) A microfluidic device for a pharmacokinetic-pharmacodynamic (PK-PD) model on a chip. Lab Chip 10: 446-455.

44. Ng CP, Pun SH (2008) A perfusable 3D cell-matrix tissue culture chamber for in situ evaluation of nanoparticle vehicle penetration and transport. Biotechnol Bioeng 99: 1490-1501.

45. Miyawaki J, Yudasaka M, Azami T, Kubo Y, Iijima S (2008) Toxicity of single-walled carbon nanohorns. ACS Nano 2: 213-226.

46. Whitney J, DeWitt M, Whited BM, Carswell W, Simon A, et al. (2013) 3D viability imaging of tumor phantoms treated with single-walled carbon nanohorns and photothermal therapy. Nanotechnology 24: 275102.

47. Whitney JR, Sarkar S, Zhang J, Do T, Young T, et al. (2011) Single walled carbon nanohorns as photothermal cancer agents. Lasers Surg Med 43: 43-51.

48. Hood RL, Carswell WF, Rodgers A, Kosoglu MA, Rylander MN, et al. (2013) Spatially controlled photothermal heating of bladder tissue through single-walled carbon nanohorns delivered with a fiberoptic microneedle device. Lasers Med Sci 28: 1143-1150.

49. DeWitt MR, Pekkanen AM, Robertson J, Rylander CG, Nichole Rylander M (2014) Influence of hyperthermia on efficacy and uptake of carbon nanohorn-cisplatin conjugates. J Biomech Eng 136: 021003.

50. Zimmermann KA, Inglefield DL, Zhang JF, Dorn HC, Long TE, et al. (2013) Single-walled carbon nanohorns decorated with semiconductor quantum dots to evaluate intracellular transport. Journal of Nanoparticle Research 16.

51. Antoine EE, Vlachos PP, Rylander MN (2015) Tunable collagen I hydrogels for engineered physiological tissue micro-environments. PLoS One 10: e0122500.

52. Price GM, Tien J (2011) Methods for Forming Human Microvascular Tubes In Vitro and Measuring Their Macromolecular Permeability. Biological Microarrays: Methods and Protocols 671: 281-293.

53. Rabanel JM, Aoun V, Elkin I, Mokhtar M, Hildgen P (2012) Drug-loaded nanocarriers: passive targeting and crossing of biological barriers. Curr Med Chem 19: 3070-3102.

54. Gobin AM, Lee MH, Halas NJ, James WD, Drezek RA, et al. (2007) Near-infrared resonant nanoshells for combined optical imaging and photothermal cancer therapy. Nano Lett 7: 1929-1934.

55. O'Neal DP, Hirsch LR, Halas NJ, Payne JD, West JL (2004) Photo-thermal tumor ablation in mice using near infrared-absorbing nanoparticles. Cancer Lett 209: 171-176.

56. Shi J, Wang B, Chen Z, Liu W, Pan J, et al. (2016) A Multi-Functional Tumor Theranostic Nanoplatform for MRI Guided Photothermal-Chemotherapy. Pharm Res 33: 1472-1485.

57. Luo L, Bian Y, Liu Y, Zhang X, Wang M, et al. (2016) Combined Near Infrared Photothermal Therapy and Chemotherapy Using Gold Nanoshells Coated Liposomes to Enhance Antitumor Effect. Small.

58. Kwak B, Ozcelikkale A, Shin CS, Park K, Han B (2014) Simulation of complex transport of nanoparticles around a tumor using tumor-microenvironment-on-chip. J Control Release 194: 157-167.

59. Han B, Qu C, Park K, Konieczny SF, Korc M (2015) Recapitulation of complex transport and action of drugs at the tumor microenvironment using tumor-microenvironment-on-chip. Cancer Lett.

60. Raeesi V, Chan WC (2016) Improving nanoparticle diffusion through tumor collagen matrix by photo-thermal gold nanorods. Nanoscale 8: 12524-12530.
61. Kong G, Braun RD, Dewhirst MW (2000) Hyperthermia enables tumor-specific nanoparticle delivery: effect of particle size. Cancer Res 60: 4440-4445.
62. Szot CS, Buchanan CF, Freeman JW, Rylander MN (2011) 3D in vitro bioengineered tumors based on collagen I hydrogels. Biomaterials 32: 7905-7912.
63. Dabbagh A, Abdullah BJ, Abdullah H, Hamdi M, Kasim NH (2015) Triggering Mechanisms of Thermosensitive Nanoparticles Under Hyperthermia Condition. J Pharm Sci 104: 2414-2428.

Chapter 5: Engineering Considerations for H-FIRE treatment of Hepatocellular Carcinoma

5.1 Introduction
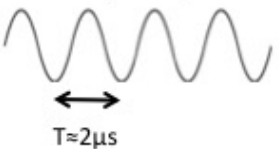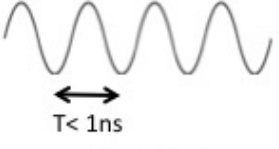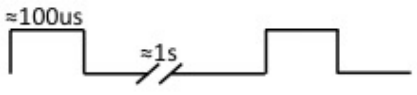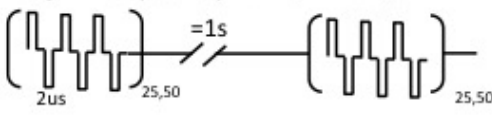
In 2015 the WHO estimates the effects of cancer will result in over 8 million deaths with approximately 10% attributed to cancers of the liver with incidence rate of liver cancer rising globally in the past decade[1]. Hepatocellular Carcinoma (HCC) will continue to be a major clinical burden in the U.S. given the emergence of obesity as an independent risk factor for HCC and the growing obesity rates in first world countries[2,3]. Chemotherapy can be used to treat HCC, however its efficacy is severely limited[4]. While chemotherapeutic agents can induce death in HCC cells, the central role of the liver in drug metabolism creates a critical limitation to produce sufficient concentration for complete tumor therapy. Therefore, the best clinical options to treat HCC remain surgical intervention, albeit resection or transplant, or *in situ* destruction through ablation technologies[5].

Radiofrequency ablation (RFA) is a surgical intervention to HCC that utilizes an active electrode to deliver a radiofrequency current, around 460 KHz, to a much larger passive electrode or grounding pad located distant from tumor site[5]. The resulting high current density at the active electrode coupled with the rapid current switching of the energy delivered results in ionic movement in the area near the electrode in the liver, causing frictional heating. At high enough energy, temperatures can reach above 100°C resulting in necrotic cell death. Microwave ablation (MWA) is a dielectric heating based ablation in which the dielectric material is the desired tissue. During MWA the alternating electromagnetic field forces water molecules in the tissue to oscillate out of phase with the applied field, leading to energy absorption and conversion to heat.

RFA and MWA have proven to be fairly well suited for the treatment of HCC when complete resection is challenging due to size or location, or removing of the tumors requires the removal of a

large non-tumorous liver. However, thermal based ablations induces indiscriminate, necrotic tissue destruction which can damage healthy vital structures near the tumor and the presence of major portal veins and hepatic veins can cause incomplete tumor necrosis due to heat sink effects leading to incomplete destruction.

Electroporation was originally developed as a cancer therapy to enhance drug delivery[6]. The first application of electric field stimulated membrane breakdown was used to enhance uptake of nonpolar chemotherapeutic drugs into tumor cells and was coined electrochemotherapy (ECT) which is current a clinical option along with a more recent use of electroporation for gene delivery[7,8]. Irreversible electroporation (IRE) is a relatively novel, non-thermal ablation modality that can be used to destroy tumors as a stand alone therapy[9]. Davalos et al were the first to propose utilizing electroporation to irreversibly destroy cells, not for transient permeabilization[10]. Clinically, IRE utilizes electrodes inserted either directly into or surrounding targeted tissue to deliver a series of short and intense electric pulses. These electric pulses, 100 us in duration and 1000-3000V/cm between the two electrodes, are delivered in sync with heart beat in order to minimize triggering of irregular heartbeats and result in cell death through inability to retain cellular homeostasis[11]. Positive reviews of the safety and efficacy of IRE treatments have previously been published highlighting the role of IRE in the treatment of tumors < 3cm in each dimension. Ultimately, IRE treatment efficacy is independent of heat generation and thermal processes and therefore making IRE a potential ablation technique for HCC in critical locations [12].

Ablation Type	Death Mechanism	Major Notes
Radiofrequency Ablation (RFA) [waveform] T≈2µs	Thermal	Rapid current change results in frictional heating; Requires low impedance, heating occurs in area of high current density; cannot treat around major blood vessels
Microwave Ablation (MWA) [waveform] T< 1ns	Thermal	Dielectric heating occurs. Heating occurs in a volume around antenna; can be used in multiple-applicator ablation
Irreversible Electroporation (IRE) [pulse diagram] ≈100us ≈1s	Non-Thermal Electroporation	Irreversible Electroporation above critical electric field (V/cm), can treat around major blood vessels with no thermal damage and ECM integrity ; requires cardiac syncing and muscle/neuro-blockers;
High Frequency IRE (H-FIRE) [pulse diagram] =1s 2us 25,50 25,50	Non-Thermal Electroporation	25-50 bipolar 2us pulses are sent every 1s. Irreversible electroporation occurs without muscle contraction or significant thermal damage. Higher electric field needed compared to IRE

Figure 1: Summary of different Thermal and Non-Thermal Ablation Techniques for HCC Treatment

High frequency irreversible electroporation (H-FIRE) was recently developed by Arena et al to overcome some of the shortcomings of IRE[13,14]. H-FIRE replaces the 100 us pulses utilized during clinical applications of IRE with a burst of shorter (500ns-2µs) bipolar pulses which are separated by a inter-pulse delay with a total energized time per burst comparable to IRE. Pulses < 2µs were modeled and shown to not induce muscle contractions[13]. Sano et al recently showed that an H-FIRE in vitro protocol of 80-100 burst at 1hz with 1 to 5µs pulses was capable of reducing the viability of pancreatic cells in suspension to less than 20% [15]. When cells were grown in a collagen 3D matrix, H-FIRE with 2µs pulses was found to have a lethal threshold of 760V/cm in pancreatic cancer cells, the same order of magnitude as monopolar IRE pulses [16]. Theoretical models of H-FIRE treatments highlight the treatment's ability to provide more predictable lesion volumes based on the potential of high-frequency

fields to overcome impedance barriers posed by low-conductivity tissues which are seen in heterogeneous tumor tissue which can cause incomplete treatment from electric field distortion[17,18]. Jiang et al gave a positive insight to H-FIRE, however questions if H-FIRE parameters could be used to create larger treatment volumes was raised[9]. A summary of these four ablations is shown in Figure 1. Ultimately, if H-FIRE can be shown to treat liver tissue without the need for heart syncing, muscle blockers, and can overcome tissue heterogeneity, there is great promise for H-FIRE as a HCC treatment.

One of the key limitations of IRE as an ablation technology is the limited real-time feedback that is present during *in vivo* treatment. While resistance and impedance measurements provide a better understanding and feedback of the biophysical breakdown of cellular membranes resulting from IRE and an idea of treatment efficacy, most clinical decisions of IRE treatment are based on computational modeling to estimate the volume of ablation *a priori*. These pretreatment models of IRE are necessary for planning electrode placement, determining pulse parameters needed, and estimating the predicted treatment volume[19]. Many of these predicted treatment volumes are determined from literature values of electric field threshold, however many of these values are not exact can be independent from pulse parameters. With the introduction of H-FIRE pulses, a better understanding of the electric field thresholds for many parameters must be elucidated for more accurate treatment planning, resulting in improved treatment outcomes for patients. *In vitro* studies are useful for highly controlled modeling of cell threshold resulting from IRE treatments and 3D *in vitro* tumor platforms have been useful for studying these novel treatments to determine electric field thresholds, however the thresholds determined from in vitro cells do not necessarily correlate directly to *in vivo* thresholds[20].

In addition to determining the feasibility of H-FIRE to non-thermally ablate clinically relevant volumes of tissue in the liver, the aim of this study is to more fully understand the mechanism of cell death during ablation with H-FIRE and to evaluate the potential for reducing nerve stimulation during

clinical delivery of H-FIRE pulses. In this study we utilize a 3D collagen *in vitro* model of HCC cancer with H4IIE cells subject to H-FIRE pulses to determine electric field thresholds. We investigated the lesion volumes produced in an *in vivo* porcine model. We show that pulse protocols can be altered to produce reliable sized lesions. Additionally we determine the affect of pulse energized on-time and number of pulses on cell death mechanism and prove that H-FIRE is capable of producing lesions valuable for clinical translation. Lastly we utilized infrared imaging to highlight the non-thermal nature of these treatments and the effect of pulse parameter on tissue heating, which is valuable to overcome many of the shortcomings of traditional thermal therapies. The results of this study highlight the promise of H-FIRE for filling the needs for novel ablations in the treatment of hepatocellular carcinoma.

5.2 Methods

5.2.1 In Vitro Tumor Platform

H4IIE rat hepatoma cell line (ATCC, Manasas VA) were utilized in the 3D *in vitro* tumor model to determine electric field threshold for multiple H-FIRE treatments. Cells were cultured in Eagles Minimum Essential Medium (EMEM) containing 10% fetal bovine serum (FBS; Sigma Aldrich, St. Louis MO) and 1% penicillin/streptomycin (P/S; Invitrogen, Carlsbad, CA) in a 37°C incubator with a 5% CO_2 humidified atmosphere. Collagen I hydrogels were utilized as an *in vitro* model of an HCC tumor as shown in Figure 2 A&B. These 3D hydrogel models were created as described previously by our group[20]. Briefly, the hydrogels were formed by neutralizing type I collagen suspended in HCl with a cell buffer containing 10% by volume 10x DMEM, cell media containing a final seeding density of $2x10^6$ cells/mL, and sufficient NaOH to result in a final solution pH of 7.4. The collagen-cell solution was then immediately pipetted into a 12mm diameter cylindrical molds with a volume to result in a height of 2.65mm. The hydrogel was allowed to polymerize for 15 min at 37°C after which the gels

were removed from the PDMS mold and were cultured in complete EMEM media for 72 hours prior to H-FIRE treatment. H-FIRE pulses were delivered with custom electrodes as seen in Figure 2A.

48 hours after H-FIRE treatment, cell culture media was removed and replaced with media containing 5 μM Calcein AM (Live stain; Invitrogen, Eugene, OR) and was incubated for 20 min at 37°C. 100 μL of 1.5 mM propidium iodide (PI; dead stain; Invitrogen, Eugene, OR) was then added to the gels for 8 min. The hydrogels were then rinsed 2x with PBS (Sigma Aldrich, St. Louis MO) to flush unabsorbed dyes. Cells were visualized using a Zeiss Observer Z1 (Carl Zeiss Microscopy LLC, Thornwood, NY). Cells that were stained green were considered live, while dead cells fluoresced as red. The red-stained region was measured using ImageJ analysis software. The electric field threshold, as highlighted as the white dotted region in Figure 2B was determined at the edge of the dead region and live region. The ablation zones were correlated to a finite element model to calculate the values of the electric field to establish the threshold described subsequently.
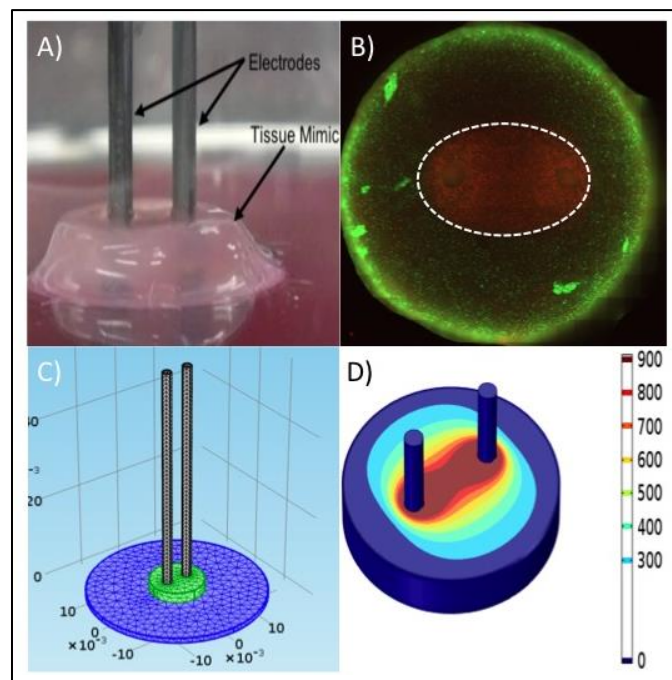
Figure 2: H-FIRE treatment in a 3D in vitro tumor platform. Live[Green] and dead[red] regions of cells in 3D hydrogel containing H4IIE separated by white dashed line after treatment of 100 burst of 100us on time for 1us(A) and 2us(B) pulses. The electric field threshold was determined utilizing a COMSOL model of the tumor platform(C)

5.2.2 COMSOL Modeling

Finite element models of the 3D *in vitro* tumor platform were created in COMSOL Multiphysics (Version 4.3, COMSOL Inc., Burlington MA). The hydrogel was modeled as a 2.65 mm thick, 12mm diameter cylinder with a solution conductivity of 1.2 S/m. Two cylinders, representing the active and ground electrode, were modeled as 0.85mm outer diameter with 3mm edge-to-edge distance in the center of the hydrogel. COMSOL Electric currents module was utilized to solve for the following equations:

$$\nabla \cdot J = Q_j \ / \ (A/m^3)$$

$$J = \left(\sigma + \varepsilon_0 \varepsilon_r \frac{\partial}{\partial t} \right) E \ / \ (A/m^2)$$

$$E = -\nabla U \ / \ (V/m)$$

In these equations, J is the current density, Q is the current source, σ is the conductivity which was set to 1.2 S/m, U is the electric potential, E in the electric field ε_0 ε_r are the permittivity of free space and relative permittivity respectively. One electrode was set to constant electric potential ie:

$$U = U \ [V] \qquad\qquad [4]$$

While the other electrode was set as a relative ground:

$$U = 0 \ V \qquad\qquad [5]$$

All other boundaries were defined, as electrical insulation where n is the normal vector to the surface and J is the electrical current

$$[6]$$
$$n \cdot J = 0 \ / \ (A/m)$$

5.2.3 *In vivo* Methods

Surgical Procedures. In total 15 ablations were performed in 3 separate animals with n=5 ablations/ H-FIRE setting employed. The number of ablations performed was selected to provide sufficient statistical power for analysis, while ensuring sufficient distance between ablation sites to avoid prior ablations, and to reduce potential variability in time between completing all of the ablations in a single animal and euthanasia 6Hrs later.

Following premedication with atropine (0.04mg/kg) anesthesia was induced using Telazol (5mg/kg, i.m.), Xylazine (2mg/kg, i.m.) and sodium thiopental (20mg/kg, i.v.). Animals were intubated and surgical anesthesia maintained with isoflurane. Pre-emptive analgesia (morphine, 0.06mg/kg, i.m.) was administered prior to commencing surgery. An accelerometer was placed on the the electrode handles, and a Bovie cautery grounding pad placed on the thigh. Animals were continuously monitored using telemetry and pulse-oximetry.

The abdominal wall was prepared using a chlorhexidine solution (x2), an upper midline incision (15-20cm) made, and a Balfour retractor placed to expose the liver. Ultrasound (US) guidance was used to identify and avoid major hepatic vessels. Two NanoKnife® IRE electrodes were positioned in parallel with spacing set to 1.5cm, and the active portion of the electrodes exposed to a length of 1cm. The electrodes were inserted into the hepatic parenchyma to a depth of 2.5-3.0cm, and successful electrode positioning confirmed by US (Figure 3A). Unlike previous studies using swine models to study IRE in the liver, no muscle relaxation drugs including neostigmine and atropine were needed in the study as muscle contractions were not seen during treatment with 2us bipolar pulses[21].

IRE electrodes were positioned within the liver, 1.5cm apart, within the parenchyma. The active portion of the electrodes was set to an exposure length of 1cm and the probe positioning was set and confirmed through the use of intra-operative ultrasound with Doppler. 100-300 bursts of 1500v/cm to

2800v/cm were delivered per ablation site. In order to examine the effect of pulse protocol on death mechanism, the number of cycles (on-time) of each burst was varied from 25-50 cycles.

Animals survived for 6h before anaesthetization and euthanasia performed with pentobarbital. A laparotomy was then performed and the liver was recovered. Lesions were excised in the center of the ablation zone. Half of the ablation was stained with triphenyltetrazolium chloride (TTC) while the remaining sections were fixed in formalin or taken for DNA laddering. Following tissue fixation, samples were prepared and sectioned 6-8μm) for H&E staining as previously reported (18). H&E stained slides were analyzed to confirm ablation areas and representative images captured. To analyze apoptotic cell death immunohistochemistry (IHC) was performed on sections using an antibody specific against cleaved caspase 3 (AbCam, Cambridge, MA) (19). Representative images of sections (n=5 per ablation) were taken and blind scored for cleaved caspase-3 expression using a scale of; 0-25% apoptosis = 0, 25-50% apoptosis = 1, 50-75% apoptosis = 2, > 75% apoptosis = 3. Data for each ablation performed were averaged and expressed as means ± SEM
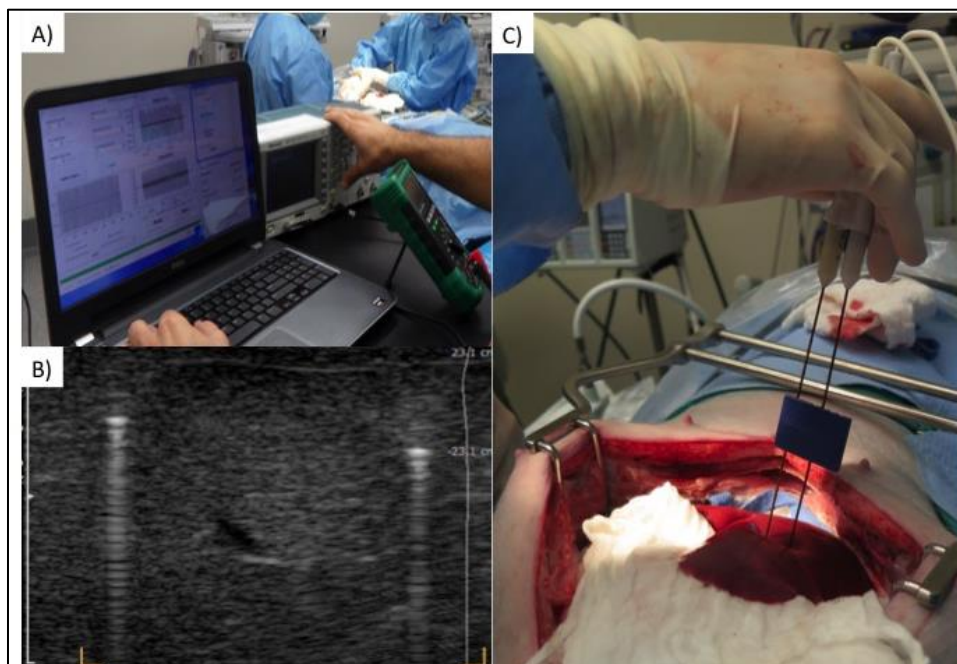

Figure 3 A) Overall setup of computer with custom software (Voltmed, Blacksburg VA) that sets voltage of H-FIRE generator below and records voltage and current of pulses delivered. Pulses are triggered by Tektronix AFG 3011 arbitrary

function generator. Ultrasound imaging is then used (B) to ensure placement of needle electrodes are in a homogenous area of the parenchyma or straddling a blood vessel when desired. Finally pulses are delivered through commercially available Nanoknife (c) with a 1cm exposure and 1.5 cm spacing. 100-300 pulses are then delivered at 1Hz while heart rate and muscle contractions are closely monitored

5.3 Results and Discussion

Typical IRE treatments utilize 80-300 monopolar pulses ranging from 50-200us in duration at a repetition rate defined by heart rate, close to 1Hz. H-FIRE parameters were chosen with similar relation to clinical IRE protocols. Treatments with a burst of 1 μs bipolar pulses were initially conducted. Treatments with a total of 100 bursts delivered at 1Hz. For comparison, groups with different energized time per burst were conducted where voltage, and burst were held constant but energized time was increased from 10 to 50 to 100 μs. The threshold for cell death for these treatments were 1393, 1078, and 813(Fig 4A). The difference was found to be statistically different with a 95% confidence level. For bursts of 2 μs, 100 bursts and voltage was kept constant and energized time was increased from 10 to 50 to 100 μs. Similar to 1 μs pulses, this data was significantly different with 95% confidence interval with thresholds of 1217, 910, and 712(Fig 4B).

Figure 4C shows the effect of number of burst on lethal electric field threshold. At 550V, the difference in electric field threshold between burst of 100us energized on time 2 μs pulses were determined. The electric field decreased from 712 to 687 to 643 for 100 to 200 to 300 bursts respectively. The differences between the electric field thresholds were not statistically significant for varied burst number for 2 μs pulses. This data agrees with previous IRE data produced by our group which shows minimal change in IRE electric field threshold after 80 pulses.
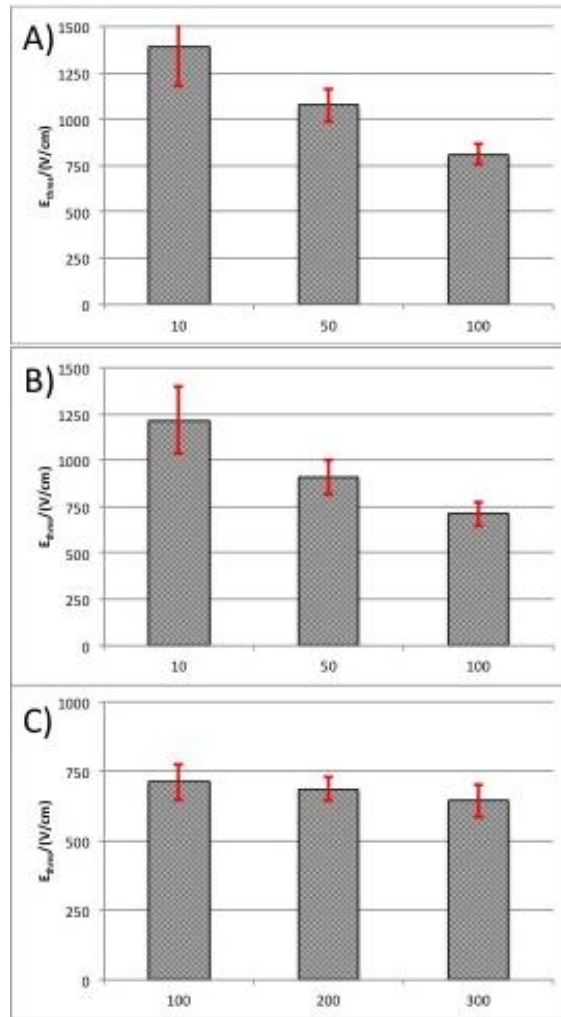
Figure 4. Determination of H-FIRE lethal electric field thresholds for in vitro tumor platform. Lethal field threshold for 100 bursts of 1us pulses with energized on time varied for 10,50 and 100us(A) 100 bursts of 2us pulses with energized on time varied for 10,50 and 100us(B). 100us energized on time of 2us pulses varied for 100,200,300 bursts(C).

All swine used in the study survived to the 6 h endpoint with no complications as expected. Heart rate and body temperature were measured during and after surgery and no significant changes were seen at either time. An experimental protocol of H-FIRE was successfully delivered as shown in Figure 2. A custom pulse generator (Voltmed, Blacksburg VA) was utilized as shown in Figure 2(A) driven by custom software that was capable of *in situ* voltage, current, and resistance measurements. Ultrasound was successfully utilized for probe placement as depicted in Figure 3(B) and successful delivery of 100-300 pulses was delivered utilizing Nanoknife electrodes as shown in Figure 3(C).

The first aim of this *in vivo* study was to determine the repeatability and predictability of lesion size creation through progressive burst amounts. The ablation volumes created from 100-300 pulses of 25 2µs pulses (100 µs energized on time) set to 1500V/cm are shown in Figure 5(D) and representative gross visualization of lesions for 100, 200, and 300 pulses are shown in Figure 5 A-C respectively. Additionally this study proved that TTC staining can predict the zone of ablation 6h after ablation as the surrounding viable liver tissue stains red and the nonviable tissue that has undergone irreversible electroporation does not stain, resulting in the dark or white colored areas. The results from this Figure highlight the ability to make controllable lesions in the liver based upon the number of burst delivered when on-time is kept constant. This data implies that, unlike the in vitro case, electric field threshold decreases with increased bursts during *in vivo* treatment even after 80 bursts of H-FIRE pulses. Additionally the relatively small deviation in the volumes indicate the repeatability of H-FIRE to create known lesion sizes and can be useful for future treatment planning protocols.
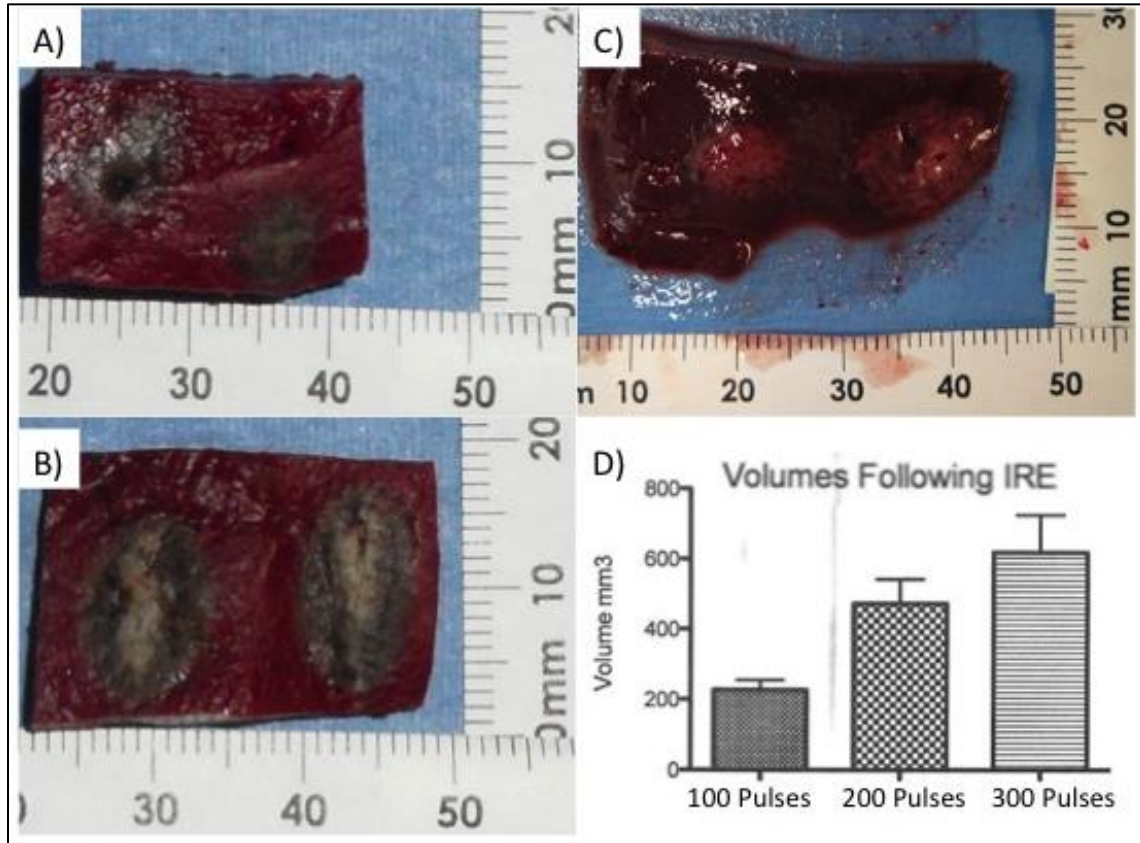
Figure 5: Liver High Frequency Irreversible electroporation (H-FIRE) ablation using two monopolar probes, spaced at 1.5cm apart with a 1-cm exposure. Ablation was performed at 1500V/cm. 100,200,and 300 (A-C) pulses consisting of 25 - 2 us bipolar cycles were delivered for an on-time of 100us per pulse for comparison to IRE pulses. Liver tissue was harvested 6 h after H-FIRE ablation. (A-C) shows the tissue after fixation with triphenyltetrazolium chloride (TTC). White and grey areas show areas of necrosis and low metabolic activity. The volumes from these gross samples were calculated and summarized in (D) with increasing volumes up to 300 Pulses when pulse on time and voltage are kept constant.

Sano et al recently showed using an *in vitro* model that cell death after H-FIRE occurs as a mix of apoptosis and necrosis[15]. We therefore wanted to test the hypothesis that protocol adjustment could occur to result in either more apoptotic or more necrotic tissue damage. A representative IHM histology micropictophotograph of a 25 cycle 300 pulse sample stained for Caspase (Brown) is shown in Figure 6(A), indicating the presence of apoptotic cell death with H-FIRE treatment. In order to test the ability to alter the balance of apoptosis to necrosis relative on-time and pulse number were varied. Figure 6(B) shows relative Caspase 3 activity as the result of blinded scoring. When pulse number is kept constant at 100 pulses and the energized on-time is increased from 100 to 200us per burst, the caspase activity

lowers, indicating less apoptosis with more on-time. Additionally when on-time is kept constant at 100us and the number of pulses increases to 300, a significant increase in Caspase activity is seen which implies that apoptosis can increase through shorter pulse trains and increase amount of bursts. Necrosis score was additionally calculate for these 3 cases and summarized in Figure 6(C). There was insignificant change in necrosis between 25 cycles, 300 burst and 50 Cycles 100 bursts, indicating that when enough energy is delivered, independent of mode, ample necrosis occurs. When the overall on time is low, as is the case for 25 cycles, 100 pulses there is significantly less necrosis. A representative image of the gross damage indicating a large lesion creation by 24 cycles, 300 burst is shown in Figure 6D. Overall, these results indicate the ability of H-FIRE to be adjusted using on-time and number of burst to change the cell death mechanism while creating significant lesions
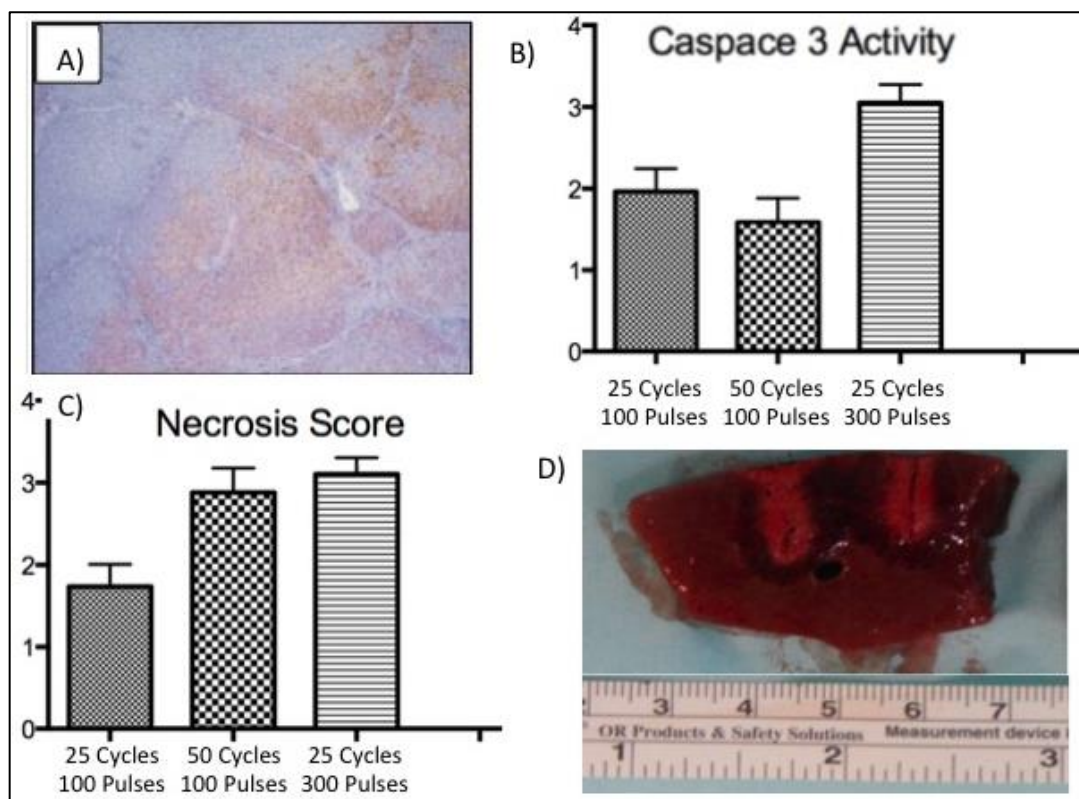
Figure 6. (A) A photomicrograph of tissue liver tissue after treatment with H-FIRE. IHC shows cleaved caspase-3 activity (CaspACE) (brown areas). (B)Samples were then scored blindly (0-4) for caspase activity as a measure for apoptotic activity. (C)Additionally necrosis was blindly scored (D) TTC stained liver treated with 50 cycles 100 pulses showing the area of ablation and low metabolic activity.

Ultrasound has previously been utilized to visualize IRE lesions in vivo[22]. Images of treated volumes show hypointense (dark) areas where lesion are present during and immediately following IRE treatment and hyperintense (light) regions 24 h post treatment[23,24]. In this study we aimed to investigate the ability of H-FIRE to create clinically feasible lesion sizes. In order to accomplish this, 50 cycles of 2 us bipolar pules were delivered at 1Hz for a total of 300 bursts, treatment time of 5 minutes. A voltage to distance ratio of 1800 V/cm across 1.5cm spacing with a 1cm exposure was delivered for a total of n=4 lesions. Ultrasound imaging was utilized immediately following treatment and an example is shown in Figure 7(a). A distinctive dumbbell-shaped ablation zone was reliably created as shown by the hypointense region in the ultrasonic image. TTC staining 6 h after treatment confirm the general shape and size of the lesion measured in the ultrasound and is shown in Figure 7(b).
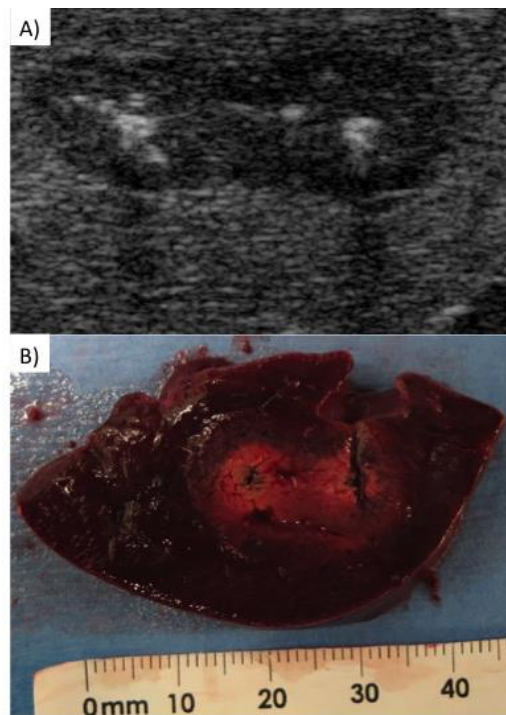

Figure 7. (A) ultrasound imaging immediately following treatment with 1800V/cm, 200 pulses, 200 us on time. Lesion is easily visualized immediately following treatment (hypoechoic area). The same "peanut" shape attributed to the H-FIRE treatment can be visualized 6 h after treatment using TTC confirming the shape seen in the ultrasound image

Significant research has been accomplished to prove the lack of thermal death mechanism in IRE, attributing most of the cell damage to irreversible poration of cellular membranes[12,25]. Experimental and computational models have also been employed for determining the lack of thermal damage for H-FIRE in the previous year[15]. However, *in vivo* confirmation of minimal heating using relevant treatment protocols to create clinically applicable lesions has yet to be confirmed. In this study an infrared camera was utilized to measuring heating during treatment of 300 burst, 50 cycles at 1800V/cm over 1.5 cm spacing. The thermal images from 5 burst, 40burst, and 80 bursts are shown in Figure 6 A-C respectively. The range of temperatures of treatment did not exceed 55°C as shown in the white area between the electrodes. While the surface temperature will not be as high as the temperature within the tumor, the needles were carefully placed as to minimize the depth of treatment to have better representative thermal imaging. It has previously been shown that temperature rises similar to those seen in this study are consistent with minimal cell death occurring from heat[25]. Additionally, an ex vivo experiment was accomplished utilizing freshly excised porcine liver. The tissue was subjected to 100 and 200 μs energized on time 2 μs H-FIRE pulses for up to 300 bursts. Heating was measured as seen in Figure 7D&E. Data from this experiment shows the build up of heat after excessive pulses. Additionally 200 μs pulses result in an average of 2.6 times the heating as 100 μs pulses. Energized on time therefore not only affects the death mechanism, but the potential for thermal damage, and must be kept in mind when treating nearing critical structures.
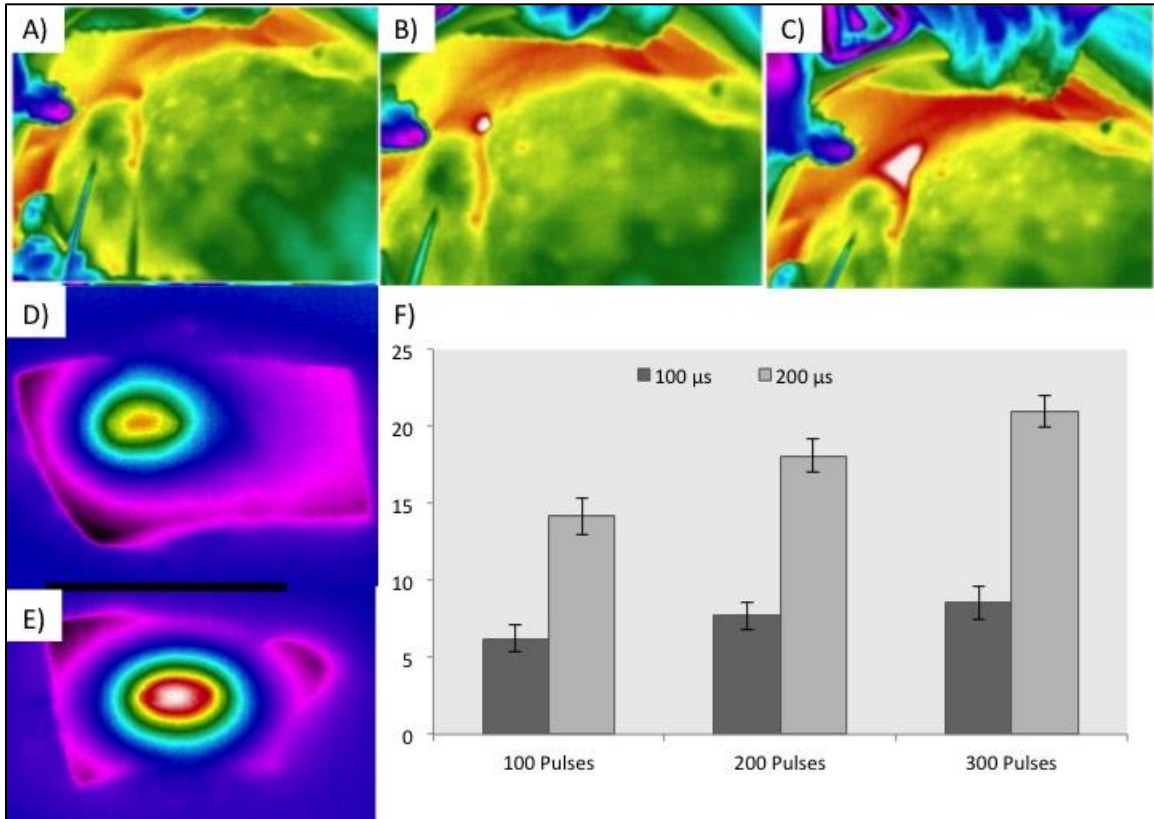
Figure 8: Infrared imaging of liver during treatment with H-FIRE. 2700 V is delivered in bursts containing 25 cycles of 2us bipolar pulses with an exposure length of 1cm and spacing of 1.5cm. The needles (lower left) were placed into the liver at an angle <30° so that lesion is close to surface to allow for the surface based infrared thermal imaging. (A) shows the liver immediately following 5 pulses, 40 pulses (b), and 80 pulses (C). Ex vivo heating after 10(D) and 100(E) bursts of 2us bipolar pulses used to collect quantitative change in temperature data for varied on time and burst number (F)

5.4 Conclusion

This was the first recorded study of High Frequency Irreversible Electroporation in liver comparing *in vitro* and *in vivo* results. The results of this study indicate that H-FIRE is capable of producing both clinically useful and repeatable lesions in swine livers. The nature of H-FIRE pulses allows for more parameter selectively than IRE, with the introduction of cycles, interpulse delay, and bursts. In this study, these parameters were varied and the mechanism of cell death and degree of potential thermal damage was found to be dependent on both burst delivery and on-time. Ultrasound imaging was utilized for both probe guidance and for lesion determination immediately following

115

treatment. The results of this study show that H-FIRE appears to be safe and effective for ablation of liver tissue and will help provide the engineering background for future clinical translation of H-FIRE.

5.5 References

1. Venook AP, Papandreou C, Furuse J, de Guevara LL (2010) The incidence and epidemiology of hepatocellular carcinoma: a global and regional perspective. Oncologist 15 Suppl 4: 5-13.
2. Wang CH, Wey KC, Mo LR, Chang KK, Lin RC, et al. (2015) Current trends and recent advances in diagnosis, therapy, and prevention of hepatocellular carcinoma. Asian Pac J Cancer Prev 16: 3595-3604.
3. Forner A, Llovet JM, Bruix J (2012) Hepatocellular carcinoma. Lancet 379: 1245-1255.
4. Deng GL, Zeng S, Shen H (2015) Chemotherapy and target therapy for hepatocellular carcinoma: New advances and challenges. World J Hepatol 7: 787-798.
5. Niemeyer DJ, Simo KA, McMillan MT, Seshadri RM, Hanna EM, et al. (2015) Optimal ablation volumes are achieved at submaximal power settings in a 2.45-GHz microwave ablation system. Surg Innov 22: 41-45.
6. Mir LM, Orlowski S, Belehradek J, Paoletti C (1991) Electrochemotherapy Potentiation of Antitumor Effect of Bleomycin by Local Electric Pulses. European Journal of Cancer 27: 68-72.
7. Heller LC, Heller R (2006) In vivo electroporation for gene therapy. Human Gene Therapy 17: 890-897.
8. Yarmush ML, Golberg A, Sersa G, Kotnik T, Miklavcic D (2014) Electroporation-Based Technologies for Medicine: Principles, Applications, and Challenges. Annual Review of Biomedical Engineering, Vol 16 16: 295-320.
9. Jiang CL, Davalos RV, Bischof JC (2015) A Review of Basic to Clinical Studies of Irreversible Electroporation Therapy. Ieee Transactions on Biomedical Engineering 62: 4-20.
10. Davalos RV, Mir LM, Rubinsky B (2005) Tissue ablation with irreversible electroporation. Annals of Biomedical Engineering 33: 223-231.
11. Martin II RC, McFarland K, Ellis S, Velanovich V (2012) Irreversible electroporation therapy in the management of locally advanced pancreatic adenocarcinoma. Journal of the American College of Surgeons 215: 361-369.
12. Garcia PA, Rossmeisl JH, Jr., Neal RE, 2nd, Ellis TL, Davalos RV (2011) A parametric study delineating irreversible electroporation from thermal damage based on a minimally invasive intracranial procedure. Biomed Eng Online 10: 34.
13. Arena CB, Sano MB, Rylander MN, Davalos RV (2011) Theoretical Considerations of Tissue Electroporation With High-Frequency Bipolar Pulses. Ieee Transactions on Biomedical Engineering 58: 1474-1482.
14. Arena CB, Sano MB, Rossmeisl JH, Jr., Caldwell JL, Garcia PA, et al. (2011) High-frequency irreversible electroporation (H-FIRE) for non-thermal ablation without muscle contraction. Biomedical Engineering Online 10.
15. Sano MB, Arena CB, DeWitt MR, Saur D, Davalos RV (2014) In-vitro bipolar nano- and microsecond electro-pulse bursts for irreversible electroporation therapies. Bioelectrochemistry 100: 69-79.

16. Sano MB, Arena CB, Bittleman KR, DeWitt MR, Cho HJ, et al. (2015) Bursts of Bipolar Microsecond Pulses Inhibit Tumor Growth. Sci Rep 5: 14999.
17. Ricke J, Jurgens JHW, Deschamps F, Tselikas L, Uhde K, et al. (2015) Irreversible Electroporation (IRE) Fails to Demonstrate Efficacy in a Prospective Multicenter Phase II Trial on Lung Malignancies: The ALICE Trial. Cardiovascular and Interventional Radiology 38: 401-408.
18. Bhonsle SP, Arena CB, Sweeney DC, Davalos RV (2015) Mitigation of impedance changes due to electroporation therapy using bursts of high-frequency bipolar pulses. Biomed Eng Online 14 Suppl 3: S3.
19. Neal RE, 2nd, Millar JL, Kavnoudias H, Royce P, Rosenfeldt F, et al. (2014) In vivo characterization and numerical simulation of prostate properties for non-thermal irreversible electroporation ablation. Prostate 74: 458-468.
20. Arena CB, Szot CS, Garcia PA, Rylander MN, Davalos RV (2012) A Three-Dimensional In Vitro Tumor Platform for Modeling Therapeutic Irreversible Electroporation. Biophysical Journal 103: 2033-2042.
21. Charpentier KP, Wolf F, Noble L, Winn B, Resnick M, et al. (2011) Irreversible electroporation of the liver and liver hilum in swine. HPB (Oxford) 13: 168-173.
22. Rubinsky B, Onik G, Mikus P (2007) Irreversible electroporation: A new ablation modality - Clinical implications. Technology in Cancer Research & Treatment 6: 37-48.
23. Lee EW, Loh CT, Kee ST (2007) Imaging guided percutaneous irreversible electroporation: ultrasound and immunohistological correlation. Technol Cancer Res Treat 6: 287-294.
24. Appelbaum L, Ben-David E, Sosna J, Nissenbaum Y, Goldberg SN (2012) US findings after irreversible electroporation ablation: radiologic-pathologic correlation. Radiology 262: 117-125.
25. Garcia PA, Davalos RV, Miklavcic D (2014) A numerical investigation of the electric and thermal cell kill distributions in electroporation-based therapies in tissue. PLoS One 9: e103083.

Chapter 6: Treatment of Infiltrative Skin Tumors in Horses With High-Frequency Pulsed Electrical Energy

Matthew DeWitt*[2], Christopher Byron*[1]Richard Trahan[1], Elsa Ludwig[1], Eduardo LaTouche[2], Rafael Davalos[2], and John Robertson[2]

1 Department of Large Animal Clinical Sciences, Virginia-Maryland Regional College of Veterinary Medicine, Virginia Tech, Blacksburg, VA 24061
2 School of Biomedical Engineering and Science, College of Engineering, Virginia Tech, Blacksburg, VA 24061

6.i Abstract

Infiltrative skin tumors, including equine sarcoid, squamous cell carcinoma, and equine malignant melanoma, are challenging to treat and to control. At the time of presentation, some tumors may incorporate or be adjacent to critical anatomic structures (nerves, major blood vessels), be too large to surgically resect, or have proven to be resistant to therapy (surgery, cryotherapy, chemotherapy, among others).

We have developed a novel form of tumor therapy that is minimally-invasive, can be done under sedation, and used for ablation of masses that are not amenable to surgical resection. The therapy, termed high-frequency irreversible electroporation (abbreviated H-FIRE), administers clusters of electrical pulses through electrodes implanted in tumors. Mechanistically, the electrical energy remains 'localized' in the tumor, creating nanoscale porosities in tumor cells that cause the tumor cells to degenerate. Normal, non-tumor cells, adjacent to the administered electrical field, resist the effects of energy delivery by rapid repair of cell membranes.

Here, we report treatment of 5 horses with recurrent equine sarcoid, squamous cell carcinoma, or equine malignant melanoma. It each case, H-FIRE therapy predictably ablated tumor volume and improved patient clinical condition.

6.1 Introduction

Cutaneous tumors, including sarcoid, squamous cell carcinoma, and melanoma, are extremely common in horses[1]. While many small, circumscribed lesions can be controlled with surgical resection, cryoablation, hyperthermy, or localized chemotherapy (eg, topical 5-fluorouracil or cisplatin in oil or bioabsorbable beads), infiltrative lesions are uniquely difficult to control. Therefore, use of multiple modalities, such as a combination of surgical resection and local chemotherapy, is common in the approach to such tumors. However, complete resolution may not be obtained because of local infiltration of critical structures that cannot be surgically removed, extensive local tissue invasion by tumors, and recurrent locally aggressive growth of tumors. Therefore, there remains a high-priority need for development of additional effective and safe treatments for such tumors.

Sarcoid is the most common cutaneous tumor of horses[2]. Various therapeutic measures have been described. Common treatments include surgical excision[3], cryosurgery[3], and laser surgery[4]. The rate of local recurrence of equine sarcoid (RES) is roughly 50% following attempted surgical resection; higher rates of control (>75%) can be achieved with cryoablation. However, a proportion of RES cases will resist control with these methods and may progress with relentlessly recurrent growth. Therefore, these treatments may be combined with local topical or intralesional chemotherapy including 5-fluorouracil[5] or cisplatin in oil[6] or bioabsorbable beads[7]. However, despite multimodal treatment, recurrence rates remain close to 20%.

As for other cutaneous tumors in horses, squamous cell carcinoma is frequently treated with conventional surgical excision and local chemotherapeutic drug injection or implantation. This approach can be successful for many patients[7,8]. However, tumors that have been unsuccessfully treated via other modalities and those with gross lesions that cannot be fully

resected are at high risk of recurrence[8]. As such, there is a need for development of treatment modalities that can better effect tumor regression in situ.

Equine malignant melanoma (EMM) typically presents clinically as multicentric, confluent multinodular lesions with a propensity for growth around the anus, perineum and tailhead, among other sites (peri-mandibular). Successful surgical excision of small, circumscribed, individual EMM nodules has been well-documented.[9] However, resection of large, perianal confluent tumor masses is simply impractical because of locally extensive infiltration. Infiltrative cells penetrating connective tissue are likely to be a source of recurrence (i.e., incomplete resection) and closure and wound management are extremely problematic. Any tumor, regardless of histotype, in the peri-parotid mandibular fossa usually deeply invests nerves, ducts and major vessels, cannot be surgically removed without the risk of damage to major structures and patient debility/dysfunction. Horses with such tumors present a particular challenge to treatment. Surgical debulking with local chemotherapy can be effective[7] however many patients have recurrence.

Irreversible electroporation(IRE) is a relatively novel, no-thermal focal ablation technique designed to overcome many of the shortcomings of traditional thermal ablations such as RFA and MWA that can result in significant collateral tissue damage, incomplete therapy as a result of "heat sink" effect, and destruction of the underlying tissue microarchitecture[10]. IRE protocols involve the placement of two or more electrodes into the tumor space[11]. Clinically, electrical pulses 50-100 us in pulse duration are delivered between these electrodes in coordination with a patient's heart beat to minimize trigger of irregular hear beats and a strong anesthetic protocol including a neuromuscular blockade is given to prevent the stimulation of intense muscle contractions that can cause patient discomfort and needle displacement which can

confound treatment planning[12-14]. The electric field formed from the delivery of these pulses leads to nanoscale defects, pores, in the cellular membrane. Above a critical electric field threshold, these pores cannot close, resulting in irreversible damage leading to cell death while sparing the underlying tissue structure and critical adjacent structures[15].

IRE may be an effect treatment of tumors in anatomical locations that are sensitive to thermal damage or, in the case of this study, where function of the tissue, rectal muscles, must be unimpaired. However, the electrically induced muscle contractions as a result of the delivered pulses complicates surgery and makes treatment under solely local anesthetic impossible[16]. The risks and complications associated with equine sedation and general anesthesia are closely linked with the risks and complications involved in equine surgery and therefore treatment under mild sedation and local anesthesia should be considered of upmost importance for the treatment of tumor lesions. With this in mind, reducing muscle contractions associated with IRE treatments has become an interesting research problem[17,18]. Groups have studied the use of a current cage electrode layout design to localize current to the treatment region, however these designs may not be useful for the treatment of surface lesions due to the prohibitive layout of electrodes.[16] Additionally, changing pulse parameters can reduce muscles contractions, as muscle contractions are known to increase exponentially as pulse duration increases under 100us[19].

With this in mind, Arena et al recently showed that in vivo application of shorter, 1-2us, bipolar pulses with a short interpulse delay can eliminate the muscle contractions associated with equal on-time IRE pulses (50-100us)[18]. These high frequency irreversible electroporation (H-FIRE) pulses are seen in Fig. 1B and were delivered with synchronization of heartbeats. Additionally, it has theoretically been shown to produce more uniform treatment areas in

heterogeneous tissue due to the high frequency component of tissue impedance, which can lead to better fitting computational models, allowing treatment planning which was utilized in this study[20]. Ultimately, these novel bipolar pulses for the use of IRE treatments can lead to safer, higher efficacy ablations and should be better understood for clinical translation.

This case report presents the use of H-FIRE pulses for the treatment of multiple surface lesions in equine patients; demonstrating the safety and efficacy of this novel treatment under mild sedation rather than the prohibitive complete anesthetic conditions. We have shown that bursts of 2us bipolar pulses were effective in reducing multiple surface lesions while resulting in minimal muscle contractions with clinical pulse settings and without the need for heart synchronization or neuromuscular blockers.
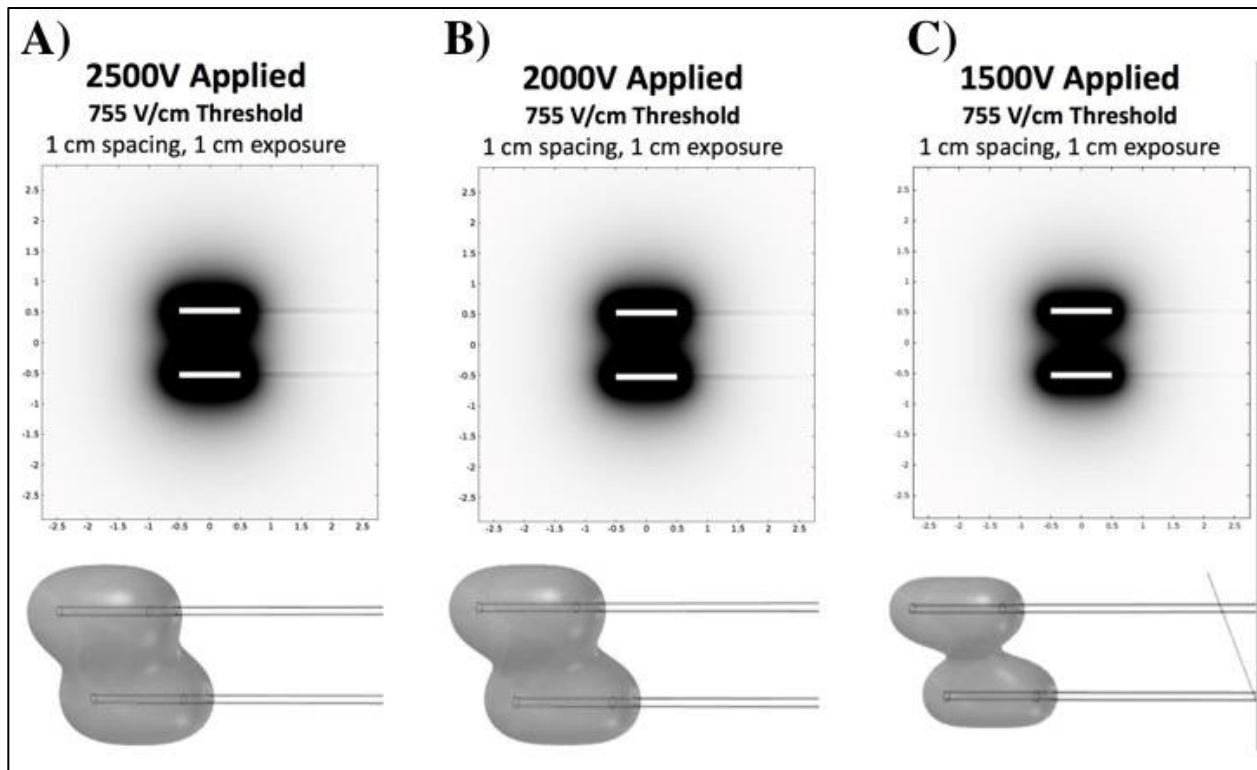
6.2 Results and Discussion:

Figure 1: Computational COMSOL model for prediction of treatment volume in H-FIRE treatment of surface tumors. Data is show in 2D and 3D volumetric presentation for 1cm spacing and 1cm exposure for 2500V(a), 2000V(b), and 1500V(c)

For H-FIRE treatment utilizing 2us bipolar pulses, a conservative electric field threshold of 755 V/cm was assumed based on previous in vitro and in vivo results. When 150 bursts of 100 us energized on time H-FIRE pulses are delivered, as in the case of these case studies, this is the hypothesized electric field threshold in which irreversible electroporation occurs, ablating all cells within this electric field. A COMSOL model of a surface lesion was established to highlight the volume of treated tissue for 2500V, 2000V, and 1500V as seen in Figure 1 (A-C) respectively. The results from this computational model show the need for delivering high voltages to create large effective treatments areas (2x2x1cm). This model was utilized for planning treatment spacing, voltages, and electrode exposure to ensure complete lesion volume destruction. While not shown, computational modeling also occurred to ensure that non-thermal ablation occurred, sparring sensitive tissue in the perianal and perivulvar space.

Table 1. Treatment Matrix for Equine Case Studies

Patient	Age at Treatment (years)	Tumor Type	# of Treatment	Initial Tumor Size	Final Tumor Size	% Change in Tumor
1(Equine)	11	Multifocal EMM	4	5.0x2.5x2.5cm	4.0x2.0x2.0	-52.1%
2(Equine)	14	Perivulvar SCC	2	3.5x3.5x3.5cm	3.0x3.0x1.6	-66.4%
3(Equine)	20	Perianal SCC	2	6.0x8.0x4.0cm	1.0x0.5x0.5cm	-99.8%
4(Equine)	19	Intranasal MCT	2	3.0x1.5x1.0cm	2.2x1.5x1.0	-26.7%
5(Equine)	x	Mulifocal EMM	x			

A clinical protocol of H-FIRE was developed and utilized in this case study for the treatment of infiltrative skin tumors. High voltage 2us bipolar pulses to induce irreversible electroporation of cancerous cells were applied through two sharp electrodes as seen in Figure 2A&B. For larger lesions, clinical Angiodynamic electrodes were used with an electrode-to-electrode spacing distance of 1-1.5cm. To avoid arcing from skin folds in smaller lesions, custom

electrodes were created and used as seen in Figure 2B with a spacing of 0.5c. Bursts of 100 us energized on time pulses were delivered without the need of heart beat synchronization. Electrodes were inserted directly into the surface lesions as seen in Figure 2C with the use of Angiodynamic spaces to ensure steady placement of active electrodes. Bursts were successfully delivered in sets of 50 at 1Hz with a 15 second delay to minimize and avoid extensive thermal damage based on computational modeling. Gross and histological examination show that no thermal scarring or damage for the maximum treatments of 2700V were seen. Placement of electrodes and number of treatment sites were determined based on the estimated volume results of the computational model to result in extensive and complete tumor volume.
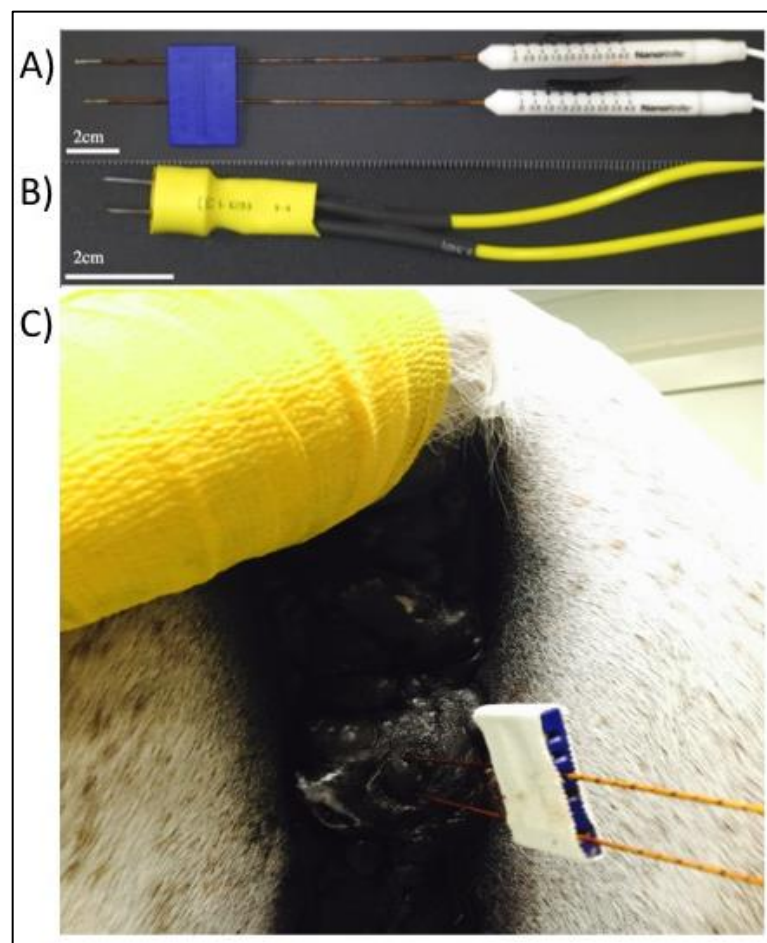

Figure 2: Treatment Protocol for Delivery of H-FIRE under Mild Sedation. (a) Angiodynamic commercial electrodes with spacer(blue) (b) custom needle electrodes used to treat small lesions (c) treatment of perianal surface lesions with placement of exposed electrodes directly into lesion

A key outcome of this case report was to exhibit the use of clinical H-FIRE parameters without the need for heart synchronization or general anesthesia. Traditional IRE pulses(50-100us) can cause extreme muscle contractions as seen in the supplemental video. In human clinical applications for soft tissue ablation, this can cause needle placement disruption, confounding important and precise computational treatment planning. In equine treatment, this necessitates the use general anesthesia for patient and surgeon safety. The use of general anesthesia can lead to many potential complications and hinders the ability to use H-FIRE as an outpatient treatment for surface lesions. In this study, the use of up to 2500V, capable of treating volumes (2x2x1cm), was effectively delivered with little no muscle contraction. Example data collected from a custom electrode during perianal treatment is shown in Figure 3. This data shows no muscle contractions during a 2250V treatment as no spikes in acceleration corresponding to pulse delivery are seen beyond the noise of data. A video of treatment (Supplementary) further highlights how minimal muscle contraction is only seen when 2800V is delivered with 1.5cm spacing. Overall, this data highlights the ability of clinical parameters of H-FIRE to be delivered without general anesthesia.
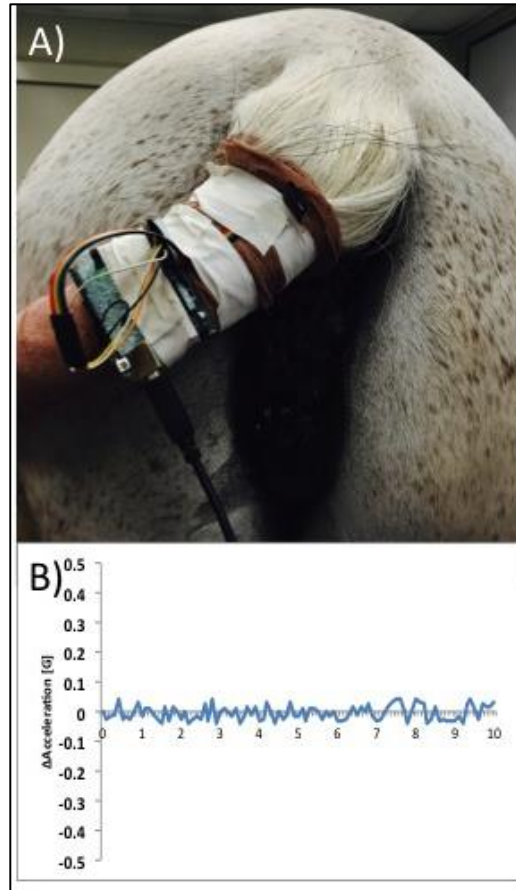
Figure 3 Muscle Contraction measurements during H-FIRE ablation. (a) Placement of custom accelerometer to measure muscle contractions in real time during treatment (b) example data showing no contractions with 2250V delivered at 1Hz

Preliminary efficacy of H-FIRE debulking of surface lesions in equine patients is highlighted in Table 1 and further shown in Figure 4. Six equine patients, having clinical presentation of infiltrative skin tumours including sarcomas and melanomas were effectively treated with H-FIRE. A summary of the debulking success of treatments is highlighted by an average decrease in tumor volume of 62.5%. In Figure 4, the red highlighted region of a melanoma is shown before (Figure 4a) and two weeks after two treatments with H-FIRE(Figure 4b). A noticeable collapse of tumor is shown grossly and confirmation of tumor destruction occurred via ultrasound imaging. With regions of epithelial tissue are seen between needle locations two weeks after H-FIRE treatment in Figure 4c. This presentation shows the destruction of melanin producing epithelial cells without the destruction of the underlying tissue

architecture. After 2 weeks this tissue was re-epithelialized, showing the ability of healthy cells to repopulate following effective treatment.
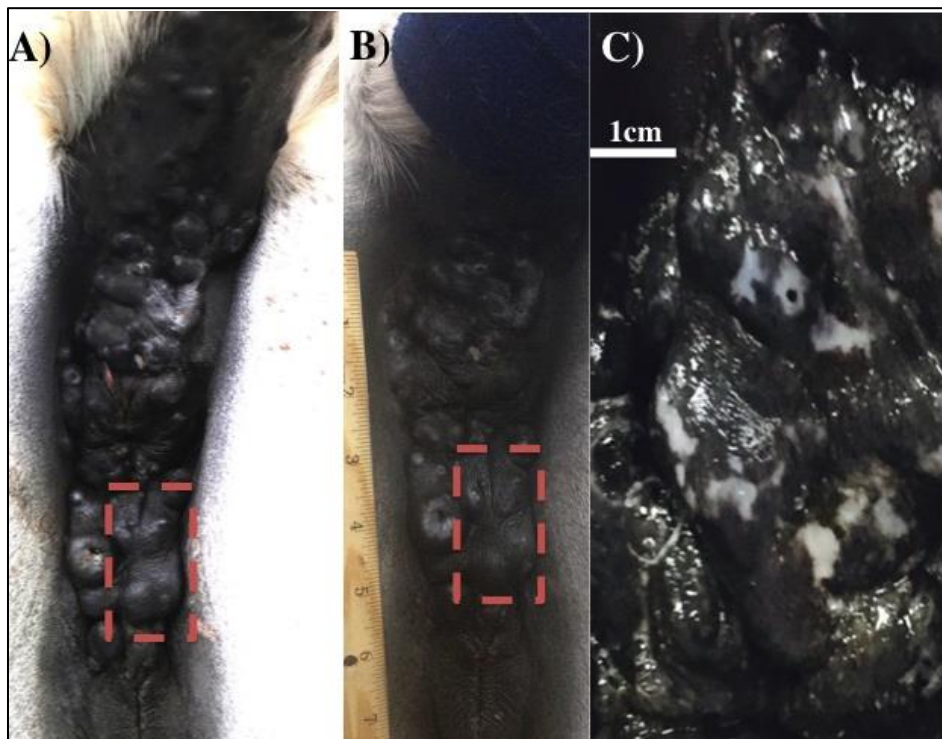

Figure 4 Efficacy of H-FIRE for treatment. Gross exinimation of treated area(red) before treatment (a) and two weeks following 2 treatments with H-FIRE (b) Enlarged treatment area showing death of melanin producing epithelial cells(white) two weeks after treatment

While the efforts in this study do not result in complete regression for all tumors treated, it should be noted that previously published work by Al-Sakare et al utilizing IRE in vivo did not obtain 100% regression rates. Their data, like the data presented here, is valuable for successful validation and adaption of protocols for human clinical applications. These successful results of this in vivo case report substantiate further in vivo studies of H-FIRE ablations as a clinical tool for the treatment of surface lesions in equine and potentially human clinical applications.

6.3 Conclusions

We have demonstrated that H-FIRE therapy is an effective clinical procedure for the treatment and control of inoperable infiltrative skin tumors in horses. The therapy can be delivered to horses that are standing and sedated, eliminating the need for general anesthesia and standard

recumbent surgery. Therapy is delivered in a time-efficient manner (usually under one hour) and

post-treatment wound management is minimal and predictable.   Repetitive treatments may be

needed to control complex, large lesions.

6.4 References

1. Rooney JR, Robertson JL (1996) Equine pathology. Equine pathology.
2. Marti E, Lazary S, Antczak DF, Gerber H (1993) Report of the first international workshop on equine sarcoid. Equine veterinary journal 25: 397-407.
3. Martens A, De Moor A, Vlaminck L, Pille F, Steenhaut M (2001) Evaluation of excision, cryosurgery and local BCG vaccination for the treatment of equine sarcoids. Vet Rec 149: 665-669.
4. Carstanjen B, Jordan P, Lepage OM (1997) Carbon dioxide laser as a surgical instrument for sarcoid therapy--a retrospective study on 60 cases. Can Vet J 38: 773-776.
5. Stewart AA, Rush B, Davis E (2006) The efficacy of intratumoural 5-fluorouracil for the treatment of equine sarcoids. Aust Vet J 84: 101-106.
6. Theon AP, Pascoe JR, Carlson GP, Krag DN (1993) Intratumoral chemotherapy with cisplatin in oily emulsion in horses. J Am Vet Med Assoc 202: 261-267.
7. Hewes CA, Sullins KE (2006) Use of cisplatin-containing biodegradable beads for treatment of cutaneous neoplasia in equidae: 59 cases (2000–2004). Journal of the American Veterinary Medical Association 229: 1617-1622.
8. Theon AP, Wilson WD, Magdesian KG, Pusterla N, Snyder JR, et al. (2007) Long-term outcome associated with intratumoral chemotherapy with cisplatin for cutaneous tumors in equidae: 573 cases (1995-2004). J Am Vet Med Assoc 230: 1506-1513.
9. Rowe EL, Sullins KE (2004) Excision as treatment of dermal melanomatosis in horses: 11 cases (1994-2000). Journal of the American Veterinary Medical Association 225: 94-96.
10. Davalos RV, Mir LM, Rubinsky B (2005) Tissue ablation with irreversible electroporation. Annals of Biomedical Engineering 33: 223-231.
11. Martin II RC, McFarland K, Ellis S, Velanovich V (2013) Irreversible electroporation in locally advanced pancreatic cancer: potential improved overall survival. Annals of surgical oncology 20: 443-449.
12. Yarmush ML, Golberg A, Sersa G, Kotnik T, Miklavcic D (2014) Electroporation-Based Technologies for Medicine: Principles, Applications, and Challenges. Annual Review of Biomedical Engineering, Vol 16 16: 295-320.
13. Neal RE, 2nd, Millar JL, Kavnoudias H, Royce P, Rosenfeldt F, et al. (2014) In vivo characterization and numerical simulation of prostate properties for non-thermal irreversible electroporation ablation. Prostate 74: 458-468.
14. Martin II RC, McFarland K, Ellis S, Velanovich V (2012) Irreversible electroporation therapy in the management of locally advanced pancreatic adenocarcinoma. Journal of the American College of Surgeons 215: 361-369.
15. Jiang CL, Davalos RV, Bischof JC (2015) A Review of Basic to Clinical Studies of Irreversible Electroporation Therapy. Ieee Transactions on Biomedical Engineering 62: 4-20.
16. Golberg A, Rubinsky B (2012) Towards electroporation based treatment planning considering electric field induced muscle contractions. Technology in cancer research & treatment 11: 189-201.
17. Arena CB, Sano MB, Rylander MN, Davalos RV (2011) Theoretical Considerations of Tissue Electroporation With High-Frequency Bipolar Pulses. Ieee Transactions on Biomedical Engineering 58: 1474-1482.

18. Arena CB, Sano MB, Rossmeisl JH, Jr., Caldwell JL, Garcia PA, et al. (2011) High-frequency irreversible electroporation (H-FIRE) for non-thermal ablation without muscle contraction. Biomedical Engineering Online 10.

19. Reilly JP (2012) Applied bioelectricity: from electrical stimulation to electropathology: Springer Science & Business Media.

20. Bhonsle SP, Arena CB, Sweeney DC, Davalos RV (2015) Mitigation of impedance changes due to electroporation therapy using bursts of high-frequency bipolar pulses. Biomed Eng Online 14 Suppl 3: S3.

Chapter 7: Future Work

The 3D *in vitro* model utilized in chapter 3 to study nanoparticle transport has a broad range of future applications in elucidating nanoparticle feature effects on nanoparticle. While nanoparticle size is generally first thought of when describing nanoparticles, other features such as nanoparticle surface charge should be studied to determine how these affect transport in our system. We have begun a collaborative at the University of Texas at Austin to study the effect of dimensionality on nanoparticle transport. 1D grapheme sheets will be compared to 2D carbon nanotubes and 3D carbon Nanohorns in order to optimize treatments utilizing carbon nanoparticles based on dimension.

One of the values of the model utilized in Chapter 4 and 5 of this dissertation is the axisymmetric nature of a cylindrical system which allows for simplifying coupled computational models of mass transport into a 1D system. While there is great value in this, which was taken into account for these studies, the oversimplification of the tortuous vascular network present in a tumor to a straight, one-size vessel might not accurately model the transport boundaries nanoparticle face in the tumors. We have therefore begun to develop a novel model; building on knowledge gained from the demonstrated model to better replicate the vascular tumor. An overall depiction of this model is seen in Figure 1a below. This model has already been developed and we are in the beginning stages of validating its use to study nanoparticle transport. The PDMS stamp used to create the now rectangular vascular bed will be modified as shown in Figure 1b where it will be replaced by a tortuous configuration to study the effects of different angled vessels on extravasation of nanoparticles.
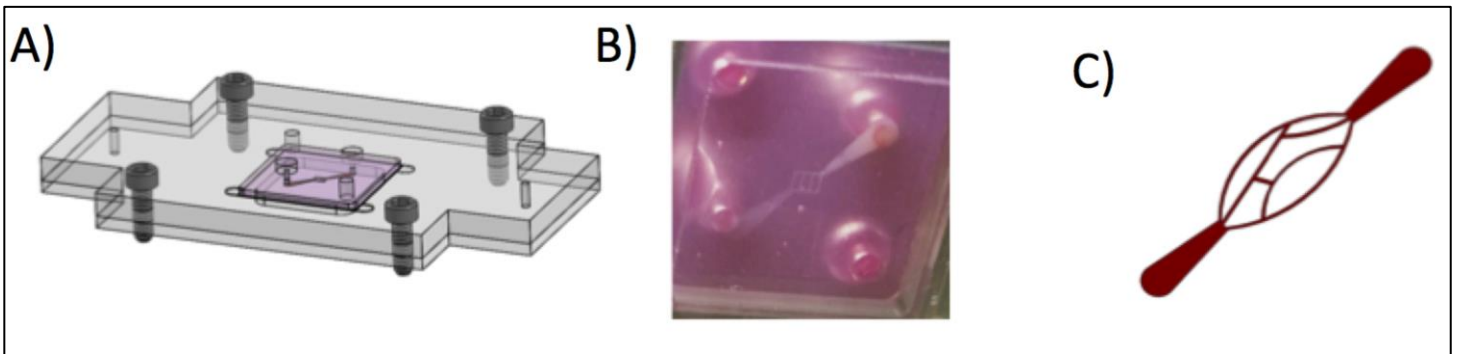
Figure 1. Depiction (a) of novel 3D tumor model which will be utilized in future nanoparticle transport studies including tortuous vessel creation (b) image of rectangular setup currently studied and (c) depiction of tortuous setup for future studies

As stated in the mild hyperthermia chapter, this non-lethal heat results in not only increased transport at the tumor tissue level, but increased activity of drug known as thermal enhancement. It will be imperative to utilize the tumor platform with not only SWNH-QD to study the effects of heat on SWNH transport, but SWNH-Cisplatin conjugates as described in chapter three, in order to co-optimize transport and Cisplatin enhancement. Since results of these studies show that mild hyperthermia has little to negative effects on nanoparticle uptake, it is imperative to establish a method to thermally trigger the release of carried Cisplatin from the particles to

The results from Chapter 6 shed interesting light on the value of 3D tumor platforms for studying H-FIRE. In Figure 6.4c, increasing the burst number from 50 to 200 has no effect on the electric field threshold of 2us bipolar pulses. This data agrees with previous data our group has published that beyond 80 pulses of IRE or 80 bursts of H-FIRE, the effects of additional pulses are minimal on electric field threshold. However, the results from the in vivo study in this chapter show a significant increase in treated volume from 100 to 300 pulses. We have therefore begun to establish a computational model of the in vivo setup as shown in the Figure below in order to compute the electric

field thresholds based on treated volume in the in vivo model. This data will be highly valuable for future H-FIRE optimization studies to better establish the necessary burst number. The in vitro data presented in this study, thermal data from the end of the chapter, along with additional accelerometer data will be incorporated with this novel, dynamic computational model of in vivo treatment into a manuscript to be submitted in the following month.
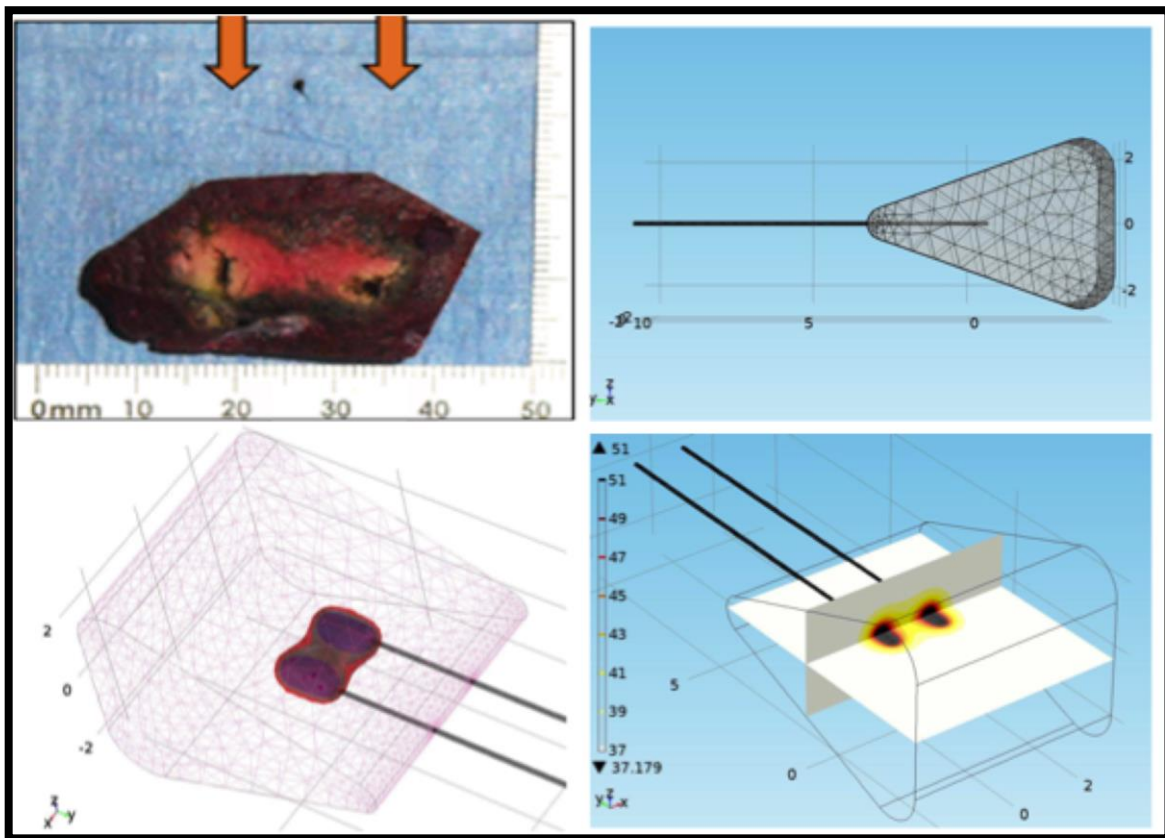

Figure 2: Use of Computational model of in vivo liver treatment to establish electric field thresholds. Data from this study can directly be compared to *in vitro* data

The results in Chapter 7 will be published as a case report. While this data and study are valuable in showing the ease of H-FIRE delivery compared to IRE for outpatient treatment of infiltrative skin lesions, for better adaption of this technology careful treatment planning of treatable lesions will need to occur. Patients in these studies often had very progressed stages of skin lesions and H-FIRE was delivered more as a

debulking, palliative treatment. In order to show efficacy more intensive treatment planning should occur in a small patient population and complete regression should be tracked. Additionally, there is great hope that H-FIRE can produce a pro-inflammatory reaction, leading to secondary destruction of tumor. There is promise in this idea as establish by previous research in our lab, future work should keep this in mind and attempt to track markers for such.

Overall, the data and progress described in this dissertation lay the groundwork for many future studies. The 3D platform described can be used to study a wide range of nanoparticles and can additionally be optimized to better represent the tumor microenvironment. Work can be established to increase not only the transport of SWNHs in the tumors but also the efficacy of carried drugs through photothermal enhancement. Lastly further *in vivo* studies and characterization of in vivo thresholds must occur to optimize H-FIRE parameters for clinical translation.